

---

# Feasibility of Near-Earth Object Deflection by Breakthrough Starshot Technology

Michael Frühauf

---



Munich 2018



---

# Durchführbarkeit von Erdbahnkreuzerabwehr mit Breakthrough Starshot Technologie

Michael Frühauf

---



München 2018



# Feasibility of Near-Earth Object Deflection by Breakthrough Starshot Technology

**Master's thesis**

at the

Faculty of Physics

of the

Ludwig-Maximilians-University Munich

handed in by

**Michael Frühauf**

(Matr. No.: 10755759)

born November 26, 1988

in Neumarkt i.d.OPf., Germany

supervised by

Prof. Dr. Andreas Burkert

(University Observatory Munich)

Munich, 31.07.2018



# Durchführbarkeit von Erdbahnkreuzerabwehr mit Breakthrough Starshot Technologie

**Masterarbeit**

an der

Fakultät für Physik

der

Ludwig-Maximilians-Universität München

eingereicht von

**Michael Frühauf**

(Matr. Nr.: 10755759)

geboren am 26. November 1988

in Neumarkt i.d.OPf., Deutschland

betreut durch

Prof. Dr. Andreas Burkert

(Universitäts-Sternwarte München)

München, 31.07.2018



**”Even the smallest person can change the course of the future.”**

Galadriel – Lord of the Rings: The Fellowship of the Ring, 1954



# Contents

<b>Abstract</b>	<b>1</b>
<b>1 Introduction</b>	<b>3</b>
1.1 The zoo of small bodies . . . . .	3
1.2 Boon and bane of near-Earth objects . . . . .	8
1.3 Conventional NEO mitigation . . . . .	14
<b>2 Near-Earth object deflection with Breakthrough Starshot</b>	<b>17</b>
2.1 Breakthrough Starshot Project . . . . .	17
2.2 Deflection concept . . . . .	19
2.3 Required velocity change . . . . .	21
2.4 Deflection by single event momentum transfer . . . . .	26
2.5 Deflection by constant fire . . . . .	30
2.6 Deflection with maximum projectile number . . . . .	35
2.7 Targeting accuracy and impact probability . . . . .	39
2.8 Course correction of projectiles . . . . .	43
2.9 Gravitational perturbation of projectiles . . . . .	46
2.10 Deflection in acceleration zone . . . . .	49
2.11 Energy release and cratering by projectiles . . . . .	53
2.12 Momentum multiplication for projectile impacts . . . . .	58
2.13 Projectiles in interplanetary space . . . . .	61
2.14 Location of light beamers . . . . .	64
<b>3 Deflection simulation</b>	<b>69</b>
3.1 MAIDS code . . . . .	69
3.2 Setup and impactor populations . . . . .	70
3.3 Results . . . . .	71

<b>4 Summary and outlook</b>	<b>77</b>
<b>Appendices</b>	<b>80</b>
A Details of MAIDS code . . . . .	81
B Details of setup and impactor populations . . . . .	87
<b>Bibliography</b>	<b>89</b>
<b>List of figures and tables</b>	<b>97</b>
<b>Abbreviations</b>	<b>99</b>
<b>Nomenclature</b>	<b>105</b>
<b>Acknowledgement</b>	<b>107</b>
<b>Statement in lieu of an oath</b>	<b>109</b>

# Abstract

## English

This Master's thesis treats the near-Earth object deflection by the Breakthrough Starshot technology, where low-mass chip-satellites with lightsails are accelerated to 20% speed of light and transfer their linear momentum to the near-Earth objects by an impact. We want to figure out, if this future technology might be a reliable solution for planetary defense, especially for the threat by asteroids. Most publications about Breakthrough Starshot concentrate on interstellar traveling, though the aspect of near-Earth object deflection was never studied before. On the other hand, there is no satisfying near-Earth object deflection method developed yet, which can reliably handle km-sized impactors with a short lead time and also no smaller object has ever been deflected until now. We tackle this question by basic analytic calculations and a self-written N-body simulation. The investigations show that 100-m-sized near-Earth objects might be deflectable, but km-sized objects seem to remain a threat for Earth. We also reveal the targeting accuracy to be the bottleneck of this concept. The energy release during the cratering process shows a huge potential for a tremendous momentum multiplication, which might solve the issue of km-sized objects, why this aspect is worth being studied in future work.

*Key words:* near-Earth objects – asteroid deflection – impulsive – Breakthrough Starshot

## German

Diese Masterarbeit behandelt die Abwehr von Erdbahnkreuzern mit Hilfe von Breakthrough Starshot Technologie, bei welcher massearme Chipsatelliten mit Lichtsegel auf 20% Lichtgeschwindigkeit beschleunigt werden und diese durch einen Einschlag ihren linearen Impuls auf die erdnahen Objekte übertragen. Wir wollen herausfinden, ob diese Zukunftstechnologie eine zuverlässige Lösung für die planetare Verteidigung darstellen könnte, insbesondere gegen die Bedrohung durch Asteroiden. Die meisten Veröffentlichungen über Breakthrough Starshot konzentrieren sich auf das interstellare Reisen. Der Aspekt der Erdbahnkreuzerabwehr wurde bisher jedoch noch nicht untersucht. Andererseits wurde bis zum heutigen Tag keine zufriedenstellende und zuverlässige Erdbahnkreuzerabwehr für km-große Einschlagkörper mit einer kurzen Vorlaufzeit entwickelt und auch kein kleineres Objekt wurde bisher abgelenkt. Wir packen diese Frage mit analytischen Berechnungen und einer selbstgeschriebenen N-Körper Simulation an. Die Nachforschungen zeigen, dass 100-m Objekte abgewehrt werden könnten, km-große Objekte scheinen jedoch weiterhin eine Gefahr für die Erde zu bleiben. Außerdem identifizieren wir die Zielgenauigkeit als Nadelöhr dieses Konzepts. Die freigesetzte Energie während der Kraterausbildung zeigt ein beachtliches Potenzial für eine enorme Impulsverstärkung, was eine Lösung für km-große Objekte darstellen könnte und weshalb dieser Aspekt in zukünftigen Arbeiten weiter untersucht werden muss.

*Schlüsselwörter:* Erdbahnkreuzer – Asteroidenabwehr – impulsiv – Breakthrough Starshot

# Chapter 1

## Introduction

### 1.1 The zoo of small bodies

Besides the Sun and planets, our Solar System consists of numerous small bodies, ranging from hundreds of kilometers to less than micrometer size. The inactive large rocky objects among this group are called *asteroids*, while m-sized and smaller objects are referred to as *meteoroids*. On the other hand, active bodies, forming a dust and gas atmosphere (coma) by outgasing, are named *comets*. One should take care not mixing up the term meteoroid with *meteorite*, which is the remnant of a meteoroid reaching Earth's surface, or a *meteor*, which is the phenomena of emitted light during a meteoroids passage through Earth's atmosphere. If the brightness of the object during atmospheric entry exceeds roughly a magnitude of -3, it is called *fireball* or if it is brighter than approximately a magnitude of -8, the term *bolide* is used (Yeomans, 2016) (Wyatt, 2008) (Abe, 2008).

Asteroids and comets formed during the Solar System's birth about 4.6 billion years ago and therefore are interesting objects for research about our origin. After the gravitational collapse of a slowly rotating gas and dust cloud, the Sun formed in the center of the system, surrounded by a protoplanetary disc. The dust grains in the disc started sticking together, leading to larger and more massive particles. The more massive particles with higher gravitational attraction assimilated the surrounding dust and ice to objects called *planetesimals*, which were up to km-size. Most of the planetesimals ended up in planets by further collisions and sticking, while others were ejected from the Solar System due to close encounters or crashed into the Sun. A small fraction remained as small bodies in the Solar System, nevertheless those survivors still count millions of objects (Yeomans, 2016).

There are various populations of small bodies in the Solar System, yet the most relevant

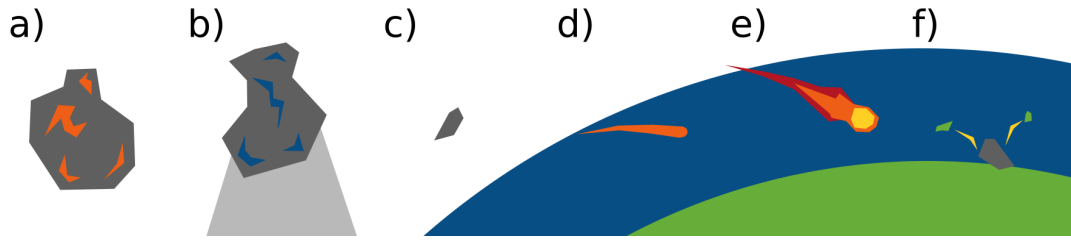


Figure 1.1: Term clarification:

- a) Asteroid: larger than m-sized and without coma
- b) Comet: with coma
- c) Meteoroid: m-sized and smaller
- d) Meteor: light emitted during atmospheric entry
- e) Fireball or bolide: brighter than the brightest planets
- f) Meteorite: remnant on Earth's surface

are the *main asteroid belt* and the *Kuiper belt*. The Kuiper belt consists of icy objects beyond the Neptune orbit between semi-major axes of  $35 \text{ AU} \lesssim a \lesssim 50 \text{ AU}$  with a combined mass  $\sum m < 10^{-1} M_{\oplus}$ . Those bodies formed outside the snow line, a theoretical border line dividing the inner warm region of a planetary system from the outer cold region. While within the snow line the water is in gas phase, beyond the line the vapor resublimates to ice and therefore ice grains grew together with dust to planetesimals. The snow line is expected to be not stationary with time, hence during planet formation, the snow line might have been at a different distance to the young Sun as it is nowadays. The main asteroid belt is located between Mars and Jupiter and spreads roughly between  $2 \text{ AU} \lesssim a \lesssim 4 \text{ AU}$  with a combined mass of  $\sum m \approx 6 \times 10^{-4} M_{\oplus}$ . Following the nebula hypothesis for the Solar System formation, which supposes the planets formed at their present orbits, Jupiter prevented an additional terrestrial planet to form by its huge gravitational force. According to the theory, the main asteroid belt is a debris field depending only on this single process. The rivaling Nice model assumes a change of the gas and ice giant's orbits in the early Solar System by gravitational encounters with countless small objects, referred to as migration. These movements of the planets disturbed and forced many small objects from the Kuiper belt to move inside to the center of the Solar System. Here, they got captured by mean motion resonances of Jupiter, among others in the outer parts of the main asteroid belt, where they mixed with the indigenous bodies (Yeomans, 2016) (Wyatt, 2008) (Levison et al., 2009).

Among the minor populations, the *Trojan asteroids* and *Hildas* are located in the inner Solar System. Trojan asteroids can be found at Jupiter's Lagrangian points L4 and L5,

which means they are in a J1/1 mean motion resonance at about  $a \approx 5.2$  AU. Usually, the Trojan asteroids are subdivided into *Trojans*, which follow Jupiter and *Greeks*, running ahead of Jupiter. Hildas have a J3/2 mean motion resonance with aphelia opposite to Jupiter's location or marginally inside L4 and L5. Hence, those bodies are located inside of Jupiter's orbit. There are also other populations of small bodies in the outer Solar System as *Centaurs*, the *scattered disc*, or the *Oort cloud* (Levison et al., 2009).

Besides all the populations far away from Earth, objects with a perihelion  $q \leq 1.3$  AU, are called *near-Earth objects* (NEOs). While NEOs include asteroids and comets, *near-Earth asteroids* (NEAs) exclusively comprise asteroids fulfilling the upper criterion. Among near-Earth objects the majority are asteroids and about 15% of the near-Earth asteroids are binary objects, which means two gravitationally bound objects orbiting a common barycenter (Mainzer et al., 2012) (Levison et al., 2009).

As there are many small body populations in the Solar System, NEOs can have different sources. Long-period comets, which can have orbital periods of millions of years, are expected to origin from the Oort cloud, where they got perturbed by other stars of the Milky Way. The majority of short-term comets start as Kuiper belt or scattered disk objects, perturbed by Uranus or Neptune to reach Jupiter's *sphere of influence* (SOI) where they get scattered into a NEO orbit. The source of almost all NEAs is the main asteroid belt. The asteroids slowly drift away from their stable orbits due to the *Yarkovsky effect*, which arises from the time delay between the absorption of sunlight and the re-emission via thermal radiation. Since the objects rotate, the re-emission occurs in a different angle than the sunlight arrives, leading to a tiny additional force. Subsequently they enter resonance regions of Jupiter, where their eccentricity changes over millions of years. Finally, they reach the Martian orbit, where they are pulled by a close encounter with Mars into a NEA trajectory. Similar to resonances, a combination of Jupiter's and Saturn's gravitational forces can change a circular main belt asteroid orbit to a NEA orbit. In the main asteroid belt, several gaps of semi-major axes are created by *powerful resonances*. They arise, if the timescale for restocking the gaps is longer than the timescale for clearing the gaps. The most important ones for NEOs are the J3/1 main motion resonances and the  $\nu_6$  secular resonance. In contrast to powerful resonances, *diffusive resonances* do not create gaps (Levison et al., 2009) (Bottke et al., 2004).

NEOs can be divided into four classes, depending on their orbital parameters relative to the Earth orbit with a semi-major axis of  $a = 1.0$  AU, a perihelion of  $q = 0.983$  AU and an aphelion of  $Q = 1.017$  AU. An object of the *Amors* is always outside Earth's

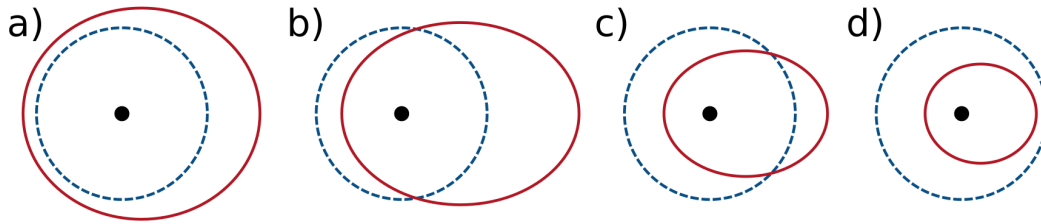


Figure 1.2: Classes of near-Earth objects with red orbits, compared to the blue, dashed Earth orbit and the black Sun in the center:

- a) Amors with  $a \geq 1.0$  AU and  $1.3$  AU  $\geq q \geq 1.017$  AU
- b) Apollos with  $a \geq 1.0$  AU and  $q \leq 1.017$  AU
- c) Atens with  $a \leq 1.0$  AU and  $Q \geq 0.983$  AU
- d) Apoheles or interior-to-Earth objects with  $a \leq 1.0$  AU and  $Q \leq 0.983$  AU

orbit, because they are defined with  $a \geq 1.0$  AU and  $q \geq 1.017$  AU but a maximum of  $q \leq 1.3$  AU. *Apollos* are crossing Earth's orbit with  $a \geq 1.0$  AU and  $q \leq 1.017$  AU, why the major part of their orbits lie beyond Earth's orbit. Other crossing objects are *Atens* with  $a \leq 1.0$  AU and aphelia  $Q \geq 0.983$  AU, however their orbits are mainly located inside Earth's orbit. Finally, *Apoheles* or *interior-to-Earth objects* (IEOs) stay inside Earth's orbit with  $a \leq 1.0$  AU and  $Q \leq 0.983$  AU. An asteroid or comet is not fixed to one class, but can change from one orbit type to another by planetary encounters (Mainzer et al., 2012). A illustration of all four classes can be found in Fig.1.2.

Other groups are commonly used in the field of NEO research, too. *Potential hazardous asteroids* (PHAs) are a subgroup of NEAs. PHAs have a minimum orbit intersection distance with Earth MOID  $\leq 0.05$  AU, which means they get closer to Earth's orbit than 0.05 AU. Since those orbits have a MOID change rate of  $0.05$  AU/100<sub>yr</sub>, they might approach even more and therefore be able to collide with Earth within 100 years. Furthermore PHAs have an absolute magnitude  $H \geq 22.0$ , which corresponds by an average NEA albedo of 0.14 to a 140 m asteroid. Those objects are able to penetrate Earth's atmosphere, reach the surface and cause massive damage. To highlight the objects with an even higher likelihood of impacting Earth than PHAs, the European Space Agencies (ESA) Space Situational Awareness (SSA) segment uses another subgroup of NEOs, the so-called *threatening objects*, including asteroids and comets of any size with an impact probability on Earth  $P > 0$  (Perna et al., 2016) (ESA NEO Coordination Centre, 2018).

On 23rd of July, 2018, there were 18421 NEOs known, ranging from m-size to km-size, whereby only 107 comets were among them. Out of those, 1909 were identified as PHAs and 754 threatening objects. Those numbers are rising from day to day and until 23rd of

July, there were 965 NEOs discovered in the year 2018. As one can see, the huge majority of known NEOs are asteroids (ESA NEO Coordination Centre, 2018).

Alongside the classification by orbital parameters and hazard, spectroscopic and mineralogical taxonomies can be found in literature. There are various historic attempts as the *Chapman taxonomy*, *Tholen taxonomy* or *Bus taxonomy*, based on visual observations of asteroids. The newer *Bus-DeMeo taxonomy* from 2010 includes observations of the wavelength from  $0.8 - 2.5 \mu\text{m}$  and therefore uses near-IR, too. There are 24 classes, depending on the absence or presence of spectroscopic features. Those features can be the result of the mineralogical composition, but they not necessarily have to. Therefore, they should be rather seen as only a trend. Though the classes were not defined by the asteroid composition, the class capital letters sometimes imply a mineralogical background, as C-type for carbonaceous, S-type for stony and M-type for metallic. While asteroids usually have to be categorized by remote, meteorites can be analyzed in laboratories explicitly for their properties. Here, exact investigation is necessary, since they can also origin from other celestial bodies like the Moon or Mars. Again, meteorites can be classified in various ways with diverse subgroups, different to the classifications mentioned above (DeMeo et al., 2009)(Burbine, 2002) (Fraser, 2013).

There is also a nomenclature for the different structural types. If an object is a single rigid body with low porosity, kept together by global cohesion, it is called *monolith*. The other extreme are so-called *rubble piles*. Those objects consist of loosely bound individual fragments of various sizes, which are mainly held together by self-gravity and less by cohesive forces. They can have small-scale voids and cracks in the size order of tens of micrometers, called microporosity and large-scale hollow spaces and fractures, the macroporosity. Theoretical models and observations imply that all km-sized asteroids and larger are rubble piles. Moreover, investigations of asteroid rotation curves indicate that even smaller objects down to roughly 150 m might be mainly rubble piles. Below, objects mostly have rotation frequencies above the gravitational break-up limit, why those objects must be monolithic. The structure is a very important property for planetary defense, because the behavior of a body during the deflection for different structures might differ significantly (Asphaug, 2004)(Britt et al., 2003).

Usually, the bodies discussed before are bound to the Sun, yet objects entering the Solar System from outside were suggested by formation models long before. Finally, in October 2017, the first unbound *interstellar object* (ISO) with the name *Oumuamua* was discovered (Meech et al., 2017).

As one can see by the numerous ways of classification, there is a wide spectrum of small objects inside and outside the Solar System with various compositions and properties – a real zoo of small bodies.

## 1.2 Boon and bane of near-Earth objects

As pointed out before, small objects continuously changing their orbits. As a result, the median life times of asteroids from the  $\nu_6$  resonance and the J3/1 mean motion resonance are  $\tau_{\text{life}} \approx 2$  Myr, where the  $\nu_6$  ones stay in a NEA orbit for a mean time  $\tau_{\text{NEO},\nu_6} \approx 6.5$  Myr and the J3/1 for  $\tau_{\text{NEO},\text{J3/1}} \approx 2.2$  Myr. 70 – 80% end up falling into the Sun and 12 – 28% are ejected from the Solar System. For the mentioned resonances there is also a probability of colliding with Earth, ranging from  $0.002 \gtrsim P \gtrsim 0.01$ . In general the impact timescale varies with the size of the body, which is connected to the population size. Large and rare objects have longer impact timescales compared to the numerous small NEAs which impact frequently. An overview can be seen in Tab.1.1. However, the impact rate of NEOs has not been constant through the Solar System’s history, as the formation models point out with a decreasing number of planetesimals. Despite this declining trend, there was a period with an increased number of impacts about 3.9 billion years ago, referred to as *Late Heavy Bombardment* (Bottke et al., 2004) (Yeomans, 2016).

Though it might sound paradox, NEO impacts on Earth were important for the evolution of life and not least for the human civilization. Water is essential for life on Earth, but it is still unknown where the water originates from, since Earth formed inside the snow line. One possibility would be the water delivery by external sources, or in more detail by a subgroup of stony asteroids with approximately 5% and comets with roughly 80% water. The asteroid impacts were triggered by disturbances of the asteroid belt region at Jupiter, while cometary impacts occurred due to the migration of Uranus and Neptune. However, it is expected that comets only have made a small contribution to the water on Earth. In addition, the deuterium to hydrogen ratios of cometary observations do not fit to terrestrial water. A recent model named *Grand Tack* assumes the migration of Jupiter inward close to the current Martian orbit and back to the present Jovian orbit during planet formation stage. This would have caused massive scattering of asteroids and icy planetesimals, delivering  $5 - 10 M_{\text{oceans}}$  of water. Please note, that also alternative scenarios are studied and all water delivery models are hotly debated (Genda, 2016).

Besides water, organic material as basic building blocks for life could have been deliv-

ered by impacts to Earth. Analysis of meteorite fragments show large amounts of organic materials, as for example amino acids. Those molecules are the base for proteins, the building blocks for cells and life as we know it. The *lithopanspermia* theory even considers an interplanetary transfer of rock-embedded life, ejected by impacts on their host planet. Here, several experiments were done on the 18-month EXPOSE-E project on the International Space Station (ISS). The LIFE experiment exposed various microbes to space conditions and showed that some microbial communities can survive those hostile space conditions. On the same project, the SEEDS experiment placed plant seeds outside the ISS and after returning them to Earth, quite a few produced viable plants. Although the 1.5-year mission is a wink compared to thousands or millions of years real travel time, where the organisms and seeds might die, their DNA could survive the journey. Shock experiments, simulating the ejection of the rocks, show the survive of microorganisms to a certain extend, boosting the theory (Yeomans, 2016) (Onofri et al., 2012) (Tepfer et al., 2012) (Meyer et al., 2011).

Although NEOs might have been an initial driver for life, obviously they can be harmful, too. A common way of describing the destructiveness of a NEO is its impact energy in

Diameter of impactor	Total NEA population	Average interval between impacts
1 m	1 billion	2 weeks
10 m	10 million	10 years
30 m	1.3 million	200 years
100 m	20,500 – 36,000	5,200 years
140 m	13,000 – 20,000	13,000 years
500 m	2,400 – 3,300	130,000 years
1 km	980 – 1000	440,000 years
10 km	4	89 million years

Table 1.1: The table shows the impact timescales and population sizes, depending on the diameter of the impactor. In particular the population sizes for small NEAs are uncertain. For the  $100 \text{ m} \leq d_{\text{NEO}} \leq 1 \text{ km}$  objects, the numbers were determined by NEOWISE infrared observations (lower number) and optical observations (higher number). Source: Yeomans (2016)

kT TNT equivalent ( $E \approx 4.2 \times 10^{12}$  J) or Hiroshima atomic bombs ( $E \approx 84 \times 10^{12}$  J). For even larger energies, MT TNT equivalent is used. Another approach is looking at the effects of the impact. In the simplest case of small meteoroids, the atmosphere acts as shield and evaporates the invaders completely. For larger bodies hitting Earth, the effects differ dramatically, depending on the object and arrival properties. They can be divided by temporal aspects in *short-term effects* and *long-term effects*, as well as by spacial aspects in *local*, *regional* and *global* (Melosh, 2007) (Pierazzo and Artemieva, 2012). An overview of caused destruction can be seen in Tab.1.2, yet the values are just rough estimates.

The short-term effects usually coincide with the local and regional damages, which are described below. An *airblast* is a shock wave in the air, produced by the body entering the atmosphere with hypervelocity, the detonation as airburst or the spread of an impact plume on ground. Although the waves weaken quickly with distance, windows can scatter, vehicles can be pushed over and even buildings and bridges can collapse by the airblast. If the NEO or pieces of it reach the ground, an *impact crater* forms, leaving nothing behind inside the crater. What is more, *ejecta* from the displaced ground totally destroys the surrounding as far as at least one more crater radius. During the impact process, about half of the kinetic energy is converted to heat and therefore a significant amount of *thermal radiation* is released. The electromagnetic energy can then ignite fires within sight of the fireball. Equally to waves in the air, a shock wave is induced from the impactor to the ground, causing *seismic shaking*. In this way, even small impactors could cause eruptions of geysers, small earthquakes and disturbances of hydrothermal systems at large distances from the impact site. As about two-thirds of Earth's surface are covered with deep-water, the most likely impact site is an ocean, where a *tsunami* would spread. As the water-wave reaches coastal area, the tsunami builds up, floats the land and sweeps vehicles and buildings away. However, the destructiveness of those waves heavily depends on the coast site conditions and they are expected to decay quicker than tsunamis by earthquakes (Melosh, 2007) (Pierazzo and Artemieva, 2012).

On the other hand, long-term effects can be mostly associated with the global effects. The only exceptional seems to be *ejecta rain back*, where pulverized target material together with ejected melt and vapor is transported into the upper atmosphere and falling back as particles onto the ground. The vapor condenses in the cold layers within hours and the released heat by condensation can be large enough to cause wildfires and burnings on unprotected animals and humans all over the world. While large particles rain down to Earth, sub-micrometer dust can stay in the atmosphere for years, called *dust*

Diameter of NEO	Energy [TNT equiv.]	Energy deposited	Potential damage
>0.3 m	2 t	upper atmosphere	Dazzling, memorable bolide or "fire-ball" seen; harmless
>1 m	100 t	upper atmosphere	Bolide explosion approaching brilliance of the Sun for a second or so; harmless, may yield meteorites
>3 m	2 kT	upper atmosphere	Blinding explosion in sky; could be mistaken for atomic bomb
>10 m	100 kT	upper atmosphere	Extraordinary explosion in sky; broken windows, but little damage on ground
>30 m	2 MT	stratosphere	Devastating stratospheric explosion; shock wave may topple trees, weak wooden houses, ignite fires within 10 km; deaths likely if in populated region
>100 m	80 MT	lower atmosphere or surface explosion affecting small region	Low-altitude or ground burst larger than biggest-ever thermonuclear weapon, regionally devastating, shallow crater roughly 1 km across
>300 m	$2 \times 10^3$ MT	local crater, regional destruction	Crater approx. 5 km across and devastation of region the size of a small nation or unprecedented tsunami
>1 km	$8 \times 10^4$ MT	major regional destruction; some global atmospheric effects	Destruction of region or ocean rim; potential worldwide climate shock – approaches global civilization-destruction level
>3 km	$1.5 \times 10^6$ MT	global	Worldwide, multi-year climate/ecological disaster; civilization destroyed (a new Dark Age), most people killed in aftermath
>10 km	$10^8$ MT	global	Mass extinction, potential eradication of human species

Table 1.2: Rough listing of destruction, caused by various NEO sizes.  
Source: Chapman (2007)

*loading of atmosphere.* The tiny particles block the sunlight, which could lead to the death of photosynthetic plants and creatures, as well as lower surface temperatures for years. Likewise, *injection of climatically active gases* as sulfate aerosols can decrease the surface temperatures too and nitrogen oxides are known to destroy the ozone layer, leading to an enhancement of dangerous UV radiation. Both substances can undergo chemical reactions to sulfuric acid or nitric acid, which is falling down as acid rain and acidifies the upper layers of the ocean. In contrast to the cooling effect, the injection of the greenhouse gas water vapor into the upper atmosphere by an oceanic impact can heat up Earth. Reactions of the vapor in the middle atmosphere again lead to the destruction of ozone and to an increase of UV radiation. Those global effects have the potential to cause mass extinctions (Melosh, 2007) (Pierazzo and Artemieva, 2012).

The question, which exact effects are caused by an impact with certain properties, is still an open research topic. Here, studying old impacts contributes to a better understanding. There are 190 confirmed impact structures worldwide, ranging from  $100 \text{ km} \leq d_{\text{crater}} \leq 10 \text{ m}$  in diameter. But also modern NEO incidents without the formation of craters can lead to more insight (Bobrowsky and Rickman, 2007) (Planetary and Space Science Centre - University of New Brunswick, 2018).

The last famous incident occurred at the city *Chelyabinsk*, Russia on February 15, 2013, where a  $d_{\text{NEO,Che}} \approx 20 \text{ m}$  asteroid with an energy of about 570 kT TNT equivalent caused the largest recorded airburst since 100 years. The object has been estimated to  $m_{\text{NEO,Che}} = 1.3 \times 10^7 \text{ kg}$  with a bulk density of  $\rho \approx 3300 \text{ kg/m}^3$ . While entering the atmosphere the fireball reached about  $-27.3$  magnitude brightness, which is brighter than the Sun. The body fragmented in the atmosphere, but did not entirely evaporate, why a few meteorites with combined 0.03 – 0.05% of the initial mass were found. Due to the shock wave, buildings started to shake, glass broke, window frames were blown out and even the collapse of a factory roof was documented. Mobile phone connection, electricity and gas supply was interrupted for a short moment due to the arriving airburst wave and the induced vibrations. It is known that people were blown down and even sunburns are recorded. In total, about 1,600 people got injured, where most had cuts and bruises from scattered glass. Luckily, there were no fatalities. Studies assume a 86% probability that the asteroid originates from the  $\nu_6$  resonance (Popova et al., 2013). The analysis of the Chelyabinsk incident indicates the complexity of an impact event and shows, that also small objects can damage the human society.

On June 30, 1908, another object entered the atmosphere above the basin of the Pod-

kamennaya *Tunguska* river, Russia and released 10 – 15 MT TNT equivalent of energy as an airburst without a crater. The result were 80 million flattened trees in an area of more than 2,000 km<sup>2</sup>, many inflamed bushes and trees and seismic waves were measured and associated with the event. Records from Europe and Asia speak about bright nights, which are expected to be the result of icy particles from a comet tail, its exploded nucleus or water vapor ejection from lower, humid atmosphere layers into dry, upper layers, which reflected light. It is not clarified yet, if the body was an asteroid or a comet, why the NEO and impact values have large uncertainties, ranging from  $60 \text{ m} \leq d_{\text{NEO,Tun}} \leq 1200 \text{ m}$  in diameter and an airburst altitude between  $6 \text{ km} \leq h \leq 10 \text{ km}$ . Due to the Tunguska event two people died, yet this low number of fatalities is accounted for by the low population density in Siberia (Longo, 2007) (Lyne, 1995) (Gritzner, 1997).

In contrast to airburst impacts, the 50,000 year old *Barringer Crater* (also called *Meteor Crater*) in Arizona, USA is the result of a ground impact. The crater has a diameter of  $d_{\text{crater,Bar}} = 1.2 \text{ km}$  and is  $z_{\text{crater,Bar}} = 170 \text{ m}$  deep. The associated iron asteroid with  $40 \text{ m} \lesssim d_{\text{NEO,Bar}} \lesssim 50 \text{ m}$  size released 6.5 MT TNT equivalent of energy in the atmosphere and 2.5 MT TNT equivalent during the ground impact. Another crater is located in Bavaria, Germany, the so-called *Ries crater* with  $d_{\text{crater,Ries}} = 24 \text{ km}$  in diameter and an age of 15.0 million years. In fact, it was a binary asteroid, since another smaller crater, the *Steinheim crater* with  $d_{\text{crater,Stein}} = 3.8 \text{ km}$  in size, is located in the west-southwest of the major impact site. The impactors are estimated to about  $d_{\text{NEO,Ries}} \approx 1.5 \text{ km}$  and  $d_{\text{NEO,Stein}} \approx 0.15 \text{ km}$  for stony densities and the released energy was in the order of  $10^5$  MT TNT. An even more important collision happened 65 million years ago, where a NEO impacted in Yucatan, Mexico and formed the largest known crater of about  $d_{\text{crater}} \approx 180 \text{ km}$ , the *Chicxulub crater*. The impactor is assumed to  $d_{\text{NEO,Yuc}} \approx 15 \text{ km}$  in size and released  $10^8$  MT TNT equivalent. This impact is considered to be the reason for the K/T event, where roughly half of the world's species disappeared, including the dinosaurs. Despite those tremendous consequences for life, it was a wonderful piece of luck for humankind, since mammals had the chance to fill the empty habitats of the extincted dinosaurs and in the end were able to evolve to the human species (Yeomans, 2016) (Melosh and Collins, 2005) (Stöffler et al., 2002) (Gritzner, 1997) (Grieve and Kring, 2007). Nowadays, such an impact would be devastating for human society.

Besides the destructive potential of near-Earth objects for our civilization, there is also a chance and future perspective, the so-called *asteroid mining*, where rare metals should be extracted from asteroids. Since many important minerals are difficult to win on Earth

by political and social issues or leading to environmental pollution, NEOs might be an alternative source. Another application is the extraction of water for life support or for in-situ propellant production. Although more work is needed to develop the necessary technologies, as propulsion systems for the huge material transport to Earth. Luxembourg regulated as first European country asteroid mining by law in 2017. The USA passed a similar law already in 2015 (Grandl and Bazso, 2013) (Fraser, 2013) (Tagesschau, 2017).

As one can see, NEOs shaped the history of Earth and enabled the current human civilization. On the other hand, those bodies threaten values and humans. Moreover, there is no need of hundreds of impacts, but a single event can have the potential to erase the human species. Therefore, NEOs are boon and bane at the same time.

### 1.3 Conventional NEO mitigation

The English term *mitigation* is described by the Oxford Dictionaries (2018) as: "The action of reducing the severity, seriousness, or painfulness of something." In the case of an upcoming NEO impact this means and includes many actions, ranging from civil protection by emergency management agencies as evacuation of the impact zone or providing security advices to the public (Perna et al., 2015) to space missions by the space agencies or military to influence the approaching NEO. The latter gets most of the attention, however space missions are not necessarily the best response. The actions depend on the consequences of the upcoming impact, which can be seen in Tab.1.2. For NEOs smaller than  $d_{\text{NEO}} < 3$  m, no further actions are needed. For bodies between  $2 \text{ m} < d_{\text{NEO}} < 30 \text{ m}$  civil protection might be the best solution. For larger objects, space missions of influencing the NEO get reasonable, yet drawing a clear line is difficult, as for influencing NEOs in space many points need to be considered.

There are various attempts of how to prevent a NEO impacting Earth. Either the object can be destroyed or it can be deflected by changing its orbit. Destruction causes fragmentation and smaller pieces, though their orbit is not largely different to the original orbit, why the fragments can still hit Earth. Tiny objects are harmless, but it is difficult to assure the fragmentation in numerous very small objects. Hence, the resulting fragments might be still large enough to be hazardous and due to the spread over a larger area might cause even more damage as a single NEO. As a result, only small asteroids should be destroyed where the fragments will be small enough to burn up in the atmosphere (Gritzner and Kahle, 2004).

Deflection of a NEO leads to a miss of Earth and is divided in *continuous small-thrust* methods and *impulsive thrust* methods. The continuous small-thrust technologies might be used if the warning time is large enough, meaning a decade or more. The deflection itself takes place over a long period of several months or more. For impulsive techniques, the action happens at a single blow and might also be used if the warning times are too short for small-thrust methods. Here a possible fragmentation of the NEO must be taken into account. Until 2018 no real or test deflection has ever been performed. For the year 2022, the test mission *Asteroid Impact & Deflection Assessment* (AIDA) to a binary asteroid Didymos is planned, consisting of NASA's *Double Asteroid Redirection Test* (DART) and ESA's *Hera* mission. While the task of the ESA spacecraft is the scientific characterization, NASA's DART is a so-called kinetic impactor (Gritzner and Kahle, 2004) (Cheng et al., 2018).

The *kinetic impactor* deflection method is an impulsive thrust technique and the basic concept is very simple, making this method attractive. It is a spacecraft with a large mass, colliding with the NEO and while doing so transferring its linear momentum to the object, leading to an orbital change. Due to the impact process and crater formation on the NEO, material is ejected, causing additional momentum change, which might exceed the linear momentum transfer of the spacecraft. Yet, there is a huge uncertainty in efficiency of this technique, which arises by the uncertainty of the composition and structure of the NEO, in particular the porosity. Here, the AIDA mission should lead to more insights in the deflection efficiency. The earlier Deep Impact mission, where a spacecraft with a mass of roughly 350 kg impacted on the comet 9P/Tempel 1 with roughly  $10 \frac{\text{m}}{\text{s}}$  in 2005, was not intended to and did not cause any measurable deflection, but investigated the composition and physical properties of the outer crust and mantle (Gritzner and Kahle, 2004) (Sanchez et al., 2009) (Cheng et al., 2018).

Another impulsive method is the *nuclear interceptor*, where a nuclear stand-off explosion takes place at a certain distance to the surface of the NEO. The released energy of the detonation by a fission device is mainly carried by X-rays and device debris to the near-Earth object, where they hit the surface. For fusion reactions, neutrons are important energy carriers, too. The energy density of a nuclear interceptor is very high and nuclear explosions are well tested and known on the ground, making this technique interesting for deflection. However, there has not been a nuclear explosion test in space due to the *Limited Test Ban Treaty* and political and security concerns may rule this deflection technique out (Sanchez et al., 2009).

For the continuous small-thrust method numerous approaches are published, but none of them is well developed yet. The most advanced and studied technique here is the *gravity tractor*, where a massive spacecraft gravitationally attracts the NEO and therefore slowly pulls it into a different orbit. The challenge of this technology is to keep the spacecraft at the right distance to the NEO, as gravity acts on both and by firing the engines, to realize a fixed distance, not accidentally pushing the NEO back to its origin again. An *ion beam shepherd* spacecraft uses one of its ion thrusters to enable a particle flow of quasi neutral plasma to the NEO, where the particles transfer their momenta. The other thruster is needed to keep the spacecraft in position. *Solar sails* attached to the asteroid could use the radiation pressure of the Sun to accelerate the NEO, yet the rotation of the object could be a big problem. Acceleration by *spacecraft propulsion* would use thrust-engines on the near-Earth object surface with chemical or low-thrust propulsion, as used in conventional spacecrafts. Very similar to this concept is the *mass driver*, which uses the material of the NEO itself by shooting it into space. The result of both concepts is a net velocity opposite to the ejecta due to momentum conservation. Again, the rotation of NEOs has to be considered as the engines have to be turned on and off to not cancel the spacial shift. The *solar concentrator* sublimates the surface of the body by focused sunlight, while a *pulsed laser* generates the photons artificially on the spacecraft. The ablated material escapes into space and leads to a repulsion. The challenge is to get enough energy on a small spot for adequately heating up the material to realize a phase transition (Sanchez et al., 2009) (Gritzner and Kahle, 2004) (Bombardelli and Peláez, 2011).

As we see, there are many approaches and ideas how to deflect a threatening object. However, only the kinetic impactor and the nuclear interceptor seem realistic for the near future. Moreover, every concept has its individual open questions, problems and downsides. Therefore, we should keep on thinking to find an affordable and reliable deflection method someday.

# Chapter 2

## Near-Earth object deflection with Breakthrough Starshot

### 2.1 Breakthrough Starshot Project

*Breakthrough Starshot* is a research and engineering program of the Breakthrough Initiative (2018) to investigate and afford an unmanned space probe reaching Alpha Centauri within the timescale of one generation. The project is funded with \$100 million by numerous investors and was supported among others by Stephen Hawking until his death.

The space probe, a so-called ultra-light nanocraft with only a few grams, is planned to consist of a StarChip and a lightsail. The StarChip is a fully functional spacecraft bus, including photon thruster, communication system and a camera as payload. The light sail is a few hundred atoms thick m-scale sail, which will be illuminated by ground based light beamers with up to 100 GW total. Those phased arrays of lasers would accelerate the nanocraft to velocities of 15 – 20% of speed of light, enabling a flight time of about 20 years to reach Alpha Centauri. The acceleration is illustrated in Fig.2.1. In contrast to conventional space probes, a single StarChip should only cost as much as an iPhone and could therefore be mass-produced. This means the launch of numerous nanocrafts to ensure redundancy and coverage. Please note, despite the Breakthrough Initiative is often talking about Alpha Centauri as target in general, the red-dwarf Alpha Centauri C, also called Proxima Centauri, with the exoplanet Proxima Centauri b is investigated as primary destination (Breakthrough Initiative, 2018).

The technology is still under development and many problems have to be solved before realizing the vision of interstellar traveling nanocrafts (Breakthrough Initiative, 2018).

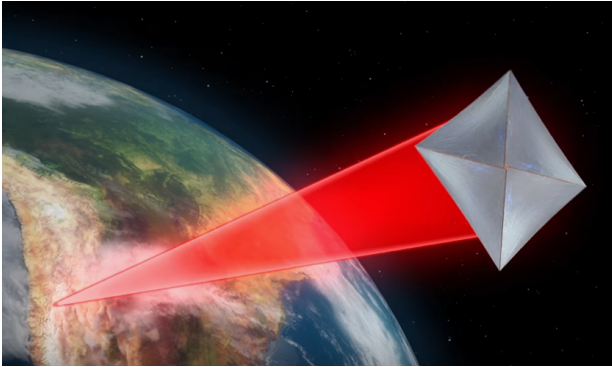


Figure 2.1: Artist illustration of a nanocraft, accelerated by Earth-based light beamers.

Source: Breakthrough Initiative (2018)

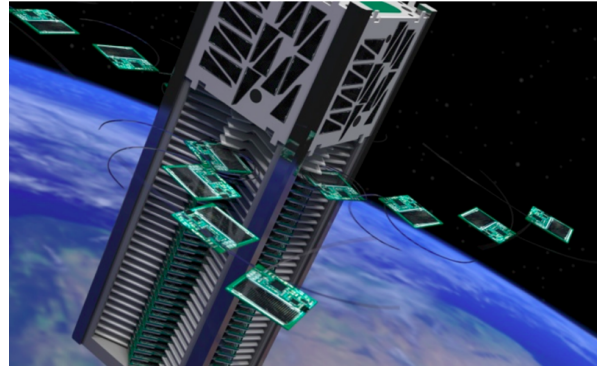


Figure 2.2: Artist illustration of the KickSat, deploying its ChipSats.

Source: Breakthrough Initiative (2018) and Ben Bishop

Therefore, there are no detailed and obviously final information about the technology, why only data from development tests and longterm goal publications can be used in this thesis.

The KickSat-1 mission, developed by Manchester et al. (2013), sent more than hundred so-called Sprite ChipSats on-board a CubeSat-based deployer to a low-Earth orbit in the year 2014. The deployment procedure is illustrated in Fig.2.2. A single ChipSat had a mass of  $m_{\text{KS,Chip}} = 5 \times 10^{-3}$  kg and a cross section of  $A_{\text{KS,Chip}} = 3.5 \text{ cm} \times 3.5 \text{ cm}$ . From those values, we can calculate a Sprite areal density of  $\Sigma_{\text{KS,Chip}} = 4.08 \frac{\text{kg}}{\text{m}^2}$ . Unfortunately, KickSat-1 failed in deploying its payload, why a second mission, KickSat-2, should now release the tiny spacecrafts (Jones, 2016). The missions should improve and push the technology for low-cost ChipSat projects. The Breakthrough Initiative (2018) lists those ChipSats in their list of research, why we use the areal density for further calculations.

Parkin (2018) introduces a system model for Breakthrough Starshot, specifying and calculating the nanocrafts and laser properties. Here, the mass of the StarChip was set to  $m_{\text{BS,Chip}} = 1 \times 10^{-3}$  kg. If we use the areal density of the Sprite ChipSats as a standard value we find a chip size of approximately  $A_{\text{BS,Chip}} \approx 1.57 \text{ cm} \times 1.57 \text{ cm}$ . From the LeitOn GmbH (2018) website we can determine a circuit board thickness  $z_{\text{BS,Chip}} \approx 1.5 \text{ mm}$  and bulk density of  $\rho_{\text{BS,Chip}} \approx 2720 \frac{\text{kg}}{\text{m}^3}$  for a FR4 4-layer 75% copper configuration. Here, the components on circuit board are not included, yet we can take those values as a first rough estimate.

Parkin (2018) continues with the whole nanocraft, consisting of the StarChip and light sail. It has a mass of  $m_{\text{BS,NC}} = 3.8 \times 10^{-3}$  kg with a sail diameter of  $d_{\text{KS,NC}} \approx d_{\text{BS,sail}} = 4.2 \text{ m}$  and sail thickness of  $z_{\text{KS,sail}} = 76 \text{ nm}$ . Finally, we get a bulk density of the sail

$\rho_{\text{BS,sail}} \approx 2660 \frac{\text{kg}}{\text{m}^3}$  and of the nanocraft  $\rho_{\text{BS,NC}} \approx 2670 \frac{\text{kg}}{\text{m}^3}$ .

The initial sail displacement from the laser source is determined to be  $d_{\text{ini,NC}} = 60 \times 10^3$  km, which is way above the geostationary orbit at roughly  $D_{\text{GEO}} \approx 36 \times 10^3$  km. The final velocity of  $v_{\text{BS,NC}} = 0.2c$  is reached at  $D_{\text{full,NC}} = 73\text{ls} \approx 0.15$  AU, as Parkin (2018) points out. Here,  $c$  stands for the speed of light in free space. Those 0.15 AU are a more conservative but maybe more realistic value as the earlier aimed few million km (Burkert, private communication, 2017).

Brashears et al. (2015) and Brashears et al. (2016) suggest also a concept of a circuit board as a tiny spacecraft, here referred to as BoardSats in general and as WaferSats for the specific concept. They introduce a photon thruster at each corner of the circuit board for attitude control. Here, 10 mW thrusters are assumed with  $3.3 \frac{\text{mN}}{\text{W}}$ , which results in an exerted force of  $F_{\text{photon}} = 33$  pN per thruster (Lubin, 2016).

## 2.2 Deflection concept

The Breakthrough Starshot technology might be also used for NEO deflection. The basic idea is to shoot a nanocraft to a dangerous object in route of collision with the Earth, instead of Proxima Centauri. The space probe acts here as a projectile, which impacts the threatening object and transfers its momentum. In addition to the moment, a large amount of energy is released, which might result in sublimation of parts of the body. Both effects change the velocity of the NEO, leading to a miss of Earth.

In the following, we are speaking of projectiles and not of nanocrafts, ChipSats or BoardSats. The acceleration process is similar for flying to Proxima Centauri and to a near-Earth object, yet the technology of the accelerated spacecraft might be different. For nanocrafts a camera, communication system, attitude control, power system, etc. is crucial for fulfilling the mission. The projectiles simply impact on a body, where velocity and mass is the key point in accomplishing the task of NEO deflection. A camera, communication system, attitude control, etc. are not essential, though might improve the hit probability of a projectile.

Conventional kinetic impactors deal with high-mass spacecrafts in the order of tons and low velocities with tens of kilometers per second. In contrast, the projectiles have only a mass of a few grams but with a fraction of the speed of light very high velocities, compensating the low mass. This method does not fit in the classical classification schemes, as the momentum transfer for a single impact is impulsive, but if more projectiles are used,

the deflection occurs continuously over a longer period.

There are clear advantages of the Starshot concept over the conventional impactor. The kinetic impactor has a long orbital travel time from Earth to its destination, ranging from years to decades. Besides, they have to fit to certain launch windows, if a maximized launch mass is aimed, limiting and delaying the deflection procedure once more. If failures occur during travel or impact, leading to the failing of the mission, other impactors must be launched with the same schedule issues again.

The situation is very different for Starshot projectiles, which can reach nearly every place in the inner Solar System in a roughly linear path almost immediately due to its very high velocity. Nanocrafts, placed in space for the main mission, might be instantly used for planetary defense. An off target shot of one or more projectiles leads not to a failing of the mission, since it is easy to place thousands of additional projectiles in space without considering any launch window issues. Hence, we would keep on shooting until Earth is safe. Finally, the laser facility should be build anyways for the main mission, why no significant additional costs for planetary defense have to be spend.

For the acceleration of the projectiles and nanocrafts, very strong light beamers are needed, which might directly target and illuminate a NEO and by surface ablation change its orbit. As the energy of the lasers would be directly transported to the object without energy conversion to kinetic energy, a higher efficiency could be realized. Concepts of

$m_p$ [kg]	$d_p$ [m]	$\rho_p$ [ $\frac{\text{kg}}{\text{m}^3}$ ]	$F_{p,\text{photon}}$ [pN]
$3.8 \times 10^{-3}$	4.2	2670	33

Table 2.1: The specification of the full nanocrafts, further called projectiles with the index  $p$ . If not explicitly mentioned in the text, the above given values are used for further calculations.

$v_p$	$D_{p,\text{ini}}$	$D_{p,\text{full}}$
$0.2c$	$60 \times 10^3$ km	0.15 AU

Table 2.2: The specification of the Breakthrough Starshot deflection method. If not explicitly mentioned in the text, the above given values are used for further calculations.

NEO deflection by direct energy are developed too, as mentioned in Sec.1.3. However, by using lasers we have to deal with the beam divergence, why the energy density of the lasers decreases rapidly with increasing distance. For the large distances of the inner Solar System, the energy densities of conventional lasers technologies are far too low to cause a notable effect on the illuminated body. In contrast, the accelerated projectiles keep their energy density due to the nearly constant kinetic energy independently of the distance to the near-Earth object, why the almost same amount of energy can be transported to every place in the Solar System.

The exact specifications for the projectiles and the Breakthrough Starshot deflection are taken from publications about Breakthrough Starshot or related topics, described in Sec.2.1 and are listed in Tab.2.1 and Tab.2.2. Please note, this work is neither intended to develop new technology for Breakthrough Starshot, nor to tackle the unsolved engineering challenges. We merely adopt the current and intended future technology to study, if planetary defense would be physically feasible with the help of the Breakthrough Starshot.

## 2.3 Required velocity change

If a NEO should be deflected, it must be pushed out of its original path, meaning its momentum must be changed at a time  $t$  before the impact. However, instead of considering the required momentum change, we calculate the required velocity change  $\Delta v_r(t)$  to deflect those objects, since the velocity change is a physical quantity independent of the mass of the NEOs.

A very simple approach of  $\Delta v_r(t)$  is based on a hypothetical linear movement of the near-Earth object:

$$\Delta v_{r,\text{lin}}(t) = \frac{b_{\oplus}}{-t} = \frac{R_{\oplus}}{-t} \sqrt{1 + \frac{2GM_{\oplus}}{R_{\oplus}v_{\infty}^2}} . \quad (2.1)$$

Here, we use  $t \leq 0$  as definition for the time before the impact. The impact happens at  $t = 0$  if the NEO was not deflected by a distance of

$$b_{\oplus} = R_{\oplus} \sqrt{1 + \frac{2GM_{\oplus}}{R_{\oplus}v_{\infty}^2}} , \quad (2.2)$$

which is the effective radius of the Earth, including the gravitational focusing, as described by Valsecchi et al. (2003).  $G$  is the gravitational constant,  $M_{\oplus}$  the mass of Earth and  $R_{\oplus}$  the radius of Earth. A typical value for  $v_{\infty}$ , the unperturbed encounter velocity of the

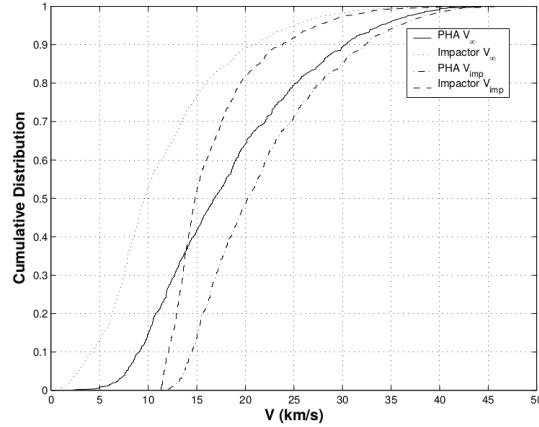


Figure 2.3: Normalized cumulative number of a potential hazardous asteroid population and impactor population, depending on their encounter and impact velocity. Impactors have lower velocities as PHAs. For the impact velocity the escape velocity of Earth is taken into account, causing higher values as the pure encounter velocity.

Source: (Chesley and Spahr, 2004)

NEO on Earth, for impacting near-Earth asteroids, can be taken from Fig.2.3, derived by Chesley and Spahr (2004). A visually estimated mean value is roughly  $\bar{v}_\infty \approx 12 \frac{\text{km}}{\text{s}}$ , leading to

$$\Delta \bar{v}_{r,\text{lin}}(t) = \frac{0.273 \frac{\text{m}}{\text{s}}}{-t} \quad (2.3)$$

with  $t$  in years. However, the curved nature of the orbital movement is not considered, why this linear approach is only valid shortly before the impact on Earth or for orbits with very high eccentricities, where the segment of the orbit is almost straight. Nevertheless, it can be used as a first rough estimate.

Carusi et al. (2002) determined a  $\Delta v_r(t)$  along the track of the NEO, which changes the semi-major axis. It additionally depends on the semi-major axis  $a_{\text{NEO}}$  of the object, the distance  $D_{\text{NEO,Sun}}$  of the object to the Sun during the deflection process and the angle  $\theta$  between the geocentric velocity of the incoming object and the heliocentric velocity of Earth:

$$\Delta v_{r,\text{par}}(t) = \frac{b_\oplus \sqrt{D_{\text{NEO,Sun}}}}{(-3tv_\infty \sin(\theta) + 2b_\oplus) \sqrt{a_{\text{NEO}}(2a_{\text{NEO}} - D_{\text{NEO,Sun}})}} \quad (2.4)$$

The variables  $v_\infty$  and  $\theta$  are not independent but depend on the orbital elements of the NEO and therefore among others on  $a_{\text{NEO}}$ . We can use the work of Valsecchi et al. (2003) to eliminate

$$v_\infty = \sqrt{3 - \frac{1}{a_{\text{NEO}}} - 2\sqrt{a_{\text{NEO}}(1 - e_{\text{NEO}}^2)} \cos i_{\text{NEO}}} \quad (2.5)$$

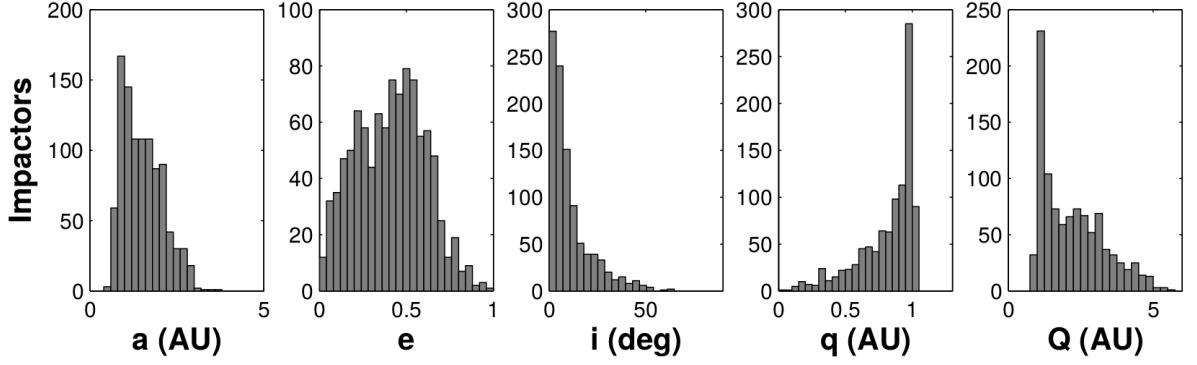


Figure 2.4: Semi-major axis  $a$ , eccentricity  $e$ , inclination  $i$ , perihelion  $q$  and aphelion  $Q$  distribution of an impactor population.

Source: (Chesley and Spahr, 2004)

and

$$\theta = \arccos \left( \frac{\sqrt{a_{\text{NEO}}(1 - e_{\text{NEO}}^2) \cos i_{\text{NEO}} - 1}}{v_{\infty}} \right) . \quad (2.6)$$

$i_{\text{NEO}}$  is the inclination and  $e_{\text{NEO}}$  the eccentricity of the NEO orbit. Please note, the equations Eq.(2.4) – Eq.(2.6) were derived in a geocentric reference frame with a gravitational constant  $G = 1$ , mass of the Sun  $M_{\odot} = 1$ , semi major axes of Earth  $a_{\oplus} = 1$ , orbital period of Earth  $T_{\oplus} = 2\pi$ , the heliocentric velocities of Earth  $v_{\oplus} = 1$  and of the NEO  $v_{\text{NEO}} = 1$ . Hence, a factor of  $2\pi \text{AU/yr}$  must be multiplied to Eq.(2.4) to get  $\Delta v_{\text{r,par}}(t)$  in SI-units. As the result depends on the orbital elements and the heliocentric distance of the body, the required velocity change is different for every NEO and for every position of the object. Therefore Chesley and Spahr (2004) determined a geometric mean  $\Delta \bar{v}_{\text{r,par}}(t)$  by using the formulas Eq.(2.4) – Eq.(2.6) and their impactor population, shown in Fig.2.4:

$$\Delta \bar{v}_{\text{r,par}}(t) = \frac{0.035 \frac{\text{m}}{\text{s}}}{-t} . \quad (2.7)$$

Here, the time  $t$  before the impact is in years. Similar to the geometric mean, we can calculate a realistic upper and lower limit, using extreme values of Fig.2.4. We choose  $a_{\text{b}} = 4.5 \text{ AU}$ ,  $e_{\text{b}} = 0.95$ ,  $i_{\text{b}} = 90^\circ$ ,  $D_{\text{NEO,Sun,l}} = q = a_{\text{b}}(1 - e_{\text{b}}^2)$  for a realistic best case and  $a_{\text{w}} = 4.5 \text{ AU}$ ,  $e_{\text{w}} = 0.95$ ,  $i_{\text{w}} = 0^\circ$ ,  $D_{\text{NEO,Sun,w}} = Q = a_{\text{w}}(1 + e_{\text{w}}^2)$  for a realistic worst case. The distances to the Sun are the perihelion  $q$  and aphelion  $Q$ , as described by Walter (2012). The limits are therefore given as

$$\Delta v_{\text{r,par,b}}(t) = \frac{0.098 \frac{\text{m}}{\text{s}}}{(-3tv_{\infty} \sin(\theta) + 2b_{\oplus})} \quad (2.8)$$

and

$$\Delta v_{r,\text{par},w}(t) = \frac{3.835 \frac{\text{m}}{\text{s}}}{(-3tv_{\infty} \sin(\theta) + 2b_{\oplus})} \quad (2.9)$$

with once more  $t$  in years. Nevertheless, there might always be rare extreme outliers which might have higher or lower  $\Delta v_{r,\text{par}}(t)$ .

As mentioned before, for Eq.(2.7) – Eq.(2.9) the required velocity change must occur parallel to the movement, yet this is not the general case for the deflection with unguided projectiles, sent in an almost straight line from Earth to the NEO. If only few projectiles are needed for a successful deflection, we can wait for proper constellations. If numerous projectiles must be shot and therefore the body has to be under constant fire, only a fraction of the transferred momentum changes the velocity parallel to the movement of the near-Earth objects. Therefore, to get even more realistic estimates, we can use

$$\Delta v_{r,\text{ang}}(t) = \frac{\Delta v_{r,\text{par}}(t)}{\cos(\bar{\alpha})} \quad , \quad (2.10)$$

where  $\alpha$  is the angle between the Earth-NEO line and the movement direction of the NEO and  $\bar{\alpha}$  the mean value. This value can be determined with a numeric simulation, where the NEO position, Earth position and  $\alpha$  is computed. Here, an interval of 50 years was chosen, starting at  $t_{\text{start}} = -60$  yr and stopping at  $t_{\text{stop}} = -10$  yr before the impact on Earth, to get a realistic mean which is not biased by the final impact approach. For the worst and best limit, where we use certain orbits, we get a specific  $\alpha$ , while for the general case we use

$t = -25$ yr	$\Delta \bar{v}_{r,\text{lin}}(t) \left[ \frac{\text{m}}{\text{s}} \right]$	$\Delta \bar{v}_r(t) \left[ \frac{\text{m}}{\text{s}} \right]$	$\Delta v_{r,b}(t) \left[ \frac{\text{m}}{\text{s}} \right]$	$\Delta v_{r,w}(t) \left[ \frac{\text{m}}{\text{s}} \right]$
–	$1.09 \times 10^{-2}$	–	–	–
par	–	$1.40 \times 10^{-3}$	$9.83 \times 10^{-4}$	$4.42 \times 10^{-2}$
ang	–	$2.35 \times 10^{-3}$	$1.18 \times 10^{-3}$	$5.27 \times 10^{-2}$

Table 2.3: The table shows the various estimates for the required velocity change to deflect a near-Earth object 25 years before impact. The first approach with only one result is based on a linear path of the NEO, while the second approach of all other results takes the orbit of the NEO into account. *par* stands for the pure parallel velocity change, while *ang* takes the non-perfect constellation of the NEO and Earth into account. The *w* and *b* indices stand for the worst and best case, while the other values are based on geometrical mean values.

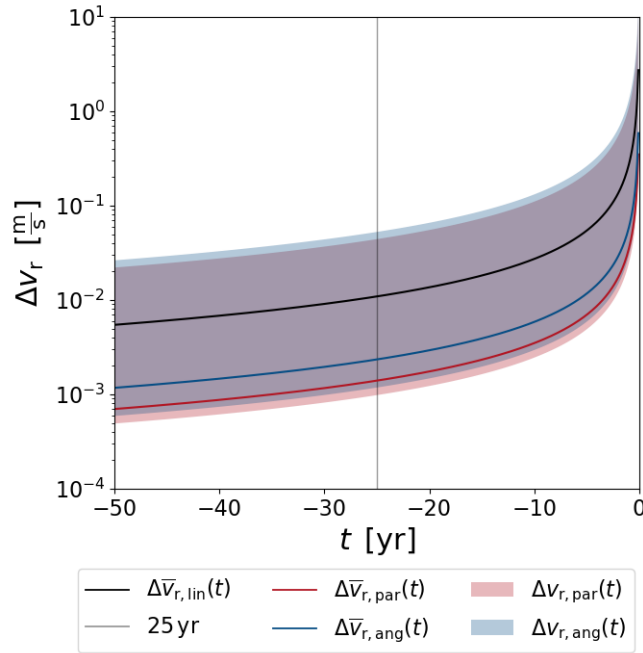


Figure 2.5: The required velocity change  $\Delta v_r$  of a NEO for a successful deflection depends on the time  $t$  before the impact. The black *lin* line shows a linear approach, while the blue and red take the orbital nature into account and are determined by geometric mean values of an impactor population. For the red *par* line, the velocity change has to occur parallel to the NEO movement, while the blue *ang* takes a mean angle between the velocity change and the movement into account. The areas show the wide spread of the value for different orbits with a realistic upper and lower limit. More extreme values could rarely occur.

the synthetic impactor population of Chesley and Spahr (2004). We obtain  $\bar{\alpha}_w = 33.8^\circ$ ,  $\bar{\alpha}_b = 33.0^\circ$  and  $\bar{\alpha}_{\text{gen}} = 53.4^\circ$ . The code and the impactor population is explained in more detail in App.A.

The evolution of the various  $\Delta v_r(t)$  can be seen in Fig.2.5. Now we pick a specific time  $t_{\text{def}} = -25$  yr before the impact to deflect the NEO. The resulting  $\Delta v_r(-25$  yr) are summarized in Tab.2.3. One can notice, that the linear approach is always larger than the geometrical mean values and the increase by the additional  $\alpha$  is relatively small compared to the difference of the different approaches.

For all  $\Delta v_r(t)$  above, no close encounter with any planet or additional perturbation by collisions are taken into account. As pointed out by Carusi et al. (2002), close encounters, where a slightly different approach can lead to a very different orbit after the encounter, lower the  $\Delta v_r(t)$ .

The situation for long periodic comets is quite different, since their orbital parameters

are much extremer as the ones we used. Therefore the deflection could not happen during several orbits but has to take place during the approach on Earth. Here, Eq.(2.2) would be more appropriate. Since NEAs dominate the NEOs, we will continue with Eq.(2.10) and  $\bar{\alpha}_{\text{gen}} = 53.4^\circ$  for any calculations depending on the required velocity change:

$$\Delta v_r(t) = \frac{0.035 \frac{\text{m}}{\text{s}}}{-t \cos(53.4^\circ)} \quad . \quad (2.11)$$

## 2.4 Deflection by single event momentum transfer

As pointed out by Benacquista and Romano (2018), the linear momentum of a system is conserved, why a perfectly inelastic collision can be described as

$$v_{\text{NEO}} m_{\text{NEO}} + v_p m_p = v_{\text{def}} (m_{\text{NEO}} + m_p) = \text{const.} \quad (2.12)$$

with the mass  $m$  and the velocity  $v$  of the NEO, the projectile  $p$  and both together after the deflection action, here marked as *def*. For relativistic mechanics the linear momentum is also conserved, yet the Lorentz factor  $\gamma(v) = 1/\sqrt{1 - v^2/c^2}$  with the speed of light in free space  $c$  must be added, leading to

$$\gamma(v_{\text{NEO}}) v_{\text{NEO}} m_{\text{NEO}} + \gamma(v_p) v_p m_p = \gamma(v_{\text{def}}) v_{\text{def}} (m_{\text{NEO}} + m_p) = \text{const.} \quad . \quad (2.13)$$

As we switch into the frame of reference of the NEO with  $v_{\text{NEO}} = 0 \frac{\text{m}}{\text{s}}$ , where we consider  $v_p - v_{\text{NEO}} \approx v_p$  since  $v_p \gg v_{\text{NEO}}$  and  $m_{\text{NEO}} \gg m_p$ , we get a velocity change of

$$\Delta v(m_{\text{NEO}}) \approx \frac{\gamma(v_p) v_p m_p c}{\sqrt{(m_{\text{NEO}} c)^2 + (\gamma(v_p) v_p m_p)^2}} \quad . \quad (2.14)$$

Comparing the summands in the square root for characteristic values reveals that the term  $(m_{\text{NEO}} c)^2$  dominates the sum, why an even more simplified version can be written as

$$\Delta v(m_{\text{NEO}}) \approx \frac{\gamma(v_p) v_p m_p}{m_{\text{NEO}}} \quad . \quad (2.15)$$

This formula describes the velocity change  $\Delta v(m_{\text{NEO}})$  of a NEO with mass  $m_{\text{NEO}}$  by linear momentum transfer from a light, relativistic moving object with mass  $m_p$  and velocity  $v_p$ . In contrast to the required velocity change  $\Delta v_r(t)$ , the achieved velocity change  $\Delta v(m_{\text{NEO}})$  depends on the mass of the near-Earth object and hence on its size and bulk density.

For a conventional kinetic impactor Eq.(2.12) is adequate and leads with a velocity  $v_{ki}$  and mass  $m_{ki}$  of an impactor to

$$\Delta v(m_{\text{NEO}}) = \frac{v_{ki}m_{ki}}{m_{\text{NEO}} + m_{ki}} \approx \frac{v_{ki}m_{ki}}{m_{\text{NEO}}} \quad (2.16)$$

in the NEO frame of reference. As before, we find  $m_{ki} \ll m_{\text{NEO}}$  and simplify the sum  $m_{\text{NEO}} + m_{ki} \approx m_{\text{NEO}}$ .

Now we can use the intended values listed in Tab.2.1 and Tab.2.2 for the projectiles in Eq.(2.15) and characteristic values  $v_{ki} = 10 \frac{\text{km}}{\text{s}}$  and  $m_{ki} = 10^3 \text{ kg}$  for a typical kinetic impactor in Eq.(2.16). The results can be seen in Fig.2.6, where the colored lines show the achieved velocity change by projectiles and a conventional kinetic impactor, depending on the near-Earth object mass  $m_{\text{NEO}}$ . For the projectiles, multiple impacts were taken into account, simply taking  $n$  times the  $\Delta v$ . This means, in this model the momenta of all projectiles are transferred at a single event at the same time. In addition, the required velocity changes for  $t_{\text{def}} = -50 \text{ yr}$ ,  $t_{\text{def}} = -25 \text{ yr}$  and  $t_{\text{def}} = -10 \text{ yr}$  are indicated as horizontal lines. The vertical lines show the mass range of spherically approximated NEOs with a diameter of  $d_{\text{NEO}} = 100 \text{ m}$  and  $d_{\text{NEO}} = 1 \text{ km}$  for a very large bulk density range of  $1000 \frac{\text{kg}}{\text{m}^3} \leq \rho_{\text{NEO}} \leq 8000 \frac{\text{kg}}{\text{m}^3}$ .

About 40 projectiles are needed to achieve the same velocity change as a kinetic impactor, independent of the mass of the NEO. Due to the logarithmic plot, this is not easy to notice. The velocity change of a single projectile is sufficient for deflecting a stony NEO with diameter of 30 m about 10 yr before the impact on Earth, a 40 m with roughly 25 yr or with an even earlier deflection of 50 yr, a 50 m stony object can be handled. For stony NEOs with size 100 m roughly 10 projectiles 40 yr or 100 projectiles 5 yr in advance are needed. The km-sized objects are more problematic, since even the  $\Delta v$  of 1000 projectiles are not sufficient in a reasonable time before the impact. Here, the kinetic impactor and the projectiles fail in deflecting large near-Earth objects, as only the pure momentum transfer is considered.

Combining the required velocity change of Eq.(2.11) with the achieved velocity change of Eq.(2.15) and Eq.(2.16) gives the deflection time  $t_{\text{def}}$ , when the deflection process must happen to barely save Earth with the projectiles and a conventional impactor:

$$t_{\text{def,p}}(m_{\text{NEO}}) = -\frac{0.035 \frac{\text{m}}{\text{s}}}{\cos(53.4^\circ)} \frac{m_{\text{NEO}}}{\gamma(v_p)v_p m_p} \quad , \quad (2.17)$$

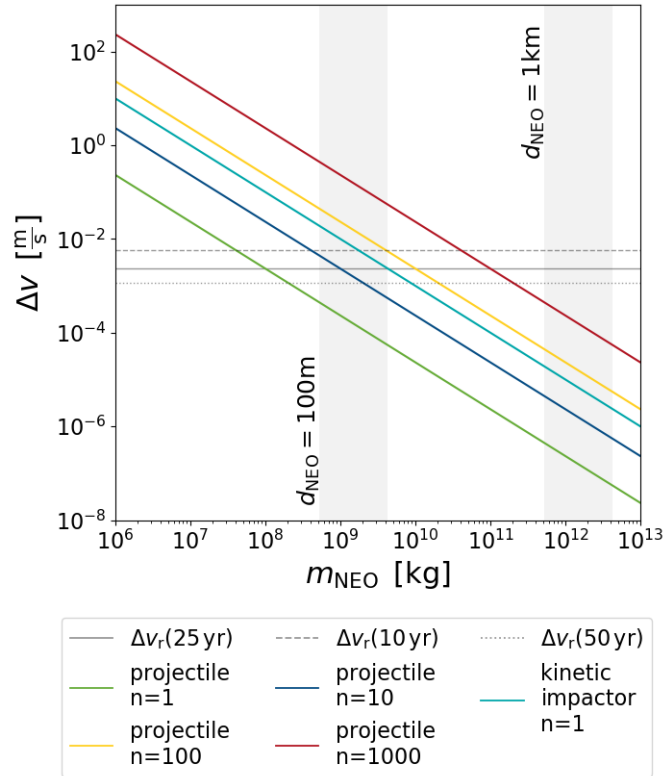


Figure 2.6: The plot shows the achieved velocity change  $\Delta v$  of a NEO by the momentum transfer of projectile impacts with  $v_p = 0.2c$  and  $m_p = 3.8\text{ g}$  as a function of the NEO mass  $m_{\text{NEO}}$ . The various colors represent different numbers of impacts, where for more than one projectile the total  $\Delta v$  is derived by multiplying a single impact by  $n$ . The cyan curve shows a conventional kinetic impactor with  $v_{\text{ki}} = 10 \frac{\text{km}}{\text{s}}$  and  $m_{\text{ki}} = 1\text{ t}$ . The horizontal lines give the approximated required velocity change for various deflection times. The vertical gray domains show the masses of NEOs with certain diameters and densities ranging from  $1 \frac{\text{kg}}{\text{dm}^3} \leq \rho_{\text{NEO}} \leq 8 \frac{\text{kg}}{\text{dm}^3}$ . About 40 projectiles have the same efficiency as a kinetic impactor, yet km-sized objects are neither by a kinetic impactor, nor by 1000 projectiles deflectable. A reasonable number of 100 projectiles could deflect a 100-m-sized object.

$$t_{\text{def,ki}}(m_{\text{NEO}}) = -\frac{0.035 \frac{\text{m}}{\text{s}}}{\cos(53.4^\circ)} \frac{m_{\text{NEO}}}{v_{\text{ki}} m_{\text{ki}}} \quad . \quad (2.18)$$

Both can be seen in Fig.2.7, where the deflection time is plotted against the mass of the body  $m_{\text{NEO}}$ . The various colors show the different projectile numbers  $n$  and the gray areas show again the mass range for certain spherically approximated NEOs. As already mentioned before, a single projectile has trouble in deflecting objects in order of several ten meters. For higher numbers of projectiles, the velocity change can be sufficient for even

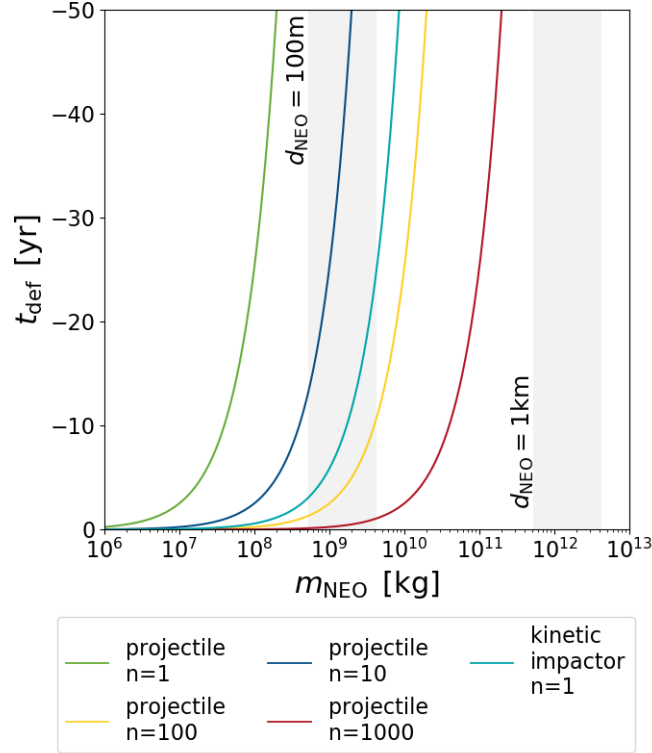


Figure 2.7: The plot shows the point of time for deflection  $t_{\text{def}}$  of a single event momentum transfer of all projectiles, depending on the mass  $m_{\text{NEO}}$  of the object. The various colors represent the different numbers of projectiles  $n$  and the cyan curve shows a conventional kinetic impactor. The vertical gray domains show the masses of NEOs with certain diameters and densities ranging from  $1 \frac{\text{kg}}{\text{dm}^3} \leq \rho_{\text{NEO}} \leq 8 \frac{\text{kg}}{\text{dm}^3}$ . For a reasonable timescale of maximum 50 yr, a single projectile might be applicable for 10-m bodies. 100-m objects are only deflectable by 10 or more projectiles. The km-regime is not deflectable with a reasonable number  $n$  of impacts. As the bulk density increases, objects with the same size get very difficult to deflect, which can be seen for  $n=10$ , where  $t_{\text{def}}$  rises very steep inside the gray shaded area.

100 m objects in reasonable time scales of a few decades. On the other hand, km-sized objects seem not deflectable by pure momentum transfer, as even 1000 projectiles 50 yr before the impact are to less.

Please note, in contrast to the kinetic impactor, where the full  $\Delta v$  is achieved at once, the deflection with multiple projectiles is stretched over a certain time range. This is not taken into account in Fig.2.6 and Fig.2.7. Therefore all projectiles must hit the NEO until the given  $t$  where to deflection activity ends, otherwise the  $\Delta v_r$  rises.

## 2.5 Deflection by constant fire

As the required velocity change can hardly be realized by a single shot, we have to take into account that it changes over time. For modeling the evolution of  $\Delta v_r(t)$  we start with the unperturbed object

$$\Delta v_{r,0}(t < t_{\text{def},1}) = \frac{0.035 \frac{\text{m}}{\text{s}}}{-t \cos(53.4^\circ)} \quad . \quad (2.19)$$

As the first projectile hits at  $t_{\text{def},1}$ , the required velocity change is lowered by the achieved  $\Delta v(m_{\text{NEO}})$  to

$$\Delta v_{r,1}(t_{\text{def},1}) = \Delta v_{r,0}(t_{\text{def},1}) - \Delta v(m_{\text{NEO}}) = \frac{0.035 \frac{\text{m}}{\text{s}}}{-t_{\text{def},1} \cos(53.4^\circ)} - \Delta v(m_{\text{NEO}}) \quad . \quad (2.20)$$

Below, we will use Eq.(2.14) for  $\Delta v(m_{\text{NEO}})$ . The further evolution is now given by another function. As the required velocity change rises over time, it will always be only the fraction  $f_1$  achieved at  $t_{\text{def},1}$ , since this perturbation is growing with time, too:

$$\begin{aligned} \Delta v_{r,1}(t_{\text{def},1} \leq t) &= f_1 \frac{0.035 \frac{\text{m}}{\text{s}}}{-t \cos(53.4^\circ)} = \frac{\Delta v_{r,1}(t_{\text{def},1})}{\Delta v_{r,0}(t_{\text{def},1})} \frac{0.035 \frac{\text{m}}{\text{s}}}{-t \cos(53.4^\circ)} \\ &= \Delta v_{r,1}(t_{\text{def},1}) \frac{t_{\text{def},1}}{t} = \left( \frac{0.035 \frac{\text{m}}{\text{s}}}{-t_{\text{def},1} \cos(53.4^\circ)} - \Delta v(m_{\text{NEO}}) \right) \frac{t_{\text{def},1}}{t} \quad . \end{aligned} \quad (2.21)$$

As soon as the second projectile hits, the new evolution is given by

$$\Delta v_{r,2}(t_{\text{def},2}) = \Delta v_{r,1}(t_{\text{def},2}) - \Delta v(m_{\text{NEO}}) \quad (2.22)$$

and the next function is

$$\begin{aligned} \Delta v_{r,2}(t_{\text{def},2} \leq t) &= f_2 \frac{0.035 \frac{\text{m}}{\text{s}}}{-t \cos(53.4^\circ)} = \frac{\Delta v_{r,2}(t_{\text{def},2})}{\Delta v_{r,0}(t_{\text{def},2})} \frac{0.035 \frac{\text{m}}{\text{s}}}{-t \cos(53.4^\circ)} \\ &= \Delta v_{r,2}(t_{\text{def},2}) \frac{t_{\text{def},2}}{t} \\ &= \left[ \left( \frac{0.035 \frac{\text{m}}{\text{s}}}{-t_{\text{def},1} \cos(53.4^\circ)} - \Delta v \right) \frac{t_{\text{def},1}}{t_{\text{def},2}} - \Delta v \right] \frac{t_{\text{def},2}}{t} \\ &= \frac{0.035 \frac{\text{m}}{\text{s}}}{-t \cos(53.4^\circ)} - \frac{t_{\text{def},1}}{t} \Delta v(m_{\text{NEO}}) - \frac{t_{\text{def},2}}{t} \Delta v(m_{\text{NEO}}) \\ &= \frac{0.035 \frac{\text{m}}{\text{s}}}{-t \cos(53.4^\circ)} - \frac{\Delta v(m_{\text{NEO}})}{t} \sum_{i=1}^2 t_{\text{def},i} \quad . \end{aligned} \quad (2.23)$$

As we continue this series, we get

$$\begin{aligned} \Delta v_{r,n}(t_{\text{def},n} \leq t) &= f_n \frac{0.035 \frac{\text{m}}{\text{s}}}{-t \cos(53.4^\circ)} = \Delta v_{r,n}(t_{\text{def},n}) \frac{t_{\text{def},n}}{t} \\ &= \frac{0.035}{-t \cos(53.4^\circ)} - \frac{\Delta v(m_{\text{NEO}})}{t} \sum_{i=1}^n t_{\text{def},i} . \end{aligned} \quad (2.24)$$

To get the evolution of the required velocity change, we recursively lower  $\Delta v_r(t)$  by  $\Delta v$  with a certain shot frequency  $s$  and let the resulting curve change as described in Eq.(2.24). This can be seen in Fig.2.8, where the solid, colored lines show the stepwise evolution,

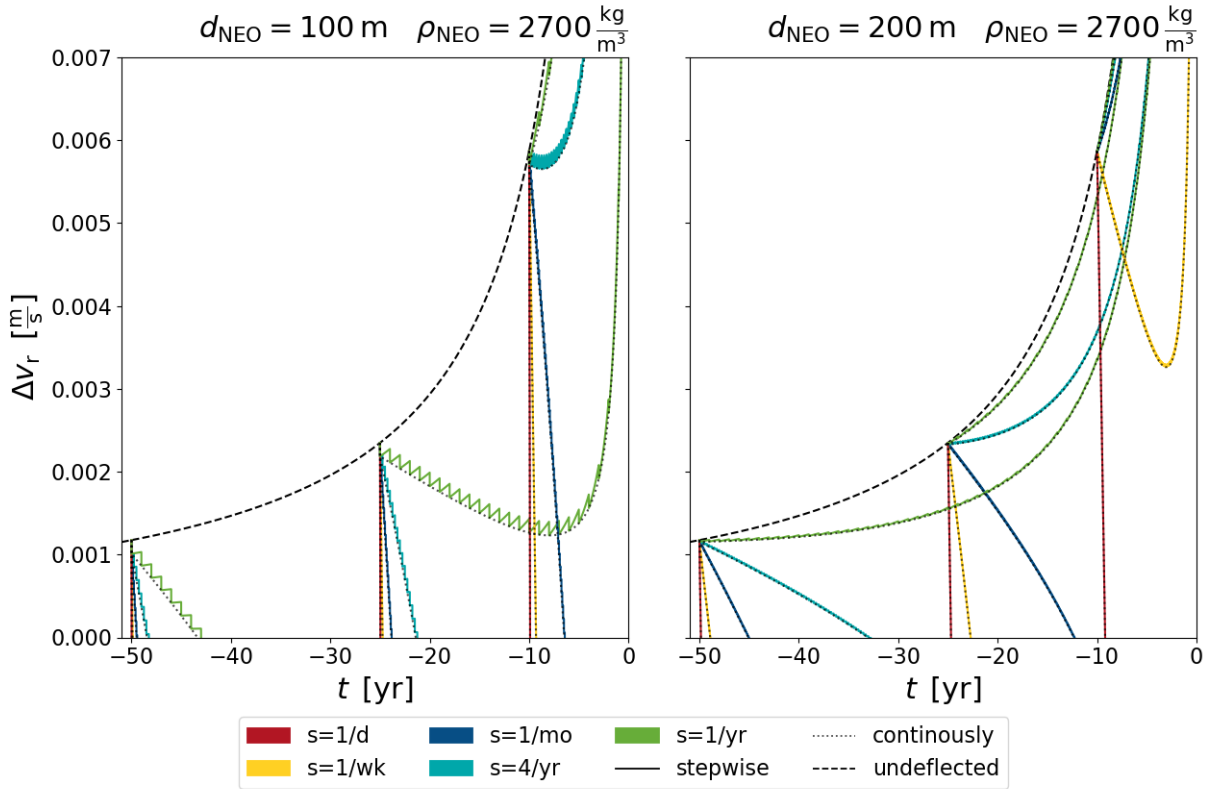


Figure 2.8: The plots show the evolution of the required velocity change  $\Delta v_r$  to deflect a NEO as function of the time  $t$ . The solid lines show the stepwise impulsive impacts, leading to zigzag shaped curves. As soon as  $\Delta v_r \leq 0 \frac{\text{m}}{\text{s}}$ , the NEO is deflected. The evolution of the various curves depend on the first projectile impact  $t_{\text{def},1}$ , the shot rate  $s$  and the mass of the NEO. The black dotted curves, which are in contact with the colored lines, show the corresponding continuous smoothed function. For a later  $t_{\text{def},1}$ , higher shot rates are needed to successfully deflect a NEO. A change from  $d_{\text{NEO}} = 100 \text{ m}$  to  $d_{\text{NEO}} = 200 \text{ m}$  leads already to very different results.

depending on  $s$  and the deflection starting time  $t_{\text{def},1}$ , when the first projectile hits the spherically approximated NEO. Two different object sizes are treated. With respect to  $s$  the unit yr means year, mo means month, wk means week and d means day. As soon as the function gets negative, the object is deflected. Some curves steeply decrease, while others continuously rise. However, for some configurations as the  $d_{\text{NEO}} = 100 \text{ m}$ ,  $t_{\text{def},1} = 25 \text{ yr}$ ,  $s = 1/\text{yr}$  the  $\Delta v_r$  is shrinking at first, but the slope is too flat and therefore the curve flips and rises again, leading to an impact on Earth. In the left plot for the lower body size, zigzag shapes can be spotted. In the right plot with a larger near-Earth object size, the velocity change per projectile impact gets smaller, why the prominent zigzag smooths out and is only visible in a zoom. Please note, that there is not an order of magnitude difference in size but the diameter is only doubled. Therefore the evolution is very different for sub-100-m objects compared to 1-km-sized bodies.

With the shot frequency  $s$  and the number of projectiles  $i$ , which hit until the time  $t_{\text{def},i}$ , we can subsume

$$t_{\text{def},i} - t_{\text{def},1} = \frac{i-1}{s} \quad (2.25)$$

in Eq.(2.24) to eliminate  $t_{\text{def},i}$ . The boundary condition of a total number of projectiles  $n = 1$  for  $t_{\text{def},i} = t_{\text{def},1}$  is fulfilled.

$$\begin{aligned} \Delta v_r(t) &= \frac{0.035 \frac{\text{m}}{\text{s}}}{-t} - \frac{\Delta v(m_{\text{NEO}})}{t} \sum_{i=1}^n t_{\text{def},i} \\ &= \frac{0.035}{-t \cos(53.4^\circ)} - \frac{\Delta v(m_{\text{NEO}})}{t} \sum_{i=1}^n \left[ \frac{i-1}{s} + t_{\text{def},1} \right] \\ &= \frac{0.035}{-t \cos(53.4^\circ)} - \frac{\Delta v(m_{\text{NEO}})}{t} \left[ nt_{\text{def},1} - \frac{n}{s} + \frac{1}{s} \sum_{i=1}^n i \right] \\ &= \frac{0.035}{-t \cos(53.4^\circ)} - \frac{\Delta v(m_{\text{NEO}})}{t} \left[ n \left( t_{\text{def},1} - \frac{1}{s} \right) + \frac{n^2 + n}{2s} \right] . \end{aligned} \quad (2.26)$$

The sum was solved by a finite series (Bronstein et al., 2012). According to Eq.(2.25),

$$n = s(t_{\text{def},n} - t_{\text{def},1}) + 1 \quad (2.27)$$

is true for  $i = n$  the total number of shots.

Now we can resubstitute  $n$  of Eq.(2.27) in Eq.(2.26) and obtain

$$\Delta v_r(t) = \frac{0.035}{-t \cos(53.4^\circ)} - \frac{\Delta v(m_{\text{NEO}})}{t} \left[ s \left( t - t_{\text{def},1} + \frac{1}{s} \right) \left( t_{\text{def},1} - \frac{1}{s} \right) + \frac{s \left( t - t_{\text{def},1} + \frac{1}{s} \right)^2 + \left( t - t_{\text{def},1} + \frac{1}{s} \right)}{2} \right] . \quad (2.28)$$

The outcome for various configurations are added to Fig.2.8 as dotted gray lines. They perfectly fit to the lower end of the zigzag-shaped stepwise evolution.

We continue to use the smoothed formula, as we want to find the critical values for which we barely succeed in deflecting. The condition for a deflection is given by  $\Delta v_r(t) \leq 0$ , why we get

$$\begin{aligned} 0 &= \frac{0.035}{-t \cos(53.4^\circ)} - \frac{\Delta v(m_{\text{NEO}})}{t} \left[ s \left( t - t_{\text{def},1} + \frac{1}{s} \right) \left( t_{\text{def},1} - \frac{1}{s} \right) + \frac{s \left( t - t_{\text{def},1} + \frac{1}{s} \right)^2 + \left( t - t_{\text{def},1} + \frac{1}{s} \right)}{2} \right] \\ &= - \frac{0.035}{\Delta v(m_{\text{NEO}}) \cos(53.4^\circ)} - \left[ s \left( t - t_{\text{def},1} + \frac{1}{s} \right) \left( t_{\text{def},1} - \frac{1}{s} \right) + \frac{s \left( t - t_{\text{def},1} + \frac{1}{s} \right)^2 + \left( t - t_{\text{def},1} + \frac{1}{s} \right)}{2} \right] . \end{aligned} \quad (2.29)$$

The deflection must also happen before the impact, why the critical value is given at  $t = 0$  yr:

$$\begin{aligned} 0 &= - \frac{0.035}{\Delta v(m_{\text{NEO}}) \cos(53.4^\circ)} - \left[ s \left( -t_{\text{def},1} + \frac{1}{s} \right) \left( t_{\text{def},1} - \frac{1}{s} \right) + \frac{s \left( -t_{\text{def},1} + \frac{1}{s} \right)^2 + \left( -t_{\text{def},1} + \frac{1}{s} \right)}{2} \right] \\ &= t_{\text{def},1}^2 - \frac{1}{s} t_{\text{def},1} - \frac{0.07}{s \Delta v(m_{\text{NEO}}) \cos(53.4^\circ)} \\ t_{\text{def},1} &= \frac{1}{2s} - \sqrt{\frac{1}{4s^2} - \frac{0.07}{s \Delta v(m_{\text{NEO}}) \cos(53.4^\circ)}} . \end{aligned} \quad (2.30)$$

We can plot Eq.(2.30) against the mass of the asteroid to see when the deflection process

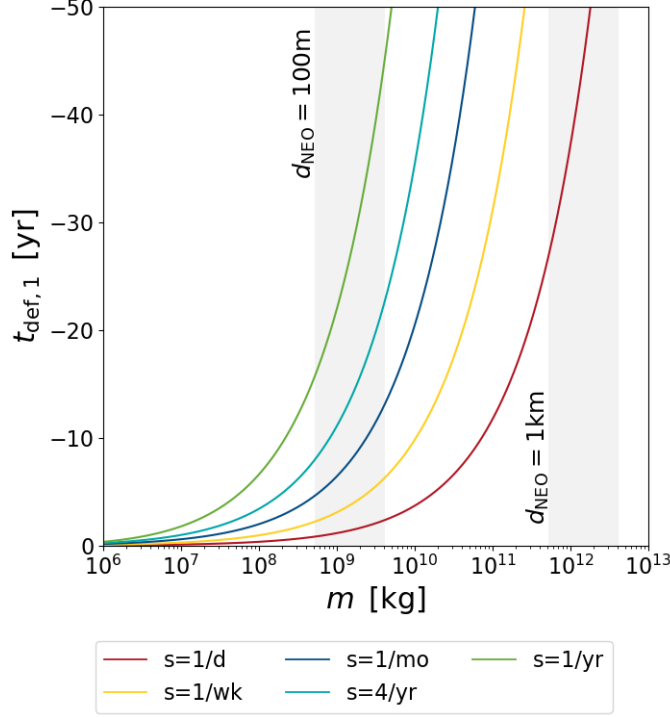


Figure 2.9: The plot shows the deflection starting time  $t_{\text{def},1}$  for continuous deflection, depending on the mass  $m_{\text{NEO}}$  of the object. The various colors represent the different shot frequencies  $s$ . The vertical gray domains show the masses of NEOs with certain diameters and densities ranging from  $1 \frac{\text{kg}}{\text{dm}^3} \leq \rho_{\text{NEO}} \leq 8 \frac{\text{kg}}{\text{dm}^3}$ . For a reasonable timescale of maximum 50 yr, 100-m-sized objects can be handled, but km-sized NEOS can not be deflected. For a weekly shot, a fairly short deflection starting time of a few years is needed for a successful 100 m near-Earth object deflection.

has to start to barely save Earth, done in Fig.2.9. As there is also a dependency of the shot frequency, various curves for different  $s$  are shown. As before, the gray region give the mass range of a 100-m and 1-km object for a broad spectrum of bulk densities.

As expected, a higher shot rate  $s$  leads to a lower deflection starting time  $t_{\text{def},1}$  for NEOs with the same mass. On the other hand, with higher  $s$  and an earlier deflection start, more massive objects can be handled. With  $s = 1/\text{d}$ , km-sized objects get achievable, but one shot per day for at least 30 years means a total shot number of more than  $10^4$ , which seems unrealistic. In contrast, 100-m-sized objects are in the achievable range for a non-instantaneous, but continuous deflection by Breakthrough Starshot projectiles. For a weekly shot, a 100-m NEO can be quite well deflected with a starting time of only a few years. With the same rate but 30 years, a 400-m body is feasible. The number  $n$  of shot

projectiles can be calculated with Eq.(2.27). Since Fig.2.9 depends only on  $s$  and Fig.2.7 depends on  $n$ , they can not be simply compared to each other.

## 2.6 Deflection with maximum projectile number

To compare the single event deflection, described in Sec.2.4, with the continuous deflection we have to choose fixed projectile numbers  $n$  in Eq.2.26. We use the condition  $\Delta v_r = 0 \frac{m}{s}$  to get the deflection starting time  $t_{\text{def},1}$ :

$$\begin{aligned} 0 &= \frac{0.035}{-t \cos(53.4^\circ)} - \frac{\Delta v(m_{\text{NEO}})}{t} \left[ n \left( t_{\text{def},1} - \frac{1}{s} \right) + \frac{n^2 + n}{2s} \right] \\ &= nt_{\text{def},1} - n \frac{1}{s} + n^2 \frac{1}{2s} + n \frac{1}{2s} + \frac{0.035}{\Delta v(m_{\text{NEO}}) \cos(53.4^\circ)} \\ t_{\text{def},1} &= \frac{1}{2s}(1 - n) - \frac{0.035}{n \Delta v(m_{\text{NEO}}) \cos(53.4^\circ)}. \end{aligned} \quad (2.31)$$

A fixed  $n$  for certain fixed shot frequency  $s$  leads to physically reasonable lower limits of  $t_{\text{def},1}$ . For later deflection starting times, where a certain shot number can not be enabled anymore, we use Eq.(2.28) with lower  $n$ . Finally, we get the function, which gives the deflection starting time  $t_{\text{def},1}$  for a maximum number of  $n$  shots:

$$t_{\text{def},1} = \begin{cases} \frac{1}{2s}(1 - n) - \frac{0.035}{n \Delta v(m_{\text{NEO}}) \cos(53.4^\circ)}, & \text{if } 1 \leq \frac{1}{2} + \frac{0.035s}{(n^2 - n) \Delta v \cos(53.4^\circ)} \\ \frac{1}{2s} - \sqrt{\frac{1}{4s^2} - \frac{0.07}{s \Delta v(m_{\text{NEO}}) \cos(53.4^\circ)}}, & \text{otherwise} \end{cases}. \quad (2.32)$$

The function for various  $n$  with different line styles and  $s$  with different colors is shown in Fig.2.10. One can already see, that the km-regime of spherically approximated bodies is not reached, because the maximum shot number is limited to  $10^3$  and a higher number is needed, as discussed in Fig.2.9. The 100-m-sized NEOs are deflectable, yet the deflection starting time extremely depends on the maximum  $n$  and  $s$ . If one follows a single shot rate, all the lines overlap close to 0 years. For earlier deflections, the curve splits into separate branches, which is the result of the projectile limitation. The plot clearly shows, that a successful planetary defense with Breakthrough Starshot is not only based on early deflection, but a large shot rate is needed, resulting into many impacts and momentum transfer.

Now the single event deflection can be compared to the continuous deflection, plotted in Fig.2.11. We see three figures, each for a maximum number of projectile shots  $n$ , where the deflection starting time  $t_{\text{def},1}$  of the first shot is plotted as function of the NEO mass  $m_{\text{NEO}}$ . The various colored lines represent the different shot rates for the continuous deflection, while the black solid line is the associated single event deflection. The horizontal, dotted lines give the time, where the number of  $n$  shots with a shot rate  $s$  can be barely reached, which is why they have the same colors as the corresponding  $s$ . The gray shaded areas give the mass range of a  $d_{\text{NEO}} = 100$  m and  $d_{\text{NEO}} = 1$  km object, depending on the bulk density  $1000 \frac{\text{kg}}{\text{m}^3} \leq \rho_{\text{NEO}} \leq 8000 \frac{\text{kg}}{\text{m}^3}$ .

For all three plots, the single event deflection would be always the most efficient de-

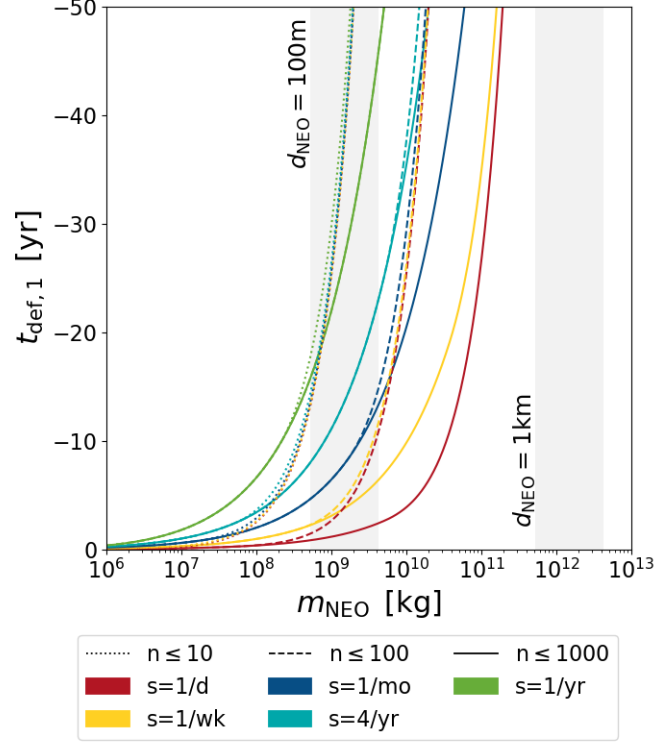


Figure 2.10: The plot shows the deflection starting time  $t_{\text{def},1}$  for a maximum number of projectiles  $n$ , depending on the mass  $m_{\text{NEO}}$  of the object. The various colors represent the different maximum numbers  $n$  of the projectiles. The vertical gray domains show the masses of NEOs with certain diameters and densities ranging from  $1 \frac{\text{kg}}{\text{dm}^3} \leq \rho_{\text{NEO}} \leq 8 \frac{\text{kg}}{\text{dm}^3}$ . For a reasonable timescale of maximum 50 yr, 100-m-sized objects can be handled, but the km-regime can not be deflected. For  $t_{\text{def},1}$  closer to 0 yr, the curves of same  $s$  match and split into branches for earlier deflections.

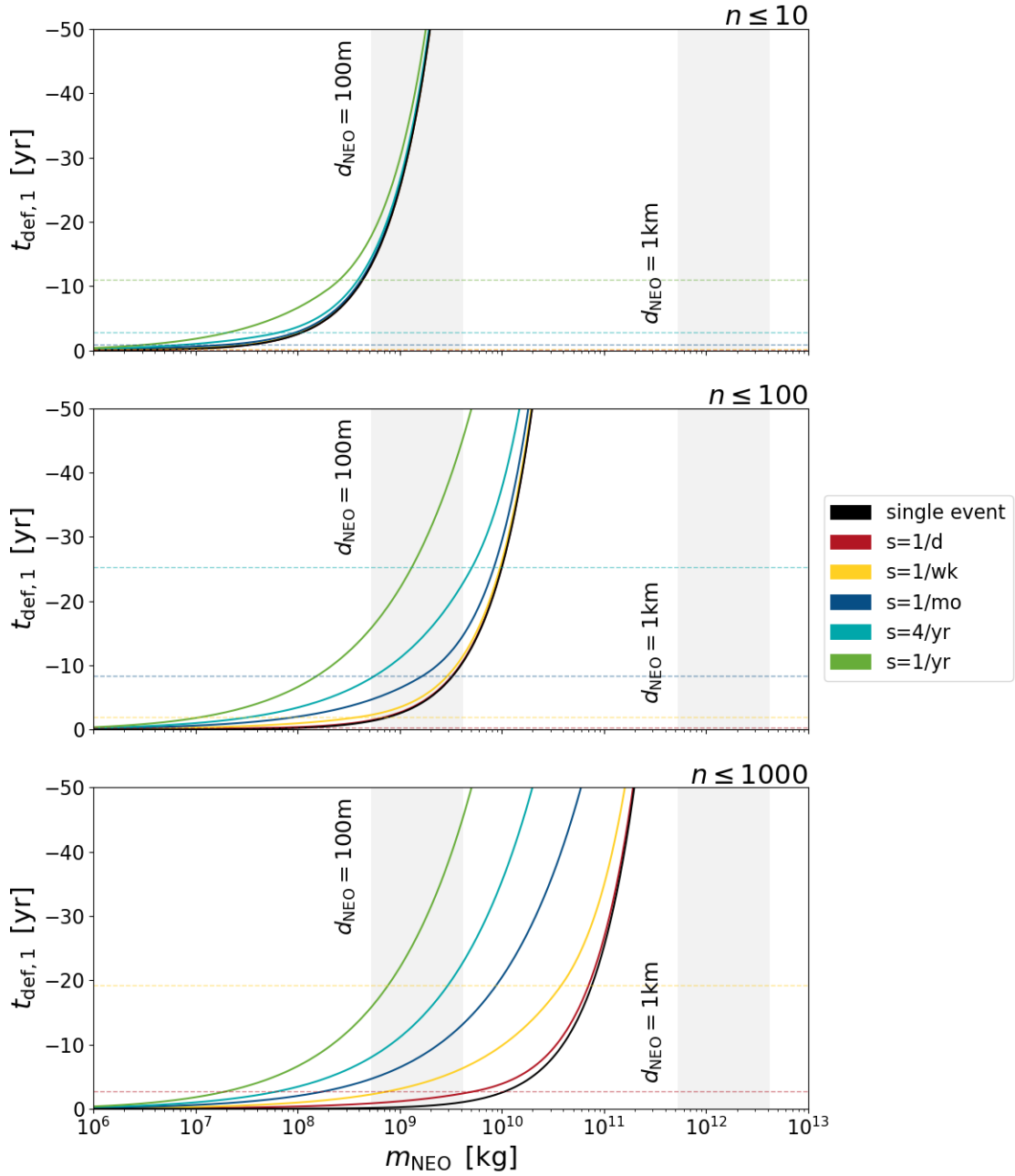


Figure 2.11: The plots show the deflection starting time  $t_{\text{def},1}$  for a maximum number of  $n$  impacting projectiles as a function of the NEO mass  $m_{\text{NEO}}$  and the shot rate  $s$  with various line colors. The solid black line indicates the single event velocity change for the corresponding  $n$ . The horizontal lines give the times, where the  $n$  shots with a certain rate  $s$  are achieved. Below those lines with the corresponding color, the shot number is smaller than the given  $n$ . The gray areas represent the masses of NEOs with certain diameters and densities ranging from  $1 \frac{\text{kg}}{\text{dm}^3} \leq \rho_{\text{NEO}} \leq 8 \frac{\text{kg}}{\text{dm}^3}$ . In general, a higher shot rate moves the curves to the single event model.

flection as its curve is never crossed by the continuous deflections. For  $n \leq 10$ , the colored lines strongly approach the black line at early  $t_{\text{def},1}$ . Hence here is hardly a difference between all the models and the various  $s$ . For deflections around 10 years, the  $s = 1/\text{yr}$  curve differs significantly, while the others are very similar to the single event deflection. The reason for this is the limit of only 10 projectiles, where the deflection process by a high shot frequency is finished in a very short time frame, making those continuous deflections similar to a single event deflection. For lower shot rates, the process is extended and can not be compared to an unique event. This circumstance can be recognized by the horizontal lines too, where the lower shot rates show several years until the 10 projectiles hit. The more frequent rates can be barely seen, as they are very close to zero. With  $n \leq 10$ , stony objects with 100 m can be deflected in a time frame of less than 50 years. Here, planetary defense works also for 50 m stony objects with less than 10 years. For  $n \leq 10$  all curves are close together, while for  $n \leq 1000$  the curves are far apart from each other.

For  $n \leq 100$  and early deflection starting time, the  $s = 1/\text{yr}$  is clearly off the single event model. It is not possible to send all 100 projectiles in the limits of the plot, since 100 years would be needed, why the corresponding horizontal line can not be displayed anymore. For short  $t_{\text{def},1}$ , only the  $s = 1/\text{wk}$  and  $s = 1/\text{d}$  are located close to the black line. For  $s = 1/\text{mo}$  or faster, a 100 m stony object can be handled within 10 years and for 50 years 200 m objects are achievable.

For  $n \leq 1000$  only the  $s = 1/\text{d}$  curve fairly fits the single event model at short deflection starting times. For earlier starts near 50 years, the  $s = 1/\text{wk}$  approaches more or less, too. The full 1000 shots can be reached only with  $s = 1/\text{wk}$  and  $s = 1/\text{d}$  within the shown 50 yr. As one can see, the deflection prospects are highly depended on the shot rate. However, as discussed before, km-sized objects are not deflectable. An even higher shot rate does not solve this problem, since this would only lead to a curve closer to the single event model and the black line would not be crossed for the same  $n$ . Hence, only a larger shot number can push the feasibility limit to bigger near-Earth objects, but as a consequence a higher  $s$  is needed too. Otherwise the deflection would not approach the single event model and therefore lies far off in the left side of the plot, as the other curves already do.

The horizontal lines are a measure of how much the curves approach the single event model in the given limits. In the upper most plot, all horizontal lines are below  $t_{\text{def},1} \approx -12\text{yr}$ , why all shot rates are quite close to the single event model. The other extreme is the lowermost plot, where only the horizontal lines for the most frequent shot rates lie in the limits, the curves are extremely spread and for the given time range mostly far away

from the single event model.

## 2.7 Targeting accuracy and impact probability

The Breakthrough Initiative (2018) aims for shooting a nanocraft to the next planetary system. The goal is to enter the system at a maximum distance of  $r_{\text{PC}} = 1 \text{ AU}$  to its host star. As discussed before, the primary destination will be most likely Proxima Centauri with a distance  $D_{\text{PC}} = 1.295 \text{ pc} \approx 4.224 \text{ ly}$  Anglada-Escudé et al. (2016). With those values, a maximum targeting angle can be determined:

$$\alpha_{\text{tar}} = \arctan\left(\frac{r}{D}\right) . \quad (2.33)$$

Here,  $D$  is in general the distance to an object and  $r$  its radius. We plot the maximum targeting angle together with the required angle for NEOs, or in other words the minimum required targeting accuracy, in the Solar System in Fig.2.12. The green line at  $\alpha_{\text{tar,max}} = 0.77 \text{ arcsec}$  is the obtained value for Proxima Centauri, where we do not take any possibility of course correction into account. So once the projectiles get accelerated, their path can not be actively changed anymore. The other colored lines show the required values for hitting spherically approximated near-Earth objects with a certain size and various distances to Earth. A 10-km-sized NEO at a distance  $D = 0.01 \text{ AU}$ , which is closer than the distance needed for final acceleration, barely has a required targeting angle close to the aimed maximum angle. The smaller the bodies and the further away, the required angles get lower. For 100-m-sized objects, an at least 50 times higher precision would be needed.

As the aimed maximum targeting angle might be difficult to reach, the Breakthrough Initiative could settle for a lower accuracy and maybe accept a loss of projectiles, not entering the Proxima Centauri system. This would lower the efficiency for planetary defense with Breakthrough Starshot, too.

We take the maximum targeting angle and minimum required accuracy as basis and calculate the probability of a projectile impact on a NEO by (Bronstein et al., 2012)

$$P = \frac{n_{\text{pro}}}{n_{\text{all}}} = \frac{A_{\text{NEO}}}{A_{\text{tar,max}}} = \frac{\pi\left(\frac{d_{\text{NEO}}}{2}\right)^2}{\pi(D_{\text{NEO}} \tan(\alpha_{\text{tar,max}}))^2} = \left(\frac{d_{\text{NEO}}}{2r_{\text{PC}}} \frac{D_{\text{PC}}}{D_{\text{NEO}}}\right)^2 , \quad (2.34)$$

where  $n_{\text{pro}}$  is the number of the prosperous events and  $n_{\text{all}}$  the number of all events.  $n_{\text{pro}}$  can be identified in this work with the projectiles hitting the NEO given by the area  $A_{\text{NEO}}$

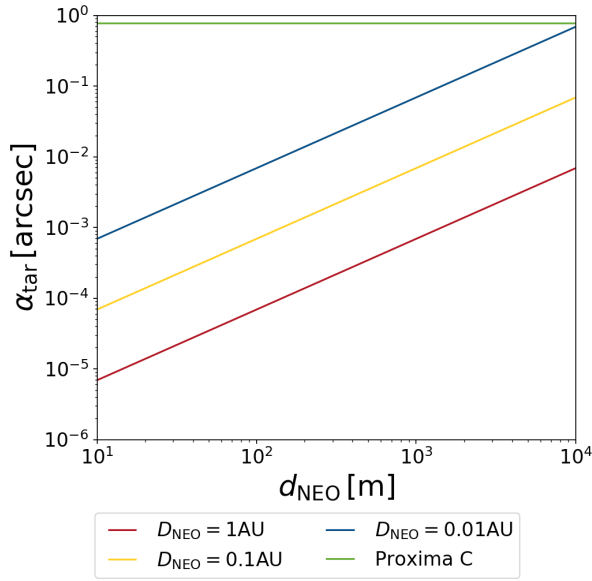


Figure 2.12: The plot shows the required targeting angles of projectiles for impacting on NEOs with certain sizes  $d_{\text{NEO}}$  and distances  $D_{\text{NEO}}$ . The aimed maximum targeting angle for entering Proxima Centauri is marked, too.

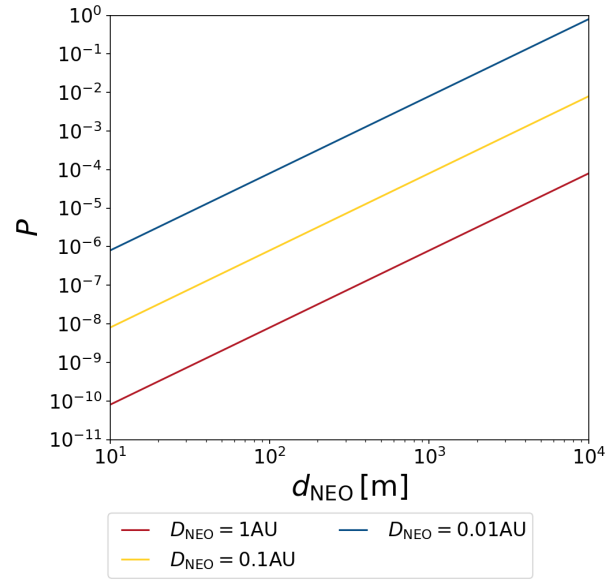


Figure 2.13: The plot shows the impact probability of projectiles on an object for various NEO diameters  $d_{\text{NEO}}$  and distances  $D_{\text{NEO}}$ .

of the body. All events are the randomly shot projectiles penetrating an area  $A_{\text{tar,max}}$  at the distance of the NEO, spanned by the maximum targeting angle  $\alpha_{\text{tar,max}}$ .

Similar as before, we can plot the probability of randomly hitting a near-Earth object as function of the size  $d_{\text{NEO}}$  and distance to Earth  $D_{\text{NEO}}$  in Fig.2.13. Due to the reciprocally squared dependence on the variables, the resulting curves are very steep. For the 100-m-sized objects we get very low probabilities ranging from roughly  $10^{-4} \lesssim P \lesssim 10^{-8}$ .

We can invert this problem and ask, how accurate the Breakthrough Starshot targeting must be to get a projectile impact with a certain probability. For this question we introduce an additional amplification factor of the targeting angle  $\chi$  in Eq.2.34 and get

$$\chi = \sqrt{P} \left( \frac{2r_{\text{PC}} D_{\text{NEO}}}{d_{\text{NEO}} D_{\text{PC}}} \right) \quad (2.35)$$

with the help of the small angle approximation. The resulting  $\chi$  for a 100% impact probability as function of the object size  $d_{\text{NEO}}$  and with various distances  $D_{\text{NEO}}$  is shown in Fig.2.14. As expected, a lower  $\chi$  is needed for larger and closer objects. A 100 m NEO at

1 AU needs roughly an improvement of the factor  $10^4$  for the aimed maximum targeting angle to ensure an impact.

Since the aimed maximum targeting angle for Breakthrough Starshot does not lead to an impact for every shot, we have to shoot a number of projectiles to realize a hit. The probability for a number of impacts  $k$  on a NEO for a specific number of shots  $n$  can be determined with the binomial distribution, as described by (Bronstein et al., 2012):

$$W_P^n(k) = \binom{n}{k} P^k (1 - P)^{n-k} = \frac{n!}{k!(n-k)!} P^k (1 - P)^{n-k} \quad . \quad (2.36)$$

Here,  $P$  is again the probability of an impact on the NEO as given in Eq.(2.34) and  $(1 - P)$  the probability of a miss. Summing up Eq.(2.36) over all  $k$  gives:

$$1 = \sum_{k=0}^n W_P^n(k) = \sum_{k=1}^n W_P^n(k) + (1 - P)^n = W_P^n(k > 0) + (1 - P)^n \quad . \quad (2.37)$$

Now we can determine the required shots  $n$  to hit at least once the NEO with a certain probability  $W_P^n(k > 0)$ :

$$n = \log_{(1-P)}(1 - W_P^n(k > 0)) = \frac{\ln(1 - W_P^n(k > 0))}{\ln(1 - P)} \quad . \quad (2.38)$$

The result of Eq.(2.38) for a 50% chance of at least one impact as function of the near-Earth object size  $d_{\text{NEO}}$  and various distances  $D_{\text{NEO}}$  is shown in Fig.2.15. For 10-km-sized, 0.01 AU distant objects only a few shots are needed. Here, we can see steps, which vanish for higher  $n$ , as the plot has logarithmic axes. As the NEO is located further away, the number of required shots increases significantly and rises several orders of magnitude. Same is true for shrinking the size with a fixed distance. Close 100-m-sized objects already need  $10^4$  shots and 1 AU distant bodies need  $10^9$  attempts to have a 50% chance of at least one impact. This means, only km-sized or larger NEOs which are close to Earth have a realistic chance of being hit with the given aimed targeting precision. However, as discussed before, those massive objects are not deflectable by the Breakthrough Starshot method by pure momentum transfer, since the velocity change is too low. The targeting precision is therefore the bottleneck of this planetary defense strategy and must be improved a lot for the real application.

In contrast to theoretical studies, the position of the NEOs are not perfectly known in reality, which leads to an additional uncertainty. Desmars et al. (2013) process data

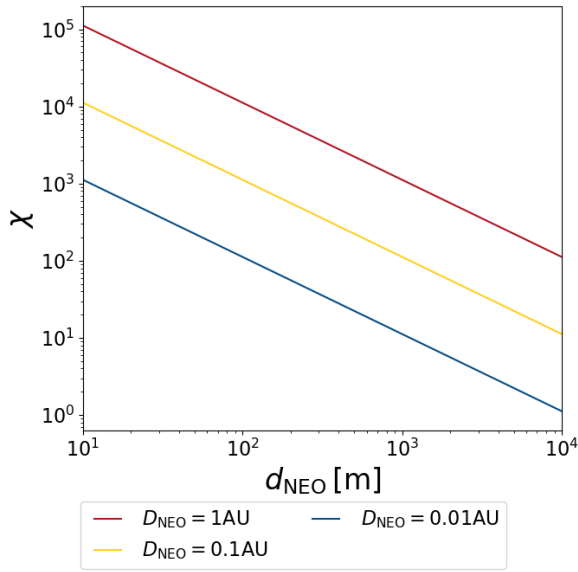


Figure 2.14: The targeting angle amplification factor  $\chi$  for a 100% impact chance is plotted as function of the NEO size  $d_{\text{NEO}}$  and distance  $D_{\text{NEO}}$ .

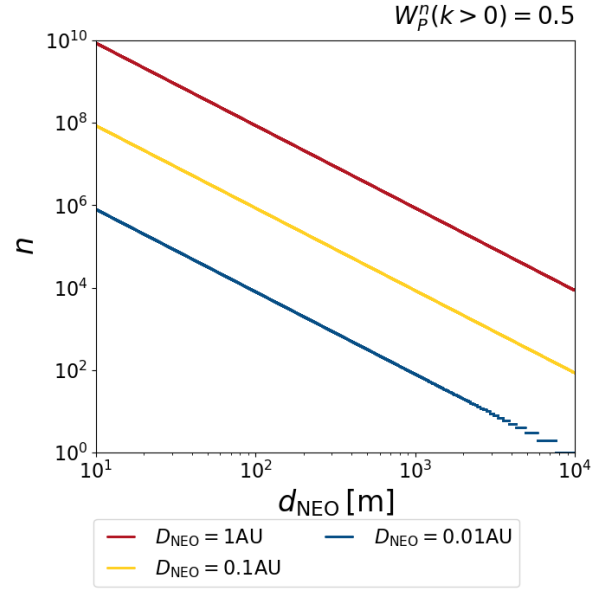


Figure 2.15: The figure shows the probability of hitting a NEO with 50% chance at least once as function of the NEO diameter  $d_{\text{NEO}}$  and distance  $D_{\text{NEO}}$ .

from the AstDyS-2 (2013) database and report accuracies for various observation methods. The ground-based CCD observations, which represent 94.12% of all asteroid observations, have an approximate uncertainty of 0.388 arcsec. The Wide-Field Infrared Survey Explorer (WISE) space telescope, which contributes with 4.25%, has an accuracy of roughly 0.583 arcsec. Radar observations are extremely rare, yet produce the most accurate data with a position uncertainty of about 3.325 km. Ostro and Giorgini (2004) mentions roughly 10 m as the best possible radar resolution.

We can compare those values to the targeting uncertainty for Breakthrough Starshot with  $\alpha_{\text{tar,max}}$ . The resulting spacial uncertainties  $d_{\text{uncert}}$  as function of the distance to the NEO  $D_{\text{NEO}}$  is shown in Fig.2.16. The gray shaded area is the acceleration zone and the gray vertical line indicates the distance of 1 AU. The Breakthrough Starshot uncertainty ranges within the plot limits from  $10^2 \text{ m} \lesssim d_{\text{uncert}} \lesssim 10^6 \text{ m}$ . The best knowledge of the position by radar astronomy is much better than the shot uncertainty and the usual radar accuracy is only worse close to Earth. However, for such close NEOs, better values, which are closer to the best radar observations, might be obtained. The ground-based CCD and the WISE data are both continuously lower than the Breakthrough Starshot uncertainty, yet all of them have the same order of magnitude. Therefore, there could be some outliers of the

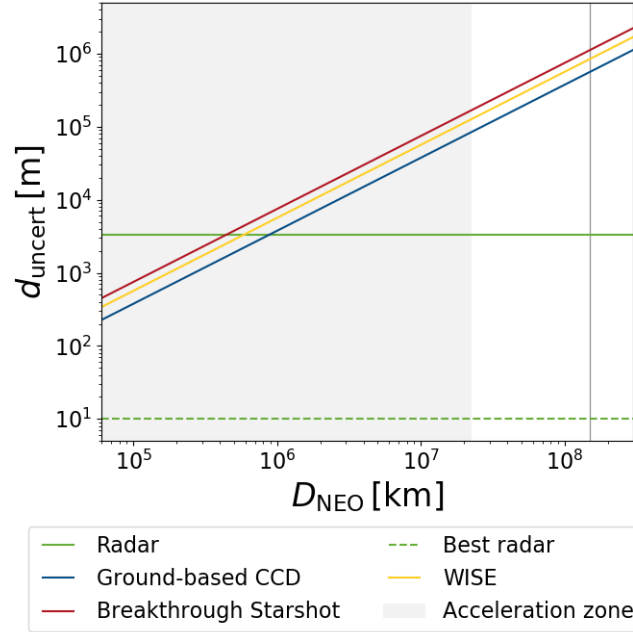


Figure 2.16: The plot shows the spacial uncertainty of the Breakthrough projectiles  $d_{\text{uncert}}$  due to the aimed maximum targeting angle  $\alpha_{\text{tar,max}}$  as red curve. The NEO position accuracy by various observation methods are given, too. The gray area indicates the acceleration zone of the projectiles and the gray vertical line shows the distance of 1 AU. The ground-based CCD and WISE observations, which contribute the most position data, have always an uncertainty lower than the projectiles, but are in the same order of magnitude.

observation, which have a worse accuracy. Though, as most of the data come from CCDs or WISE, the position data are basically of the same accuracy as the targeting accuracy, why those location data can be used for the deflection with Breakthrough Starshot. However, if a better targeting is realized by Breakthrough Starshot, better observations are needed, too. Otherwise, the wrong pointing due to wrong position data might prevent saving Earth.

## 2.8 Course correction of projectiles

So far, we did not take an active steering of the projectiles into account, yet the Breakthrough Initiative (2018) mentions photon thrusters on the StarChips. We assume four photon thruster, as introduced by Lubin (2016) with  $F_{\text{p,photon}} = 33 \text{ pN}$  each, which should be used for attitude control. However, those thrusters might also be used to correct the path of the projectiles. The thrusters should not primarily decrease the velocity of the

projectile, but change its path, why the force should be exceeded perpendicular to the direction of motion. In reality, this could be difficult to realize, since the orientation of the photon thrusters might be in direction of motion and not necessarily perpendicular, yet for a first estimate we ignore this issue.

In the following, we assume perfect location data, but only the targeting uncertainty prevents the projectiles from directly hitting the NEO. We expect the worst possible path with an arbitrary angle divergence to the NEO  $\alpha_{\text{tar}}$ . In addition, a constant force is treated, which is for simplification reasons always perpendicular to the initial path. By trigonometric considerations and the help of Fig.2.17, we can derive a formula for the normalized targeting angle improvement

$$\frac{\varphi}{\alpha_{\text{tar}}} = \frac{1}{\alpha_{\text{tar}}} \arcsin \left[ \frac{\sqrt{(L_y^2 + L_{x,1}^2)}}{\sqrt{(\frac{D_{\text{NEO}}}{\cos \alpha_{\text{tar}}})^2 + L_y^2}} \sin \left[ \arctan \left( \frac{L_y}{L_{x,1}} \right) \right] \right] , \quad (2.39)$$

with

$$L_{x,1} = \frac{D_{\text{NEO}}}{\cos \alpha_{\text{tar}}} - L_{x,0} \quad (2.40)$$

and

$$L_y = \frac{1}{2} \frac{F}{m_p} \left( \frac{L_{x,1}}{v_p} \right)^2 . \quad (2.41)$$

$L_{x,0}$  is the traveled distance with inactive thrusters and on the contrary  $L_{x,1}$  is the traveled distance with active thrusters.  $L_y$  is the result of the perpendicular added force, leading to the targeting angle improvement  $\varphi$ . Eq.(2.41) is a non-relativistic formula and must be

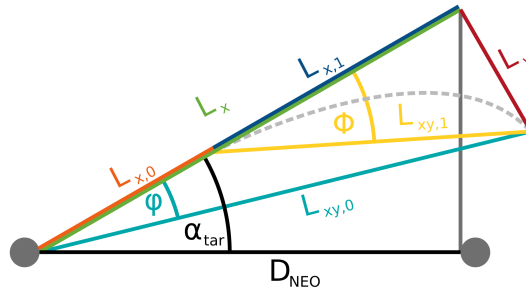


Figure 2.17: The sketch shows the angles and distances needed for the calculation of the targeting angle improvement  $\varphi$ .

treated with caution for  $v_p = 0.2c$ . We ran simulations of the projectile position, computed with the proper acceleration, and noticed that no complicated relativistic formula is needed in this case, but the classical equation is perfectly appropriate for the exerted tiny force  $F = 4F_{p,\text{photon}}$ . Even forces that are several orders larger do not show a difference. Please note, that the acceleration zone is not considered and we use a constant  $v_p$  in this first estimate. Hence, Eq.(2.39) is only a function of the exerted force  $F$ , the distance to the NEO  $D_{\text{NEO}}$ , the place where the acceleration is initiated  $L_{x,0}$  and  $\alpha_{\text{tar}}$ .

The normalized targeting angle improvement with the aimed maximum targeting angle  $\alpha_{\text{tar,max}}$  as function of the NEO distance is plotted in Fig.2.18. The distance of 1 AU is indicated by the vertical gray line. Here, we use the forces  $F = 4F_{p,\text{photon}}$  and  $F = 4F_{p,\text{photon}} \times 10^3$ . In addition, we start the acceleration at different locations, which are set to 0%, 25%, 50% and 75% of  $D_{\text{NEO}}$ . For the four 33 pN photon thrusters, the angle improvement is roughly ranging between  $10^{-12} \lesssim \varphi/\alpha_{\text{tar,max}} \lesssim 10^{-7}$  for the plotted limits, which can be absolutely neglected. Even an increase by a factor of  $10^3$  would only lead to a

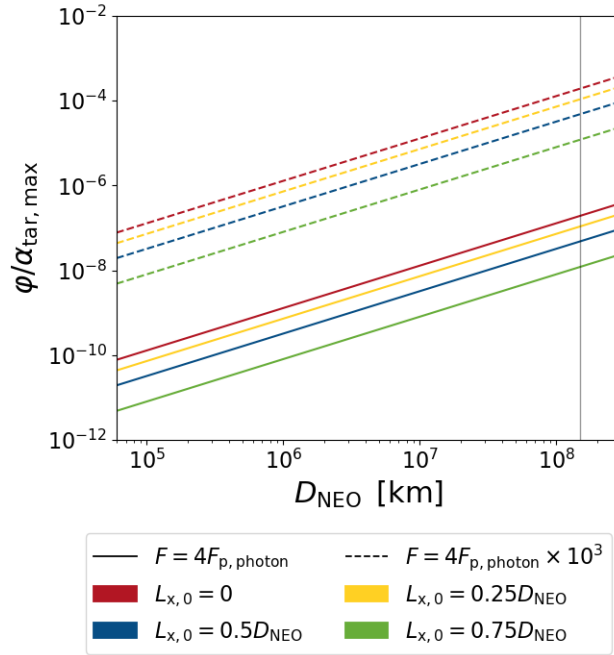


Figure 2.18: The plot shows the normalized targeting angle improvement  $\varphi/\alpha_{\text{tar,max}}$  as function of the NEO distance  $D_{\text{NEO}}$ , two different constant forces  $F$  and various positions where the acceleration starts  $L_{x,0}$ . The vertical gray line shows the distance of 1 AU. Even 1,000 times stronger thrusters as suggested only lead to 0.02% targeting angle improvement, why the thrusters can be neglected for achieving higher impact probability.

maximum improvement of about 0.02% for a NEO at 1 AU and an acceleration start right at the beginning. This shows, that a course correction, to increase the impact probability, is very difficult and with the addressed forces irrelevant.

Please note, one curve does not simply show the evolution by a single projectile due to increasing traveled distance, because we do not use fixed values for  $L_{x,0}$ . They depend on the distance of the near-Earth object itself, why every  $D_{\text{NEO}}$  has an individual  $L_{x,0}$ .

## 2.9 Gravitational perturbation of projectiles

As the projectiles are accelerated by the light beamers they do not move in a straight line through the Solar System but are perturbed by the planets, the Moon and Sun's gravity. The perturbations strongly depend on the current constellation of those celestial bodies and therefore on the epoch. The Sun in the center of the Solar System and Earth as starting point of the projectiles are excluded from this variability. Therefore, for the following computation, only the Sun's and Earth's gravity are considered as perturbation source, yet an exact calculation for a certain epoch has to include other planets and the Moon, too. The data was derived by the simulation code, described in App.A.

The distance between an unperturbed, in a straight line moving projectile and the perturbed, in a curved path moving projectile at a certain position in the ecliptic, seen from the unperturbed projectile, is plotted in the following figures. The colors represent the spacial difference between the projectiles and the solid black lines indicate the different orders of magnitude. The black dot at  $X = 0 \text{ AU}$ ,  $Y = 0 \text{ AU}$  shows the position of the Sun and the black dot at  $X = 1 \text{ AU}$ ,  $Y = 0 \text{ AU}$  shows the position of Earth. The three inner dotted lines roughly visualize the orbit of Venus, Earth and Mars, while the two outer dotted lines roughly limit the asteroid main belt. The computation was done in a moving frame around Sun, keeping Earth at a fixed point.

Fig.2.19 shows the projectiles, starting at 0.15 AU, where they already reached their final speed of  $0.2c$ . During the acceleration process, no perturbation was considered, but only after free floating through space. The white circle represents the acceleration zone. For the left plot only the Sun was taken into account. For the right figure, Earth's gravity was added, too. Visually, no difference between both can be seen, since the starting point of 0.15 AU is way outside of the Earth's sphere of influence with  $D_{\text{SOI}} = 6.2^{-3} \text{ AU}$  (Walter, 2012) and hence Earth's gravity is negligibly small. The perturbations by the Sun already lead in a very narrow area at roughly  $D \approx 0.3 \text{ AU}$  around the Earth to a difference

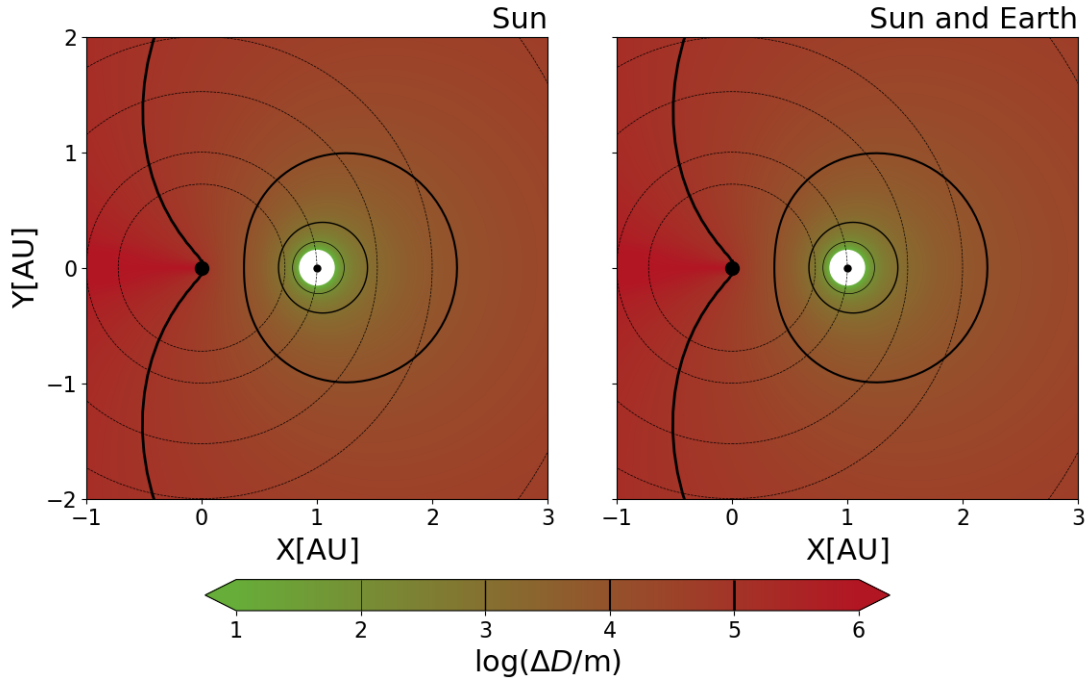


Figure 2.19: The plots show the spatial displacement of gravitationally perturbed projectiles to unperturbed ideal projectiles, depending on the position in the Solar System. The first scenario treats only the gravity of the Sun at  $X = 0$  AU,  $Y = 0$  AU, while the second includes Earth's gravity at  $X = 1$  AU,  $Y = 0$  AU, too. In this model the gravitational perturbation starts when the projectiles reached maximum speed at 0.15 AU, why the region close to Earth is kept blank. The color code displays the perturbation, supported by some thick lines. The dotted concentric lines around the Sun show the orbits of several planets and the edges of the asteroid main belt.

of  $\Delta D = 1$  km. For more than  $D \gtrsim 1$  AU, the perturbation grows to  $\Delta D \gtrsim 10$  km. Until the Sun is reached, the contour lines are roughly circular shaped.

Fig.2.20 takes the acceleration process into account. The projectiles start at  $D = 60 \times 10^3$  km with no relative speed to Earth and are accelerated to the 20% speed of light. In this simulation, the acceleration is considered for simplification reasons to be constant, which is certainly not the realistic case, as described by Parkin (2018). On the one hand, the projectiles start inside the SOI and on the other hand, the projectile velocity is in the beginning low. The projectiles are more perturbed as in the model before and the contour lines look different. If only the Sun is considered, the perturbation for the  $Y \approx 0$  AU values are of the same order as before, yet for all other directions the distraction gets stronger, forming slimmer, egg-shaped contour lines until getting close to the Sun. If Earth is taken into account too, the difference gets bigger, which can be clearly noticed on the right

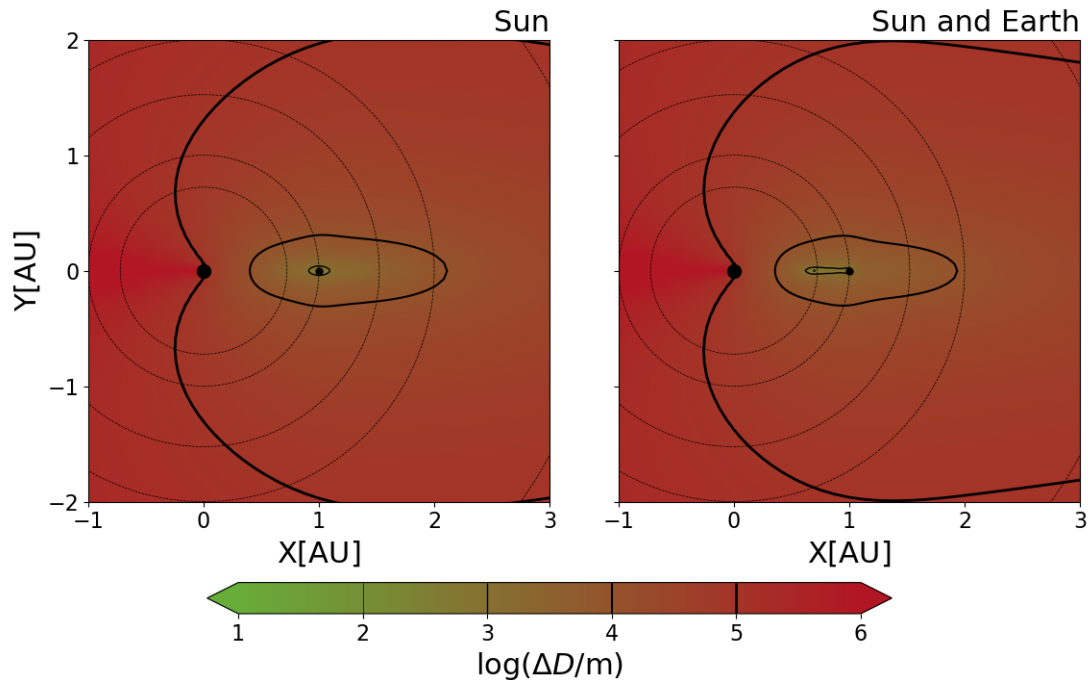


Figure 2.20: The plots show the spacial displacement of gravitationally perturbed projectiles to unperturbed ideal projectiles, depending on the position in the Solar System. The first scenario treats only the gravity of the Sun at  $X = 0$  AU,  $Y = 0$  AU, while the second includes Earth's gravity at  $X = 1$  AU,  $Y = 0$  AU, too. In this model the gravitational perturbation starts when the projectiles start to get accelerated at  $60 \times 10^3$  km. The color code displays the perturbation, supported by some thick lines. The dotted concentric lines around the Sun show the orbits of several planets and the edges of the asteroid main belt.

corners. The differences away from the Sun get stronger, while to the Sun the differences stay roughly constant. Since the Sun's gravity is dominating the area closer to the Sun, Earth's gravity mostly gets negligible. However, there is a small corridor, where the Sun's and Earth's gravity cancel out, leading to a very low distraction, which can be seen as greenish stripe in direction to the Sun. A more detailed look reveals a minimum inside the stripe, as the projectiles, slowed down by Earth at first, catch up to unperturbed projectiles due to the Sun's gravitationally acceleration.

If we compare the distraction values to the interesting sizes of a near-Earth object, ranging from sub-100-m to several km, we see a displacement ranging from the size order of a near-Earth object up to a three larger orders of magnitude. Although the projectiles travel with a fraction of the speed of light, the Sun's gravity must be taken into account, as otherwise the projectiles would clearly miss the NEOs.

## 2.10 Deflection in acceleration zone

As discussed before, the chance of hitting a NEO with the aimed targeting precision is very low. Yet, for close approaches on Earth, the chance of a hit rises. The drawback here is that the NEO will be in the acceleration zone and the final speed will not be achieved. As a result, the velocity change would be lower.

As discussed by Parkin (2018), the acceleration of the projectile changes over time, as it departs from Earth. In the following, we use two different models. For the first, the acceleration decreases reciprocally squared with the distance, since the illumination of the light sail has to evolve with the same dependence, too. The second goes inversely proportional. For both, the relativistic calculation must be considered, as also done by Parkin (2018). Therefore, we have for the reciprocally squared acceleration

$$\dot{v}_2(D) = \gamma(v)^3 \frac{D_{p,ini}^2}{D^2} \dot{v}_{2,ini} = \left( \frac{1}{1 - \frac{v^2}{c^2}} \right)^{\frac{3}{2}} \frac{D_{p,ini}^2}{D^2} \dot{v}_{2,ini} \quad (2.42)$$

and for the inversely proportional one

$$\dot{v}_1(D) = \gamma(v)^3 \frac{D_{p,ini}^2}{D} \dot{v}_{1,ini} = \left( \frac{1}{1 - \frac{v^2}{c^2}} \right)^{\frac{3}{2}} \frac{D_{p,ini}^2}{D} \dot{v}_{1,ini} \quad (2.43)$$

Here, the values of  $\dot{v}_{1/2,ini}$  are the initial accelerations at an initial distance  $D_{p,ini} = 60 \times 10^3$  km, where the projectile moves with an initial velocity  $v_{p,ini} = 0 \frac{m}{s}$ . As the projectile moves to infinity, the acceleration gets  $\lim_{D \rightarrow \infty} \dot{v}_{1/2} = 0 \frac{m}{s^2}$ .

The velocities for the two models can now be calculated by the differential equations

$$\begin{aligned} \dot{v}_2 &= \frac{dv}{dt} = \frac{dv}{dD} \frac{dD}{dt} = v \frac{dv}{dD} \\ D_{p,ini}^2 \dot{v}_{2,ini} \int_{D_{p,ini}}^{D_{NEO}} \frac{1}{D^2} dD &= \int_{v_{2,ini}}^{v_{2,imp}} \left( 1 - \frac{v^2}{c^2} \right)^{\frac{3}{2}} v dv \\ -D_{p,ini}^2 \dot{v}_{2,ini} \frac{1}{D} \Big|_{D_{p,ini}}^{D_{NEO}} &= -\frac{c^2}{5} \left( 1 - \frac{v^2}{c^2} \right)^{\frac{5}{2}} \Big|_{v_{p,ini}}^{v_{2,imp}} \\ v_{2,imp} &= c \sqrt{1 - \left[ 1 - \frac{5D_{p,ini}^2 \dot{v}_{2,ini}}{c^2} \left( \frac{1}{D_{p,ini}} - \frac{1}{D_{NEO}} \right) \right]^{\frac{2}{5}}} \end{aligned} \quad (2.44)$$

and

$$\begin{aligned}
D_{p,\text{ini}}^2 \dot{v}_{1,\text{ini}} \int_{D_{p,\text{ini}}}^{D_{\text{NEO}}} \frac{1}{D} dD &= \int_{v_{1,\text{ini}}}^{v_{1,\text{imp}}} \left(1 - \frac{v^2}{c^2}\right)^{\frac{3}{2}} v dv \\
D_{p,\text{ini}}^2 \dot{v}_{1,\text{ini}} \ln(D) \Big|_{D_{p,\text{ini}}}^{D_{\text{NEO}}} &= -\frac{c^2}{5} \left(1 - \frac{v^2}{c^2}\right)^{\frac{5}{2}} \Big|_{v_{p,\text{ini}}}^{v_{1,\text{imp}}} \\
v_{1,\text{imp}} &= c \sqrt{1 - \left[1 - \frac{5D_{p,\text{ini}}^2 \dot{v}_{1,\text{ini}}}{c^2} \ln\left(\frac{D_{\text{NEO}}}{D_{p,\text{ini}}}\right)\right]^{\frac{2}{5}}} .
\end{aligned} \tag{2.45}$$

As the projectiles should have a final speed  $v_p = 0.2c$  at  $D_{p,\text{full}} = 0.15 \text{ AU}$ , the initial acceleration can be determined to:

$$\begin{aligned}
\dot{v}_{2,\text{ini}} &= \frac{-\frac{c^2}{5} \left[\left(1 - \frac{v_p^2}{c^2}\right)^{\frac{5}{2}} - 1\right]}{D_{p,\text{ini}}^2 \left(\frac{1}{D_{p,\text{ini}}} - \frac{1}{D_{p,\text{full}}}\right)} \approx 2.97 \times 10^6 g_{\oplus} , \\
\dot{v}_{1,\text{ini}} &= \frac{-\frac{c^2}{5} \left[\left(1 - \frac{v_p^2}{c^2}\right)^{\frac{5}{2}} - 1\right]}{D_{p,\text{ini}}^2 \ln\left(\frac{D_{p,\text{full}}}{D_{p,\text{ini}}}\right)} \approx 8.34 \times 10^{-3} g_{\oplus} .
\end{aligned} \tag{2.46}$$

Here,  $g_{\oplus}$  is the standard acceleration due to gravity by Earth. Please note that Parkin (2018) presents a  $\dot{v}_{\text{ini}} = 1.520 \times 10^4 g_{\oplus}$  and a  $\dot{v}_{\text{full}}$  in his publication, which differ from our work, since our models are different and simpler. As one can notice, the  $\dot{v}_{\text{ini}}$  value lies in between of our values, hence we expect the real acceleration somewhere between our models.

In the following plots, four different quantities can be seen. The achieved velocity change for a single impact from Eq.(2.14) as function of the distance is shown in green color, where the two different models span an area. The probability of an impact on a spherically body from Eq.(2.34) is plotted in blue, where we have to use the distance to the NEO  $D_{\text{NEO}} - D_{p,\text{ini}}$ , since the object is coming close to Earth in this calculation and the initial distance can not be neglected. The velocity of the projectiles  $v_{\text{imp}}$  are the cyan areas, deepening on the chosen model. Finally, the combination  $\Delta v \cdot P$  is plotted in red color, indicating the expected value of the velocity change. The horizontal, black lines show the required velocity change by Eq.(2.10) for various deflection starting times. They are not valid for close encounters, or in other words in side the SOI, why we do not give

any statement about the required velocity change inside the SOI. As studied before, large NEOs are much harder to deflect, why only a  $d_{\text{NEO}} = 50$  m in Fig.2.21 and  $d_{\text{NEO}} = 100$  m in Fig.2.22 with both  $\rho_{\text{NEO}} = 2700 \frac{\text{kg}}{\text{m}^3}$  are considered. The left plot shows the full acceleration zone from  $60 \times 10^3 \text{ km} \leq D_{\text{NEO}} \leq 0.15 \text{ AU}$ , while the right one is a zoom to spot details. Here, one can see an additional horizontal dotted line, which indicates the position of the maximum of  $\Delta v \cdot P$ .

For both plots, the reciprocal squared acceleration change leads to the upper limits of  $v_{\text{imp}}$ ,  $\Delta v$  and  $\Delta v \cdot P$ , since the starting acceleration value is much higher than for the other model. However, the final values are reached very quickly and are not changing a

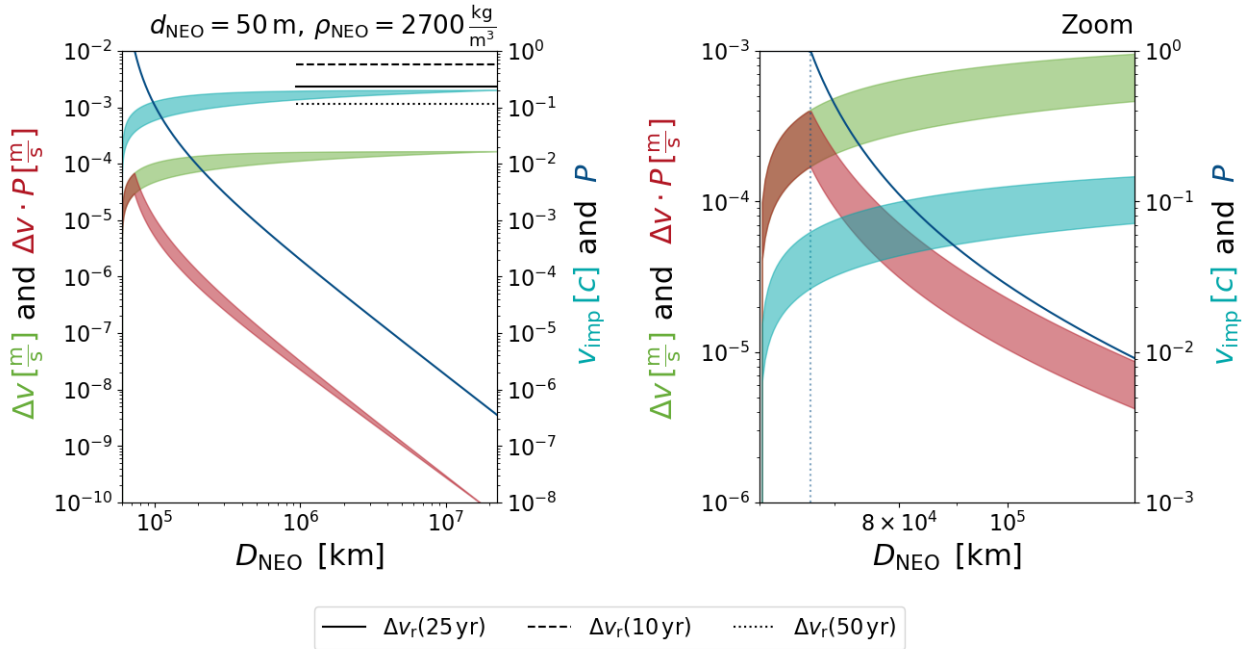


Figure 2.21: The plot shows in cyan the velocity of the projectile  $v_{\text{imp}}$ , in green the achieved velocity change  $\Delta v$ , in blue the probability of an impact  $P$  and in red the expected value of the velocity change  $\Delta v \cdot P$  for a NEO with size  $d_{\text{NEO}} = 50$  m and bulk density of  $\rho_{\text{NEO}} = 2.7 \frac{\text{kg}}{\text{dm}^3}$ . Two different models for the acceleration lead to a range of values and colored areas. We expect the real acceleration in between the two models. All quantities depend on the distance  $D_{\text{NEO}}$  to the NEO. The required velocity change  $\Delta v_r$  for various deflection times are indicated has horizontal lines until the sphere of influence is reached and the correctness of the values can not be guaranteed anymore. The vertical dotted line shows the position of the maximum of  $\Delta v \cdot p$ . The right plot is a zoom into the important part of the left plot. The expected value of the velocity change is mostly dominated by the probability, leading to a maximum between  $2 \times 10^{-4} \frac{\text{m}}{\text{s}} \lesssim \Delta v \cdot P \lesssim 4 \times 10^{-4} \frac{\text{m}}{\text{s}}$ , slightly below  $7 \times 10^4$  km.

lot at the end of the acceleration zone. The inversely proportional model gives the lower limit, as it starts with a lower initial acceleration but is not settling as fast, but catching up slowly. As expected, the achieved  $\Delta v$  for the  $D_{\text{NEO}} = 100$  m object is lower than for the  $D_{\text{NEO}} = 50$  m. The probability starts with a maximum of  $P = 1$  for both objects, yet decreases very quickly as soon as the distance rises. The expected value of the velocity change is not a physically reasonable quantity for a single projectile, yet the position of its maximum shows the distance of the highest velocity change chance. Since the velocities are rising very quickly and are already larger than  $0.01c$  at the maxima of  $\Delta v \cdot P$ , both bodies are mostly dominated by the quickly decreasing probability. The maxima of the

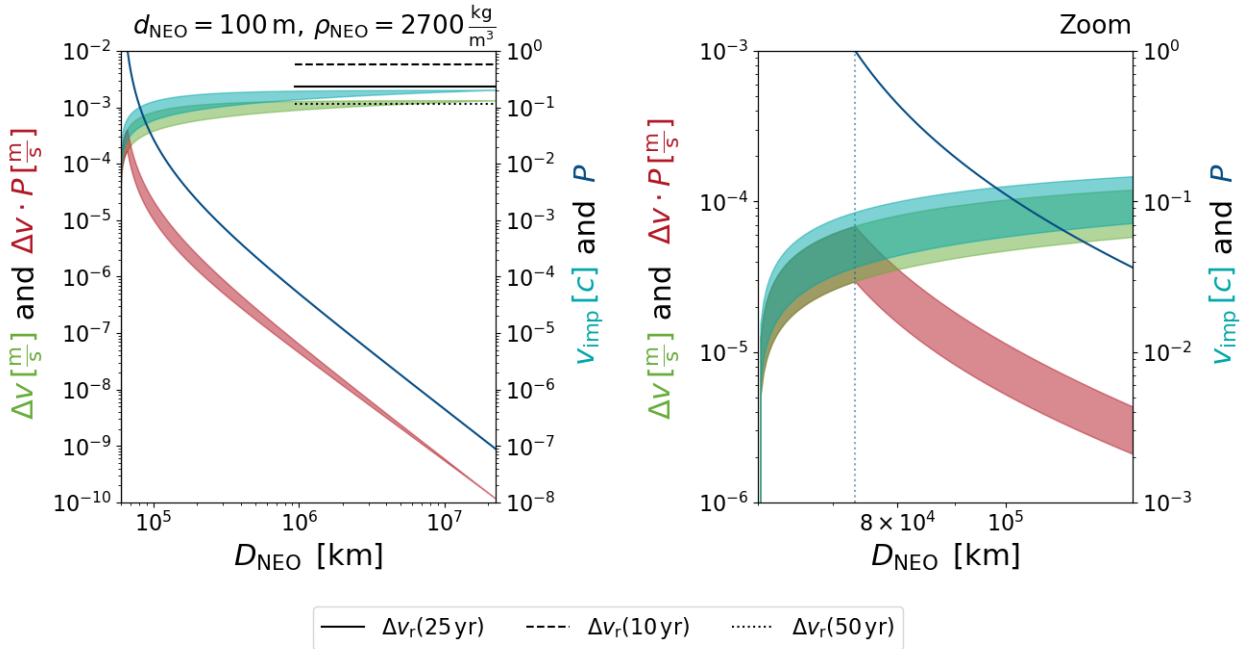


Figure 2.22: The plot shows in cyan the velocity of the projectile  $v_{\text{imp}}$ , in green the achieved velocity change  $\Delta v$ , in blue the probability of an impact  $P$  and in red the expected value of the velocity change  $\Delta v \cdot P$  for a NEO with size  $d_{\text{NEO}} = 100$  m and bulk density of  $\rho_{\text{NEO}} = 2.7 \frac{\text{kg}}{\text{dm}^3}$ . Two different models for the acceleration lead to a range of values and colored areas. We expect the real acceleration in between the two models. All quantities depend on the distance  $D_{\text{NEO}}$  to the NEO. The required velocity change  $\Delta v_r$  for various deflection times are indicated as horizontal lines until the sphere of influence is reached and the correctness of the values can not be guaranteed anymore. The vertical dotted line shows the position of the maximum of  $\Delta v \cdot P$ . The right plot is a zoom into the important part of the left plot. The expected value of the velocity change is mostly dominated by the probability, leading to a maximum between  $3 \times 10^{-5} \frac{\text{m}}{\text{s}} \lesssim \Delta v \cdot P \lesssim 7 \times 10^{-5} \frac{\text{m}}{\text{s}}$ , slightly above  $7 \times 10^4$  km.

expected values are right at the position when  $P$  starts to decrease, which are close to the initial distance, both around  $7 \times 10^4$  km. This is only about 0.3% of the full acceleration length. The highest achievable  $\Delta v \cdot P$  are in the range of a few  $10^{-5} \frac{\text{m}}{\text{s}}$  for the 100-m near-Earth object or a few  $10^{-4} \frac{\text{m}}{\text{s}}$  for the 50-m body. This is less than the required  $\Delta v_r(50 \text{ yr})$ . However, as mentioned in Sec.1.1 and Sec.2.3, close encounters with planets can change the orbit of any small object. A position change of a NEO, induced by a velocity change before the encounter, gets amplified. Carusi et al. (2002) calculates this effect for a few examples by finding several orders lower required  $\Delta v_r$  before the close encounters than after the encounters. Since our deflection happens during the encounter, the needed value might lie somewhere in between, depending on the MOID and when the deflection happens. It is not unlikely that NEAs have close encounters with Earth before their impact on Earth, where keyholes play a major role. The so-called *keyholes* are regions in space with a certain MOID where the orbit of the NEO is changed to a period of an integer resonance with Earth, why it will impact years later. Hence, if a few projectiles can be shot before and shortly after passing a keyhole, Breakthrough Starshot might deflect a NEA during the close encounter Yeomans et al. (2009). Here, more work is certainly needed to investigate those cases in more detail.

## 2.11 Energy release and cratering by projectiles

Besides the linear momentum, the energy is a conserved quantity for a closed system, as described by the first law of thermodynamics in Nolting (2017). For relativistic velocities with relativistic kinetic energies we have

$$m_{\text{NEO}}c^2(\gamma(v_{\text{NEO}}) - 1) + m_{\text{p}}c^2(\gamma(v_{\text{p}}) - 1) = (m_{\text{NEO}} + m_{\text{p}})c^2(\gamma(\Delta v) - 1) + \Delta U = \text{const.} \quad (2.47)$$

with the factor  $\gamma(v) = 1/\sqrt{1 - v^2/c^2}$ ,  $c$  as the speed of light in free space and  $\Delta U$  the change of internal energy. In the frame of reference of the NEO, with  $v_{\text{NEO}} = 0 \frac{\text{km}}{\text{s}}$ ,  $v_{\text{p}} - v_{\text{NEO}} \approx v_{\text{NEO}}$  due to  $c > v_{\text{p}} \gg v_{\text{NEO}}$  and since  $v_{\text{p}} \gg v_{\text{ki}} \gg \Delta v(m_{\text{p}})$ , in the mass range from  $1 \times 10^6$  kg and higher, the change of inner energy for a projectile impact can be written as

$$\Delta U = m_{\text{p}}c^2(\gamma(v_{\text{p}}) - 1) \approx 7 \times 10^{12} \text{ J} \quad (2.48)$$

and the inner energy for a conventional kinetic impactor deflection is given by

$$\Delta U = \frac{1}{2} m_{\text{ki}} v_{\text{ki}}^2 \approx 5 \times 10^{10} \text{ J} \quad . \quad (2.49)$$

Here we used the characteristic values from Tab.2.1 and Tab.2.2 for the Breakthrough Starshot deflection and  $v_{\text{ki}} = 10 \frac{\text{km}}{\text{s}}$  and  $m_{\text{ki}} = 1 \text{ t}$  for the conventional kinetic impactor. We see that a projectile releases roughly 140 times more energy as the kinetic impactor.

The released energy leads to rearranging of the internal structure, heating, sublimation and material ejection of the NEO. To get an impression of what might happen at the NEO during a projectile impact, we take a look on crater scaling laws by Holsapple (1993). In the following we stick to the summary by (Richardson et al., 2007), where more details about the equations and their derivations can be looked up.

The transient crater volume for a spherically impacting body is given by:

$$V_{\text{crater}} = K_1 \left( \frac{m_{\text{p}}}{\rho_{\text{NEO}}} \right) \left[ \left( \frac{g_{\text{NEO}} r_{\text{p}}}{v_{\text{p}}^2} \right) \left( \frac{\rho_{\text{NEO}}}{\rho_{\text{p}}} \right)^{-\frac{1}{3}} + \left( \frac{\bar{Y}}{\rho_{\text{NEO}} v_{\text{p}}^2} \right)^{\frac{2+\mu}{2}} \right]^{-\frac{3\mu}{2+\mu}} \quad . \quad (2.50)$$

It is not explicitly mentioned in the work of Holsapple (1993) or Richardson et al. (2007) that the impact site has originally a roughly flat surface, or in other words the target is much bigger than the impactor. However, this is indicated by all sketches.  $\bar{Y}$  is the effective material strength, depending on the target material.  $K_1$  and  $\mu$  are additional properties of the target material. Depending on the main driver of the cratering process  $\mu$  ranges from  $\frac{1}{3} \leq \mu \leq \frac{2}{3}$ . Those values are derived experimentally, with hypervelocity experiments for various materials, as given in Tab.2.4. Unfortunately, those experimental impact velocities are orders lower than  $0.2c$ , as shown by Housen and Holsapple (2011). Even though we can not argue that those values can be used for the computation of a Breakthrough Startshot projectile impact, we are going to use them, since otherwise there is no way of estimating the effects of an impact. Therefore we want to point out that the results, obtained by using those constants, should be treated with caution.

In addition, Eq.(2.50) contains the bulk density of the target  $\rho_{\text{NEO}}$ , mass  $m_{\text{p}}$ , velocity  $v_{\text{p}}$  and bulk density  $\rho_{\text{p}}$  of the projectile.  $r_{\text{p}}$  is the radius of the spherical projectile, which is very unfavorable, since the Breakthrough Starshot projectile is not spherical but very flat. For reshaping the projectiles, as given in Tab.2.1, we have two different options. We keep the mass and bulk density fixed, while determining a new, smaller radius  $r_{\text{p,sph}} = 6.80 \times 10^{-3} \text{ m}$ , or we keep the mass and radius and determine a new, lower bulk density

$\rho_{\text{p,sph}} = 9.80 \times 10^{-5} \frac{\text{kg}}{\text{m}^3}$ . Both values are far off the real values of the projectile. Finally,  $g_{\text{NEO}}$  is the force of gravity of a NEO, which can be computed for the case of a sphere by

$$g_{\text{NEO}} = G \frac{m_{\text{NEO}}}{r_{\text{NEO}}^2} = G \frac{2\pi}{3} \rho_{\text{NEO}} d_{\text{NEO}} \quad . \quad (2.51)$$

Eq.(2.50) can be divided into two regimes. If  $g \gg \bar{Y}$ , much more energy is needed to eject the crater material than breaking up the near-Earth asteroid material. This is the gravity regime or gravity-dominated cratering, where Eq.(2.50) can be simplified to

$$V_{\text{crater,g}} = K_1 \left( \frac{m_{\text{p}}}{\rho_{\text{NEO}}} \right) \left( \frac{g_{\text{NEO}} r_{\text{p}}}{v_{\text{p}}^2} \right)^{-\frac{3\mu}{2+\mu}} \left( \frac{\rho_{\text{NEO}}}{\rho_{\text{p}}} \right)^{\frac{\mu}{2+\mu}} \quad . \quad (2.52)$$

The strength regime or strength-dominated cratering is given by  $g \ll \bar{Y}$ , as more energy is needed to break the material apart than ejecting the crater material. It can be written as:

$$V_{\text{crater,s}} = K_1 \left( \frac{m_{\text{p}}}{\rho_{\text{NEO}}} \right) \left( \frac{\bar{Y}}{\rho_{\text{NEO}} v_{\text{p}}^2} \right)^{-\frac{3\mu}{2}} \quad . \quad (2.53)$$

The diameter  $d_{\text{crater}}$  of the transient crater and the approximated depth  $z_{\text{crater}}$  can be calculated with:

$$d_{\text{crater}} = \sqrt[3]{\frac{24}{\pi} V_{\text{crater}}} \quad , \quad (2.54)$$

Material	$K_1$	$\mu$	$\bar{Y}$ [MPa]	$\rho_{\text{NEO}}$ [ $\frac{\text{kg}}{\text{m}^3}$ ]
Dry soil	0.24	0.41	0.18	1500
Wet soil	0.20	0.55	1.14	2000
Soft rock	0.20	0.55	7.6	2250
Hard rock	0.20	0.55	18.0	2500

Table 2.4: The table shows various common target properties derived by cratering experiments.

Source: Richardson et al. (2007) and Holsapple (1993)

$$z_{\text{crater}} \approx \frac{1}{3}d_{\text{crater}} \quad . \quad (2.55)$$

We can plot the crater diameter for the given materials of Tab.2.4 and the Breakthrough Starshot specifications of Tab.2.1 and Tab.2.2 as function of the NEO bulk density, done in Fig.2.23. There is no difference noticeable if  $r_{\text{p,sph}}$  or  $\rho_{\text{p,sph}}$  is used. The markers show the position of the densities, for which the constants were determined in the experiments by Holsapple (1993), as listed in Tab.2.4. The plots must be treated with caution, since  $\bar{Y}$ ,  $\mu$ , and  $\nu$  do not change with the bulk density here, but for the very few experimental data, especially  $\bar{Y}$  changes with  $\rho_{\text{NEO}}$ . High metallic bulk densities are excluded by purpose in the plot, as the given experimental constants are only for rocky densities and lower. This figure is similar to the work of Richardson et al. (2007), where the Deep Impact missions impact on comet 9P/Tempel 1 was studied, shown in Fig.2.24. The bulk densities are slightly different, as the focus in this work is shifted more to asteroids.

For the strength regime the projectiles, compared to the impactor on 9P/Tempel 1,

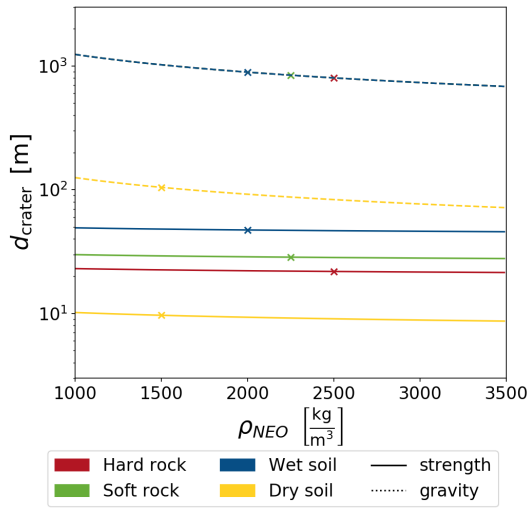


Figure 2.23: Estimates for the transient crater diameter  $d_{\text{crater}}$  caused by projectiles as function of the bulk density  $\rho_{\text{NEO}}$  for various experimental constants in the gravity and strength regime. The markers show the position of the material densities of the experiments for determining the constants.

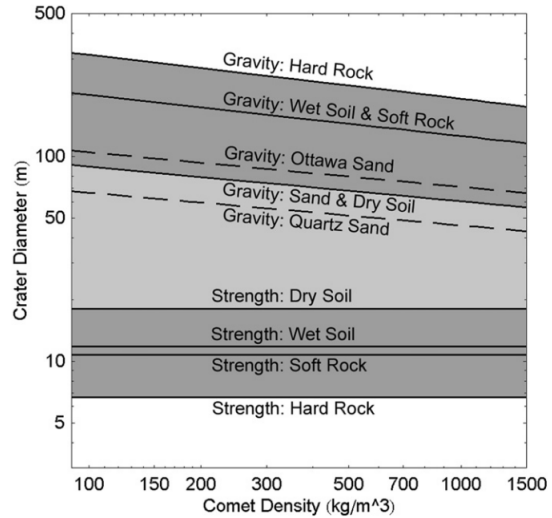


Figure 2.24: Estimates for the transient crater diameter on the comet 9P/Tempel 1 as function of the comet bulk density for various experimental constants in the gravity and strength regime.

Source: Richardson et al. (2007)

cause larger craters. Yet they are only a few times larger and not a full order of magnitude. The size order is of 10 m. The dry soil has the smallest crater size, which is contrary to the Richardson et al. (2007) work. This can be explained by the extremely high velocity of the projectiles, making the bases of the exponentiation in Eq.2.52 and Eq.2.53 very low in general. As a consequence, the lower  $\mu_{\text{drysoil}}$  pushes the curve down, compared to the other  $\mu$ . The transient crater sizes do not change a lot with varying bulk density. For the gravity regime, the craters caused by projectiles would be remarkably larger than the Deep Impact craters, ranging from 100-m to km-size. This is roughly an order of magnitude larger as for the Deep Impact mission. Excluding the dry soil, the other three curves lie on top of each other, why only the hard rock curve is visible in the plot. The transient crater sizes are very slightly increasing with lower bulk densities.

The transient crater diameter  $d_{\text{crater}}$  as function of the NEO diameter  $D_{\text{NEO}}$  for the different materials is shown in Fig.2.25. Here, the bulk densities of Tab.2.4 were taken for the different materials. Again, both regimes are plotted in various line styles. The gray area indicates, if the size of the crater exceeds the size of the NEO, what we identify with the fragmentation of the object.

As the strength regime, given by Eq.(2.53), is not a function of the NEO mass and therefore not a function of the NEO diameter, the associated transient crater diameters are constant. Again, the high velocity is the reason why  $\mu$  gets important and the dry soil diameter is smaller than the others. One can see, that an object in the 10-m-regime gets most likely fragmented. The gravity regime diameters are much bigger, though they decrease with larger NEO sizes. Here, fragmentation would occur for 100-m-sized rocky bodies. However, as discussed in the introduction section, fragmentation and therefore uncontrollable debris, which are still in route of collision, is not the goal of a deflection mission.

Depending on the regime, the outcomes are very different. The strength regime would give much smaller craters than the gravity regime, but the expected crater sizes from the tiny projectiles are still larger than for the Deep Impact mission. Analyzing the sum of Eq.(2.50) reveals the absolute dominance of the first summand, why the impact of the Breakthrough Starshot projectiles should be described in the strength regime. One would expect this for small NEOs, where the gravity is negligible, yet this is not the primary reason. The result is produced by the extreme high velocity of the projectiles and the exponent of the second summand, independent of the NEO size. Please note again, that the experimental constants are derived for hypervelocity experiments with velocities several

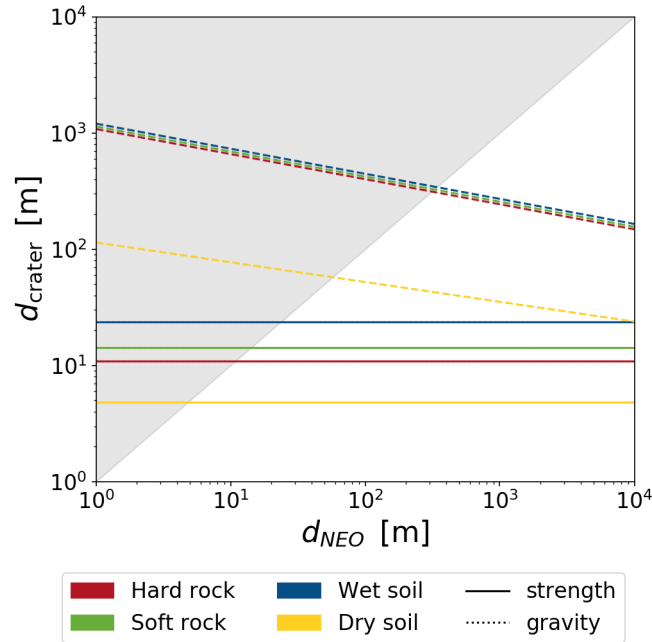


Figure 2.25: Estimates for the transient crater diameter  $d_{\text{crater}}$  caused by projectiles as function of the near-Earth object diameter  $d_{\text{NEO}}$  for various experimental constants in the gravity and strength regime. The near-Earth object is modeled as a sphere. The gray area shows where the size of the crater exceeds the size of the NEO, which we interpret as fragmentation of the body.

orders lower than  $0.2c$  and therefore the results must be treated with caution.

In addition the question arises, if the projectile might be able to penetrate a NEO. In general, the shape of a projectile with a large m-sized cross section by the lightsail is not designed to enter an object, compared to a bullet with a characteristic conical shape. Therefore one would rather expect the destruction of the projectile during the collision and the associated formation of an impact crater than a penetration of the projectile. However, by estimating the crater depth with Eq.(2.55), we can not completely exclude this case for NEOs smaller than roughly 100 m or rubble pile asteroids.

## 2.12 Momentum multiplication for projectile impacts

Since the linear momentum of a system has to be conserved, the ejected crater material leads to an additional velocity change of the NEO. This is quantified by the so-called momentum multiplication factor  $\beta$ , described among others by Housen and Holsapple

(2012) as

$$\beta = 1 + \frac{p_e}{p_{\text{imp}}} = 1 + \frac{p_e}{\gamma(v_{\text{imp}})v_{\text{imp}}m_{\text{imp}}} \quad (2.56)$$

where  $p_e$  is the linear momentum of the escaping ejecta,  $p_{\text{imp}}$  the linear momentum of the impactor and the associated mass  $m_{\text{imp}}$  and velocity  $v_{\text{imp}}$  of the impactor. If no material gets ejected, the factor is  $\beta = 1$ , while escaping ejected material leads to  $\beta > 1$ . However, not all of the ejecta contributes to the  $\beta$ -factor but only the fraction which escapes the gravity field of the object and therefore is larger than the escape velocity (Takeuchi, 2008)

$$v_{\text{esc}} = \sqrt{2G \frac{m_{\text{NEO}}}{d_{\text{NEO}}}} = \sqrt{G \frac{\pi}{3} \rho_{\text{NEO}} d_{\text{NEO}}^2} \quad . \quad (2.57)$$

In this equation we assumed the NEO to be homogeneous and spherically and the escape starts at the surface of the object.

Housen and Holsapple (2012) describes a scaling law for the momentum multiplication factor

$$\beta - 1 \sim (v_{\text{imp}})^{3\mu-1} \quad , \quad (2.58)$$

where  $\mu$  is again an experimental measured constant ranging between  $1/3 \leq \mu \leq 2/3$ . In their work they highlight the porosity to be a key factor in the achievable  $\beta$ . Rocky nonporous materials have large momentum multiplication factors of  $4 \lesssim \beta \lesssim 10$  for conventional kinetic impactor velocities of  $v_{\text{imp}} \approx 10 \frac{\text{km}}{\text{s}}$ . Interpolation to  $v_{\text{imp}} \approx 30 \frac{\text{km}}{\text{s}}$  could lead to factors of  $\beta \approx 20$ . On the other hand, sand as porous material would only have  $\beta \approx 3$  for  $v_{\text{imp}} \approx 30 \frac{\text{km}}{\text{s}}$ . Even more porous material might closely stick to  $\beta \approx 1$ , as an experiment with a 70% porous pumice showed.

Although it is very unlikely that the high velocity of  $v_p = 0.2c$  is in the valid regime for Eq.(2.58), as all laboratory experiments have orders lower velocities, we use the equation

Material	$C [10^3]$	$\mu$	$\rho_{\text{NEO}} [\frac{\text{kg}}{\text{m}^3}]$
River rock	0.67	0.67	2700
Sand	11.37	0.51	1440

Table 2.5: The table shows the target properties for determining the momentum multiplication factor, reproduced from the plots of (Housen and Holsapple, 2012).  $C$  is the proportionality constant, determined with  $v_{\text{imp}}$  in SI-units.

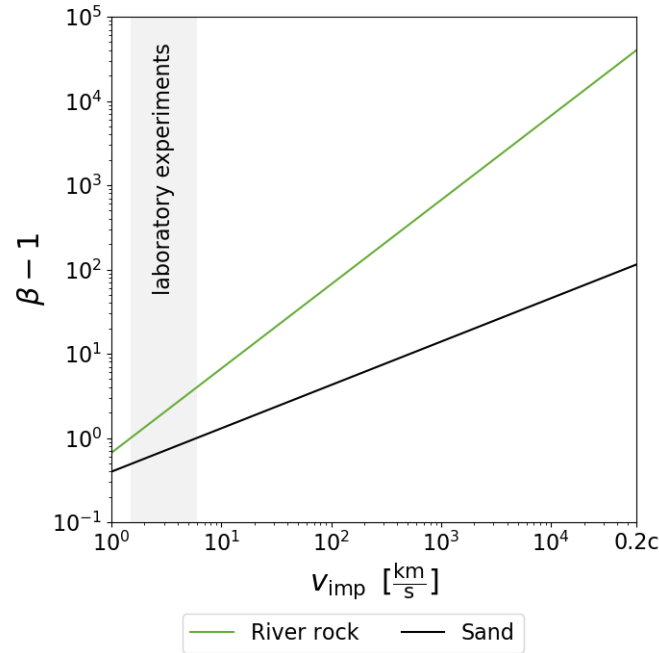


Figure 2.26: The plot shows the interpolated momentum multiplication factor  $\beta$  as function of the impact velocity  $v_{\text{imp}}$  and two different materials, derived by the work and experiments of Housen and Holsapple (2012). The gray area shows the regime of the hypervelocity laboratory experiments. For  $v_{\text{imp}} \approx v_p$ , the resulting  $\beta$  for river rock is in the order of  $10^4$ , yet other materials with other porosities can have tremendously lower momentum multiplication factors.

with the constants of Tab.2.5, together with the specifications of Tab.2.1 and Tab.2.2, to estimate a  $\beta$  for the Breakthrough Starshot projectiles. The proportionality constants are reproduced from the plots of Housen and Holsapple (2012), since only results but no input data were published. The interpolated  $\beta$  is plotted as function of the impact velocity in Fig.2.26, similar to the work of Housen and Holsapple (2012), yet with higher impact velocities  $v_{\text{imp}}$ . The gray area marks the regime of the laboratory experiments.

Since the velocities of Breakthrough Starshot projectiles are orders higher than conventional kinetic impactors, the interpolated momentum multiplication factors are orders higher, too. The river rock allows  $\beta$  of the order of  $10^4$  and even for the sand we get  $\beta \approx 10^2$ . This would dramatically improve the efficiency of the deflection method. However, decreasing the slope for very high porosities would result in very low  $\beta$  close to unity and no noteworthy change of the  $\Delta v$ . As hypervelocity experiments with nowadays technology can not reach the interesting velocity regime for this deflection method, computer simulations might shed some light on the cratering, material ejection and momentum

multiplication in the future.

In contrast to theoretical derivations, numerical modeling and laboratory experiments, the momentum multiplication factor for an actual deflection is still unknown and should be determined by at least one or more test deflections in space. This is one of the key goals of the AIDA mission for a kinetic impactor (Cheng et al., 2018). If the Breakthrough Starshot technology for the main mission would be operational, test shots to the moon could be done for investigating the crater formation by projectiles, as long as this would be compliant with the *Outer Space Treaty*. Anyway, even with test missions the  $\beta$ -factor will still be an uncertainty, as it depends on numerous factors and hence might change from one body to another. Therefore discussions at the *Near-Earth objects scientific programme* of the *Munich Institute for Astro- and Particle Physics* (MIAPP) of the DFG cluster of excellence *Origin and Structure of the Universe* revealed, that planetary defense can not rely on best case scenarios. NEO deflection should be successful for a low momentum multiplication factor or even  $\beta = 1$ , too.

## 2.13 Projectiles in interplanetary space

The interplanetary space is not empty but full of small micrometeorites and dust which might hit and interact with the projectiles during traveling. As mentioned by Grün et al. (1985) and Lubin (2016) the dust in the Solar System is concentrated in the ecliptic plain. For planetary defense, in contrast to interstellar flight, the higher dust concentration in the ecliptic is relevant, as most of the NEOs are distributed close to the ecliptic.

Grün et al. (1985) reports a total mass density of  $\rho_{\text{dust}} = 9.6 \times 10^{-20} \frac{\text{kg}}{\text{m}^3}$  in the ecliptic plane at 1 AU distance to the Sun. If we assume perfectly inelastic collisions of this material with a projectile, the velocity of the projectile decreases. Due to the high velocity of the projectiles, we set  $v_{\text{dust}} = 0 \frac{\text{km}}{\text{s}}$ . In reality, some micrometeorites might hit through the projectile, why the model gives a lower limit of the decelerated projectile velocity  $v_{\text{p,dec}}$  for a given traveled distance  $D$ . It can be derived by the linear momentum conservation to:

$$v_{\text{p,dec}} = \frac{m_{\text{p}} v_{\text{p}}}{m_{\text{p}} + \rho_{\text{dust}} \pi \left(\frac{d_{\text{p}}}{2}\right)^2 D} \quad , \quad (2.59)$$

where  $d_{\text{p}}$  is the diameter of the projectile, listed in Tab2.1. The result can be seen in Fig.2.27. The velocity is given in units of  $0.2c$ , which equals the final achieved velocity by the acceleration of the lasers. For a travel distance of  $D = 1 \text{ AU}$ , which is marked by the

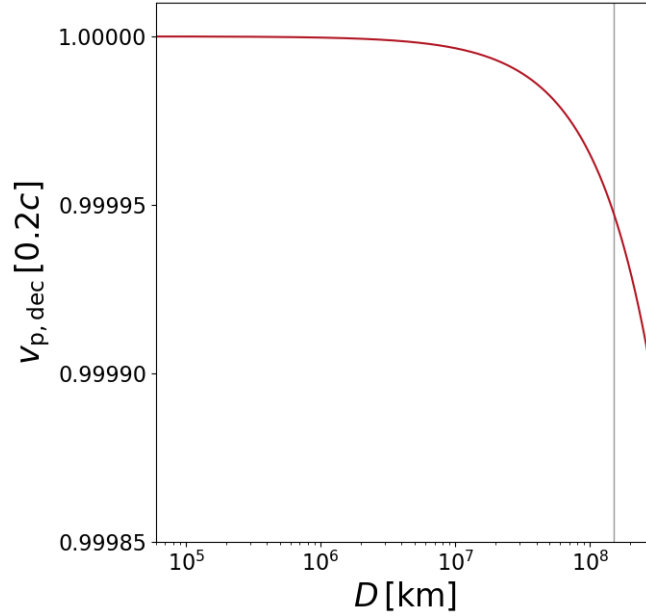


Figure 2.27: The plot shows the evolution of the projectile velocity  $v_{p,\text{dec}}$  with deceleration by interplanetary dust as function of the traveled distance  $D$ . For traveling distances of the order of AU, the loss in velocity is tiny with an order of 0.01%.

gray vertical line, the loss in velocity is only in the order of 0.005%, which is negligible for the calculations of planetary defense.

Grün et al. (1985) also derives a cumulative spatial density of interplanetary dust  $\mathcal{N}$  as function of the individual dust mass by a micrometeoroid flux model. For a distance of 1 AU to the Sun, it is

$$\mathcal{N} = -m \ln(10) \frac{k}{v_0} \frac{d\mathcal{F}(m)}{dm} \quad (2.60)$$

with  $v_0 = 20 \frac{\text{km}}{\text{s}}$  as meteoroid speed, a constant  $k = 4$  for an isotropic flux and the cumulative interplanetary meteoroid flux

$$\begin{aligned} \mathcal{F}(m) = & (2.2 \times 10^3 m^{0.306} + 15)^{-4.38} + 1.3 \times 10^{-9} (m + 10^{11} m^2 \\ & + 10^{27} m^4)^{-0.36} + 1.3 \times 10^{-16} (m + 10^6 m^2)^{-0.85} \end{aligned} \quad (2.61)$$

at 1 AU. According to Grün et al. (1985), the values were found by fitting the function on data from HEOS 2, Pioneer 8 and Pioneer 9 spacecrafts.

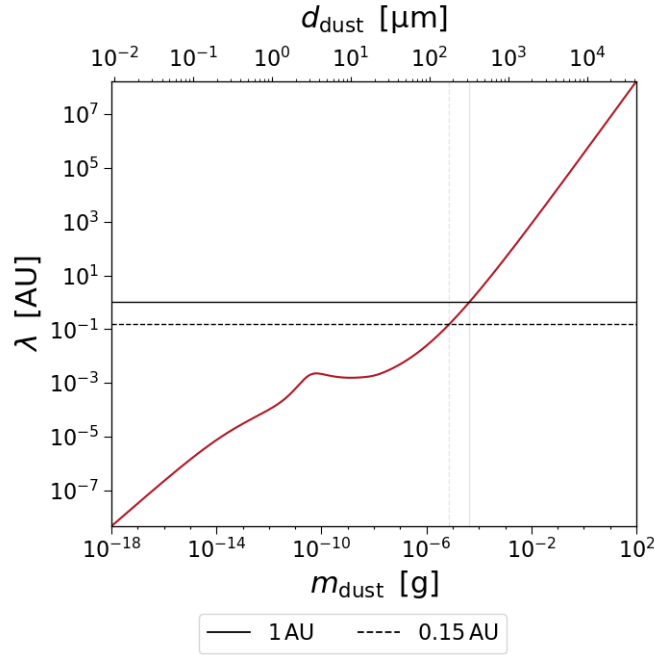


Figure 2.28: The plot shows the mean free path  $\lambda$  as function of the individual dust mass  $m_{\text{dust}}$  or the spherically approximated diameter of the dust  $d_{\text{dust}}$  with a bulk density of  $\rho_{\text{dust}} = 2.5 \frac{\text{kg}}{\text{dm}^3}$ . The horizontal lines show the mean free path of  $\lambda = 1 \text{ AU}$  and  $\lambda = 0.15 \text{ AU}$ , which are the length scales of a possible deflection distance and the end of the acceleration zone.

Now we can use the mean free path  $\lambda$ , as described by Ghisellini (2013)

$$\lambda = \frac{1}{\mathcal{N}\sigma} = \frac{1}{\mathcal{N}\pi\left(\frac{d_p}{2}\right)^2} \quad (2.62)$$

to estimate the sizes of the particles, which typically collide with the projectiles during the interplanetary travel. Here,  $\sigma = (d_p/2)^2$  is the cross section, simplified due to  $d_p/2 \gg r_{\text{dust}}$ .

The mean free path  $\lambda$  as function of the individual dust masses  $m_{\text{dust}}$  or as function of the diameters  $d_{\text{dust}}$  of spherically approximated dust grains with a bulk density  $\rho_{\text{dust}} = 2500 \frac{\text{kg}}{\text{m}^3}$  (Grün et al., 1985) is shown in Fig.2.28. We see that for  $\lambda = 0.15 \text{ AU}$ , the dust size is roughly  $2 \times 10^2 \mu\text{m}$  with a mass of about  $10^{-5} \text{ g}$ . Those values represent the biggest and most massive micrometeorites which we typically expect to collide with the projectile during its acceleration. Accordingly, smaller and less massive objects will hit the projectile even more often. For a larger travel distance in the order of  $\lambda = 1 \text{ AU}$ , the common maximum dust size increases to around  $3 \times 10^2 \mu\text{m}$  with a mass between  $10^{-5} \text{ g} \leq m_{\text{dust}} \leq 10^{-4} \text{ g}$ . Hence, the projectiles have to sustain collisions with the mentioned size

and mass orders, otherwise the projectiles might get destroyed or perturbed during their travel to the near-Earth object.

Lubin (2016) warns that mm-sized micrometeorites might cause catastrophic damage to the affected area. Independently, futures studies have to precisely analyze the damage by the dust collisions and must obtain a hazardous dust size limit. In particular the smaller and less massive micrometeorites, which impact not only infrequent, but for sure many times during the travel, pose a great danger for the reliability of the Breakthrough NEO deflection concept.

## 2.14 Location of light beamers

Proxima Centauri has a declination of  $\delta = -62^{\circ}40'46.1631''$  and a right ascension of  $\alpha = 14^{\text{h}}29^{\text{m}}42.94853^{\text{s}}$  (SIMBAD Astronomical Database, 2018). Therefore the best location for the lasers would be at the latitude of  $\Phi \approx -62.5^{\circ}$ , because at least once every day Proxima Centauri would be right at the zenith. As the altitude of the location is neglected, the laser beams have the shortest path through the atmosphere and hence the lowest disturbance and attenuation, if they point to the zenith. Unfortunately, no continent is directly at this latitude, but only the island Livingston. The island is part of the Antarctica, whose continental mainland is located a bit more southern.

For near-Earth objects the situation is different. On the one hand they are dominated by asteroids, which have a tendency to low inclinations. Chesley and Spahr (2004) show that PHAs and the impactor population have even stronger foci on low inclinations, why we concentrate in the following on the ecliptic. On the other hand, the bodies are moving and hence their true anomaly  $\nu$  is changing continuously, leading to changing  $\alpha$ . Furthermore, there is not only one NEO but many of them in the night and day sky with different  $\alpha$ . Hence, there is not a fixed direction where to shot as for Proxima Centauri, why the equatorial region at  $\Phi = 0^{\circ}$  would be the best location for the lasers concerning planetary defense. The lasers might not necessarily only fire if they point directly to the zenith, but might be also able to fire if they have certain angle deviation to the zenith. We call the maximum possible angle deviation  $\zeta$ . This leads to a cone of possible laser directions, depending on  $\zeta$ . This cone is rotating around Earth and cuts the ecliptic, which determines the parts of the ecliptic that can be illuminated by the lasers. The light beamers do not directly target the NEOs, but the projectiles, though the projectiles are basically extensions of the light beam in a nearly straight line when traveling to the bodies. The

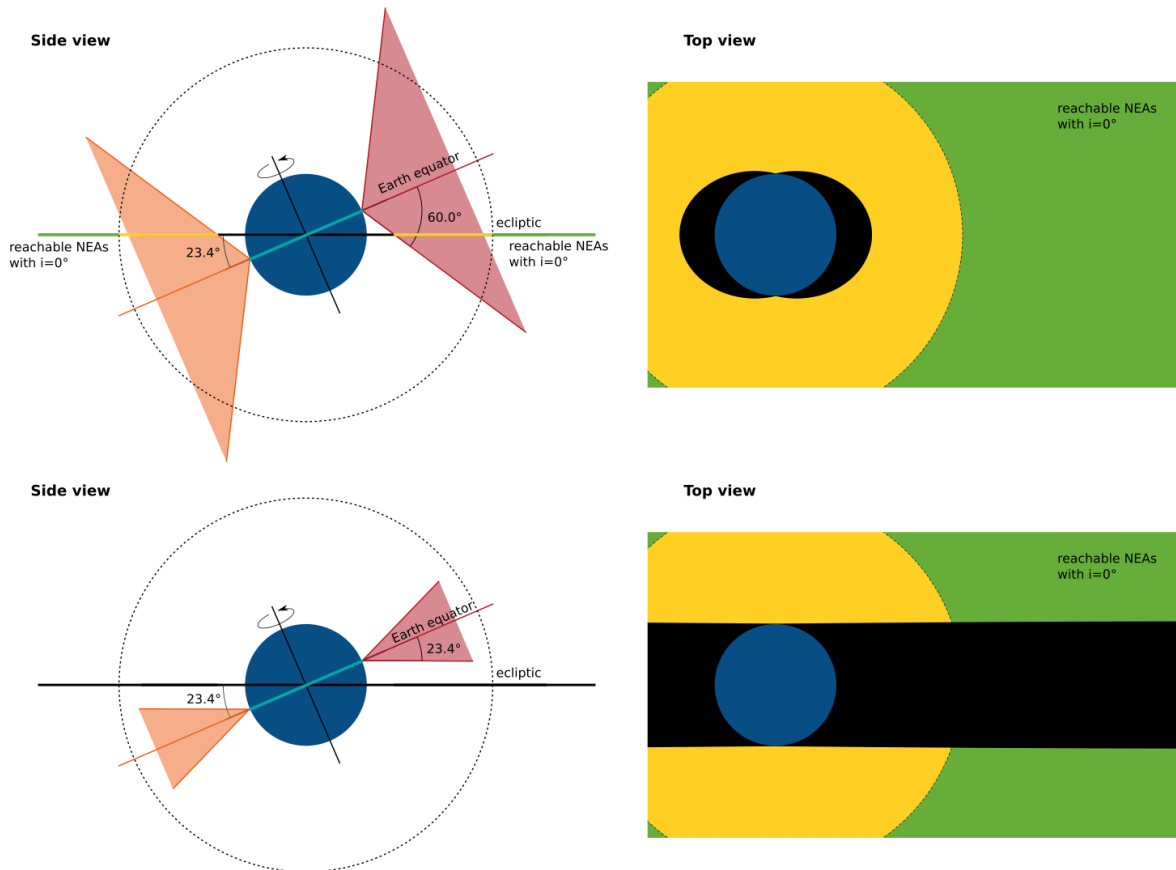


Figure 2.29: The sketch shows the side view of Earth with the light beamers at the equator. The two triangles represent the sectional plane of the extreme cases beam cones at their maximum inclinations to the ecliptic. The black part of the ecliptic can not be targeted with the lasers, while the green part is reachable. The yellow part can be targeted, yet is inside the dashed circle, which marks the initial displacement of the projectiles or the acceleration zone. The top view shows the three regions of the ecliptic again. The upper sketch has an angle deviation to the zenith  $\zeta = 60^\circ$ , where almost all of the ecliptic can be targeted within one rotation of Earth and the non-reachable part has the shape of two overlapping ellipses. The lower sketch has  $\zeta = 23.4^\circ$ , which is the same angle as the inclination of the Earth equator to the ecliptic. Here, the non-reachable area extends to infinity with right ascensions of  $\alpha = 6^{\text{h}}$  and  $\alpha = 18^{\text{h}}$ . For even smaller angles, the black zone broadens, until  $\zeta \approx 0^\circ$  leads to a reachable part in the shape of sharp, straight lines in  $\alpha = 0^{\text{h}}$  and  $\alpha = 12^{\text{h}}$  direction.

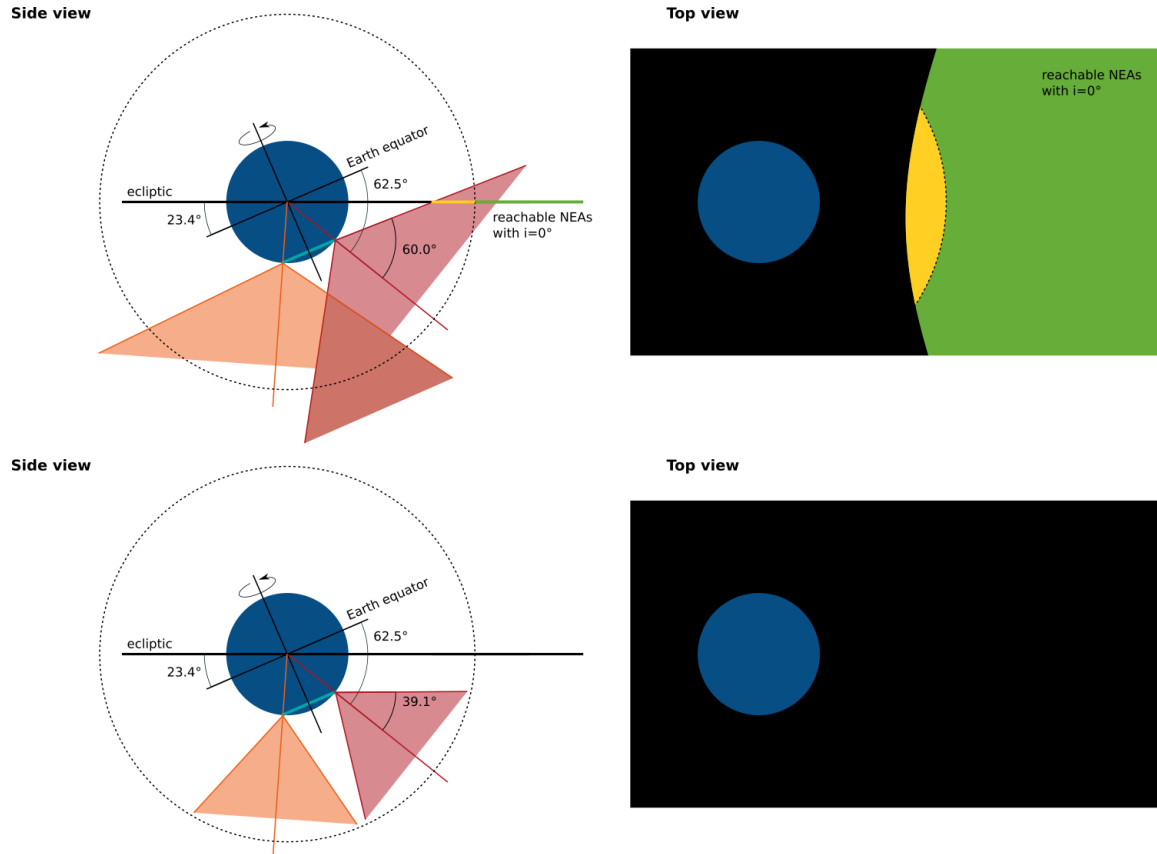


Figure 2.30: The illustration shows the side view of Earth with the light beamers at latitude  $\Phi = -62.5^\circ$ , which is the best position for shooting nanocrafts to Proxima Centauri. The two triangles represent the sectional plane of the extreme cases beam cones at their maximum inclinations to the ecliptic. The black part of the ecliptic can not be targeted with the lasers, while the green part is reachable. The yellow part can be targeted, yet is inside the dashed circle, which marks the initial displacement of the projectiles or the acceleration zone. The top view shows the three regions of the ecliptic again. For  $\zeta = 60^\circ$  in the upper sketch, only a limited part of the ecliptic with a direction to  $\alpha = 18^{\text{h}}$  can be reached. This direction is independently of the epoch. For  $\zeta \leq 39.1^\circ$ , the ecliptic is fully unreachable.

above-mentioned scenario can be seen in the upper illustration of Fig.2.29, where in the side view the sectional plane of the two extreme case cones with the maximum inclination angle in opposite directions are shown. While Earth is rotating, the inclinations oscillate between those maximum inclinations. We arbitrarily chose  $\zeta = 60^\circ$  as a first assumption, though this must be adjusted as soon as new information about the acceleration technology of Breakthrough Starshot is published. For the illustrated extreme cases, a small offset in the ecliptic from Earth, marked with black, can not be targeted by the lasers. If the laser position is  $i = 0^\circ$ , which happens two times during a full rotation, the lasers are in the ecliptic and there is no offset. The shape of the ecliptic, which can not be illuminated, are two overlapping ellipses, depending on  $\zeta$ , as shown in the top view. A full rotation of Earth enables the lasers to illuminate almost the full ecliptic, illustrated with green, depending on the laser angle. Hence, the limiting factor if near-Earth objects in the ecliptic can be targeted or not, might be only the initial sail displacement of  $60 \times 10^3$  km or the end of the acceleration zone at 0.15 AU, as described by Parkin (2018), marked with yellow and the dashed circle around Earth. This area in the sketch is for none of the zones in scale, but only for illustration. As  $\zeta$  shrinks, a smaller fraction of the ecliptic can be targeted. For the case of  $\zeta = 23.4^\circ$ , the ecliptic can not be illuminated at the extrema of the laser inclinations, why a non-reachable area extends to infinity in the  $\alpha = 6^{\text{h}}$  and  $\alpha = 18^{\text{h}}$  direction. This is shown in the lower illustration of Fig.2.29. As  $\zeta \approx 0^\circ$ , the intersection with the ecliptic and therefore the reachable part is almost a straight line in  $\alpha = 0^{\text{h}}$  and  $\alpha = 12^{\text{h}}$  direction.

Besides, when firing the lasers from the equator, one has to take into account that geostationary satellites might be in between the laser and the projectiles, which are waiting in their gateway orbit for departure.

The NEO deflection with lasers around  $\Phi = -62.5^\circ$  is more difficult. A sketch of this scenario can be seen in the upper illustration of Fig.2.30, where we again arbitrarily chose  $\zeta = 60^\circ$  as limit of the lasers. The ecliptic can be reached only for a small period why only a very limited part can be targeted. This part has a preference to  $\alpha = 18^{\text{h}}$ , independent of the epoch. For  $\zeta \leq 39.1^\circ$ , the ecliptic can never be reached, shown in the lower illustration of Fig.2.30.

The position of the laser is very important for NEO deflection, as only a part of the sky can be covered by a single laser, even for a full rotation of Earth. Similar to astronomical observations, a laser southern to the equator can reach mostly NEOs of the southern hemisphere and vice versa. This is important for comets, which have orbits not necessarily

close to the ecliptic. Asteroids have a preference to low inclinations, why a location at the equator seems the best solution for planetary defense, yet not for sending nanocrafts to Proxima Centauri, why we have clearly a clash of interests for the location site. In addition, the maximum angle deviation to the zenith  $\zeta$  plays also a huge role, as it broadens or shrinks the non-reachable area tremendously.

The various tangential speeds of Earth at different latitudes due to its rotation is another aspect which must be considered, as the zenith is passing by quicker for a faster speed and hence the targeting of the projectiles by the light beamers might be more difficult. With a sidereal day of  $T_{\oplus} \approx 23 \text{ h } 56 \text{ min } 4 \text{ s}$ , the tangential speed of Earth  $v_{\text{tan}}$  at the Equator is roughly  $464.6 \frac{\text{m}}{\text{s}}$ , while at a latitude of  $\Phi \approx -62.5^\circ$ , the speed is only approximately  $214.5 \frac{\text{m}}{\text{s}}$ . The tangential speed of Earth at the equator is hence twice as quick as on the best location for the Breakthrough Starshot main mission. Here, we need more information of the acceleration technology to check, if there could be another conflict.

# Chapter 3

## Deflection simulation

### 3.1 MAIDS code

The *massive asteroid impact deflection simulation* (MAIDS) is a self-written 3D-code to simulate the deflection of impacting NEOs. Here, not only a single object can be simulated, but many bodies with various orbits, properties and deflection starting times. Any deflection method can be implemented, yet as for this thesis only the Breakthrough Starshot projectiles are considered, only this deflection method is ready for use.

The simulation is done in the three-dimensional space with the Sun at origin. The movement of the Earth and the spherically approximated NEOs are computed with the Leapfrog integrator, as for this time integration the energy is conserved in a longterm and for fixed timesteps the simulation is time reversible (Benacquista and Romano, 2018). At first, the orbits of the impacting NEOs are determined, depending on the chosen input. To ensure an impact on Earth, all impactors start at the same position as Earth. Then, a backward integration determines the initial position and velocity for the actual computation. Here, only the Sun's gravity is treated. Obviously neglecting the gravity of the Moon, Earth and the other planets is physically not correct, yet this makes the simulation independent of the epoch, ensures the initial determined orbit of the NEOs and lowers the computational costs. As a result, no orbit changes by close encounters are taken into account. During the forward integration, the deflection by Breakthrough Starshot projectiles is added, where the linear momentum transfer but no momentum multiplication is considered. The limits of the minimum deflection distance are set to the initial distance of the projectiles and for deflection in the acceleration zone, a constant acceleration is taken into account for simplicity reasons. The travel time, perturbations on the projectiles and

interstellar dust which might damage the projectiles are neglected. The distance to Earth is checked for the time around the scheduled impacts to recognize the impacts. An impact is given if the distance is lower than an enlarged effective radius of Earth, which includes the acceleration of Earth. Due to the enlargement, no false negative impacts are missed, yet we get false positive impacts. Therefore the simulation results can be seen as a worst case. To ensure that no impact is missed, the timesteps are shrunked shortly before the scheduled impacts. In addition, the simulation is extended a bit to recognize late arriving impactors. All masses are kept constant, why fragmentation is fully neglected and no porosity is considered. Furthermore, we do not include a position uncertainty, but every NEO location is perfectly known.

More details of the code can be found in App.A.

### 3.2 Setup and impactor populations

The deflection starting time for the simulations is set to  $t_{\text{def},1} = 10 \text{ yr}$  or  $t_{\text{def},1} = 25 \text{ yr}$ . Those values are chosen since the overall goal is to find a deflection method which can be done in a reasonable time frame. On the other hand, this limits the computational costs.

We choose two different ways of setting up the NEO orbits for the deflection. On the one hand, we use 21272 synthetic impactor orbits by Chesley and Spahr (2004), where the semi-major axis  $a$ , eccentricity  $e$  and inclination  $i$  are used. For the argument of periapsis  $\omega$ , two different cases can be used, realizing the impact of the body on Earth, doubling the impactor orbit number to 42544. All other parameters are fixed due to the requirement of the impact.

To set up the physical properties of the synthetic impactors, we apply the cumulative size distribution of Stuart and Binzel (2004) to get realistic diameters of the objects. In this simulation we use sizes of  $50 \text{ m} \leq d_{\text{NEO}} \leq 500 \text{ m}$ , as those objects might be deflectable with the Breakthrough Starshot technology. As result of the distribution, most of the objects have diameters of the lower end, while only few have the diameters of the upper end. For the bulk density we differentiate between dark NEOs with  $\rho_{\text{NEO,dark}} = 1400 \frac{\text{kg}}{\text{m}^3}$  and bright NEOs with  $\rho_{\text{NEO,bright}} = 2700 \frac{\text{kg}}{\text{m}^3}$ . The dark-to-bright ratio is given by 1.6 (Stuart and Binzel, 2004). Both, the sizes and densities are randomly distributed among the orbits.

The second orbit setup is done with the PHA list of ESA NEO Coordination Centre (2018). Their orbits do not necessarily ensure an impact on Earth, why we slightly modify the eccentricity to realize an impact. At the beginning of July 2018, 1908 PHAs are

known. This number is again doubled due to  $\omega$  to 3816. Here, information about the absolute magnitude  $H$  is provided too, why we can determine the diameters and masses by randomly picking the dark or bright NEO albedo and density.

More details of the setup can be found in App.B.

### 3.3 Results

We analyze the normalized number of successful deflections  $n_{\text{def}}/n_{\text{all}}$  as function of the amplification factor of the targeting angle  $\chi$  in Fig.3.1 for the synthetic impactor population and Fig.3.2 for ESA's PHA population.  $\chi$  indicates, how much better the targeting angle in relation to the standard targeting angle of  $\alpha_{\text{tar,max}}$  was chosen for the simulation. The various colors indicate the different shot frequencies  $s$ . In addition, the right columns show the average number of projectile impacts on a NEO  $\bar{n}_{\text{hits}}$  for different  $s$  as function of  $\chi$ . The markers and line styles represent the impacts inside the acceleration zone with only a fraction of the final velocity, outside the acceleration zone with full speed  $0.2c$  and the sum of both. The upper rows are the results for  $t_{\text{def},1} = 10$  yr simulations and the lower rows for  $t_{\text{def},1} = 25$  yr. The lines have no physically meaning, but are only shown for a better orientation. For all simulations we have *independent firing*, which means a projectile is always fired if possible, independently of the relative movement of the NEO to Earth.

In general, we see that the deflection success increases with a larger  $s$ , as in average more projectiles hit the object and hence more momentum is transferred. Moreover, a rising  $\chi$  has a similar effect, until a threshold of  $\chi$  is reached where  $\bar{n}_{\text{hits}}$  and  $n_{\text{def}}/n_{\text{all}}$  stays constant. For a certain targeting precision, nearly every projectile hits and therefore a further improvement does not change the defense success. This plateau can be seen in the individual curves for the acceleration zone and for full speed too, where the threshold of  $\chi$  in the acceleration zone is reached for lower values. As one would expect, the hits are dominated at first by impacts in the acceleration zone, as here the distance to Earth is lower and the impact probability is higher. For larger  $\chi$ , impacts with full speed dominate, because the space outside the acceleration zone clearly exceeds the space inside this zone and more projectiles can hit.

The comparison of the 10 year and 25 year simulation confirms, that a longer deflection time leads to higher success, since more projectiles can be shot and less velocity change  $\Delta v_r$  is required for earlier deflection date. The deflection success is very different for the two populations, too. Here the main reason is the different size distribution, as the synthetic

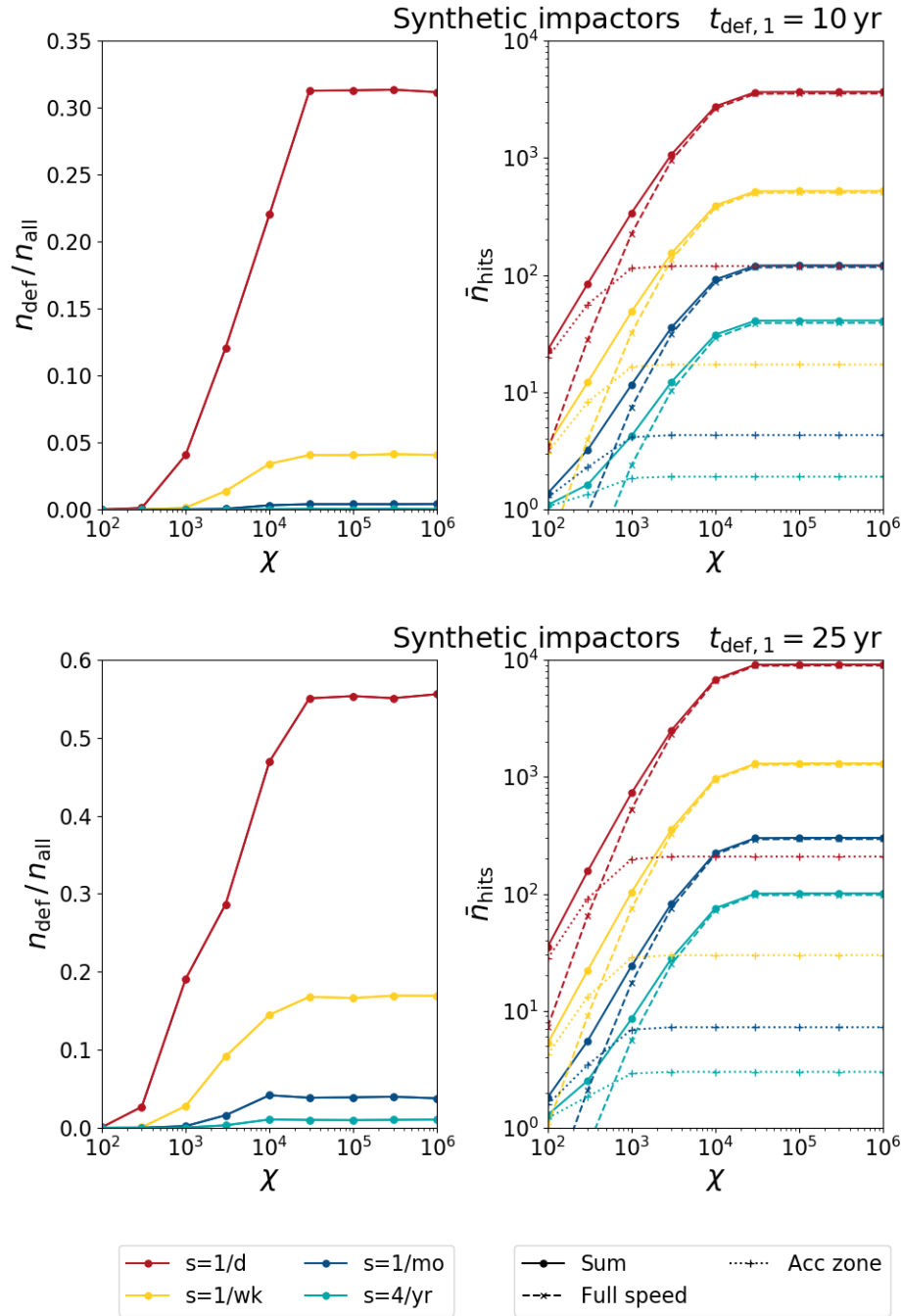


Figure 3.1: The plot shows the deflection simulation of synthetic impactors. The left figures show the normalized number of successfully deflected NEOs  $n_{\text{def}}/n_{\text{all}}$  as function of the amplification factor of the targeting angle  $\chi$ . The various colors represent different shot frequencies. The right plots show the average number of projectile impacts on a NEO  $\bar{n}_{\text{hits}}$  as function of  $\chi$ , again with the different colors for  $s$ . The markers and line styles distinguish the impacts inside the acceleration zone with a fraction of  $0.2c$ , outside the acceleration zone with full speed  $0.2c$  and the sum of both. The upper row shows the  $t_{\text{def},1} = 10 \text{ yr}$  simulation and the lower row has a simulation time of  $t_{\text{def},1} = 25 \text{ yr}$ .

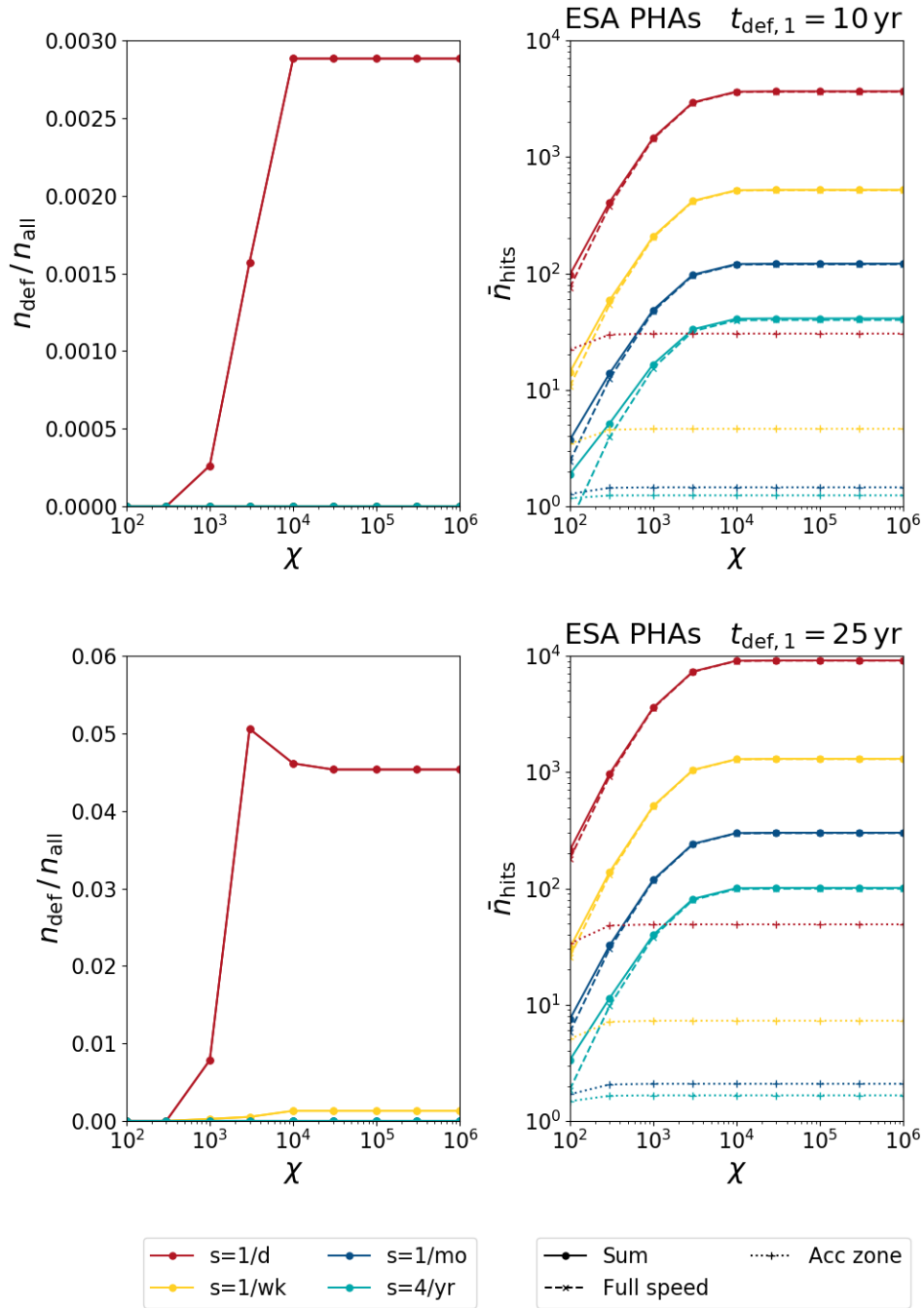


Figure 3.2: The plot shows the deflection simulation of the ESA’s PHA impactors. The left figures show the normalized number of successfully deflected NEOs  $n_{\text{def}}/n_{\text{all}}$  as function of the amplification factor of the targeting angle  $\chi$ . The various colors represent different shot frequencies. The right plots show the average number of projectile impacts on a NEO  $\bar{n}_{\text{hits}}$  as function of  $\chi$ , again with the different colors for  $s$ . The markers and line styles distinguish the impacts inside the acceleration zone with a fraction of  $0.2c$ , outside the acceleration zone with full speed  $0.2c$  and the sum of both. The upper row shows the  $t_{\text{def},1} = 10 \text{ yr}$  simulation and the lower row has a simulation time of  $t_{\text{def},1} = 25 \text{ yr}$ .

impactors with  $50 \text{ m} \leq d_{\text{NEO}} \leq 500 \text{ m}$  are dominated by small objects. On the other hand, the smallest body of ESA's PHA population is by definition roughly 140 m and the sizes are reaching up to several km.

The threshold for  $\chi$  of the synthetic impactors is around  $10^4$ , which is in good agreement with the theoretically determined value of Sec.2.7. For 25 years we get a maximum of roughly 55% deflection success for  $s = 1/a$  and for 10 years the success is about 30%. The threshold for the real PHAs is with roughly  $3 \times 10^3$  a bit lower than for the other population, as the PHAs are on average larger and the plateau is reached quicker. The maximum deflection success for  $s = 1/a$  is only about 4% for 25 years and 0.03% for 10 years. The origin of the peak of deflected NEOs at  $\chi = 3 \times 10^3$  in the ESA PHA 25 year simulation is still unclear, as no outlier can be seen in the average number of hits. Hence, the answer might be a strong difference in impact number between the individual objects, or special constellations with lower required velocity changes.

Detailed analysis of the  $t_{\text{def},1} = 25 \text{ yr}$ ,  $s = 1/a$  simulations can be seen in Fig.3.3, where the upper row shows histograms of the synthetic impactors and the lower row the real PHAs. Again, we see the normalized number of successfully deflected NEOs  $n_{\text{def}}/n_{\text{all}}$ , though now for the individual bins. The results depend on the eccentricity  $e$ , semi-major axis  $a$ , inclination  $i$  and NEO size  $d_{\text{NEO}}$ . The different colors indicate the amplification factors of the targeting angle  $\chi$ .

The synthetic impactors clearly show a trend to a better deflection for higher  $e$  and  $a$ . Both quantities are connected, as a NEO with low eccentricity must have a semi-major axis near 1 AU. On the other hand, large objects with large eccentricities have a larger semi-major axis or one which is significantly smaller than 1 AU. Otherwise the orbit would not cross the Earth orbit and therefore would not be an Earth impactor. Bodies with higher  $i$  are also easier for planetary defense. Those trends are not surprising, since they can be reproduced by Eq.(2.4) – Eq.(2.6) for the required velocity change. As expected, the successful number of deflection shrinks with larger NEO size. For bin  $100^\circ \leq i \leq 120^\circ$  no values are shown as no NEO of the population has this inclination.

The situation for ESA's PHA population is slightly different. We see that for the real objects there is no clear trend in  $e$ . For larger  $a$ , the success increases at first until roughly  $3 \text{ AU} \lesssim a \lesssim 3.5 \text{ AU}$ , where it starts to decrease again.  $i$  has also a maximum and decreases roughly at  $25^\circ$ . Only the decreasing trend with increasing size is clearly similar to the synthetic impactors. Though we have to take care in drawing statistical conclusions by the PHA population, as this is not a large, artificial population with randomly distributed

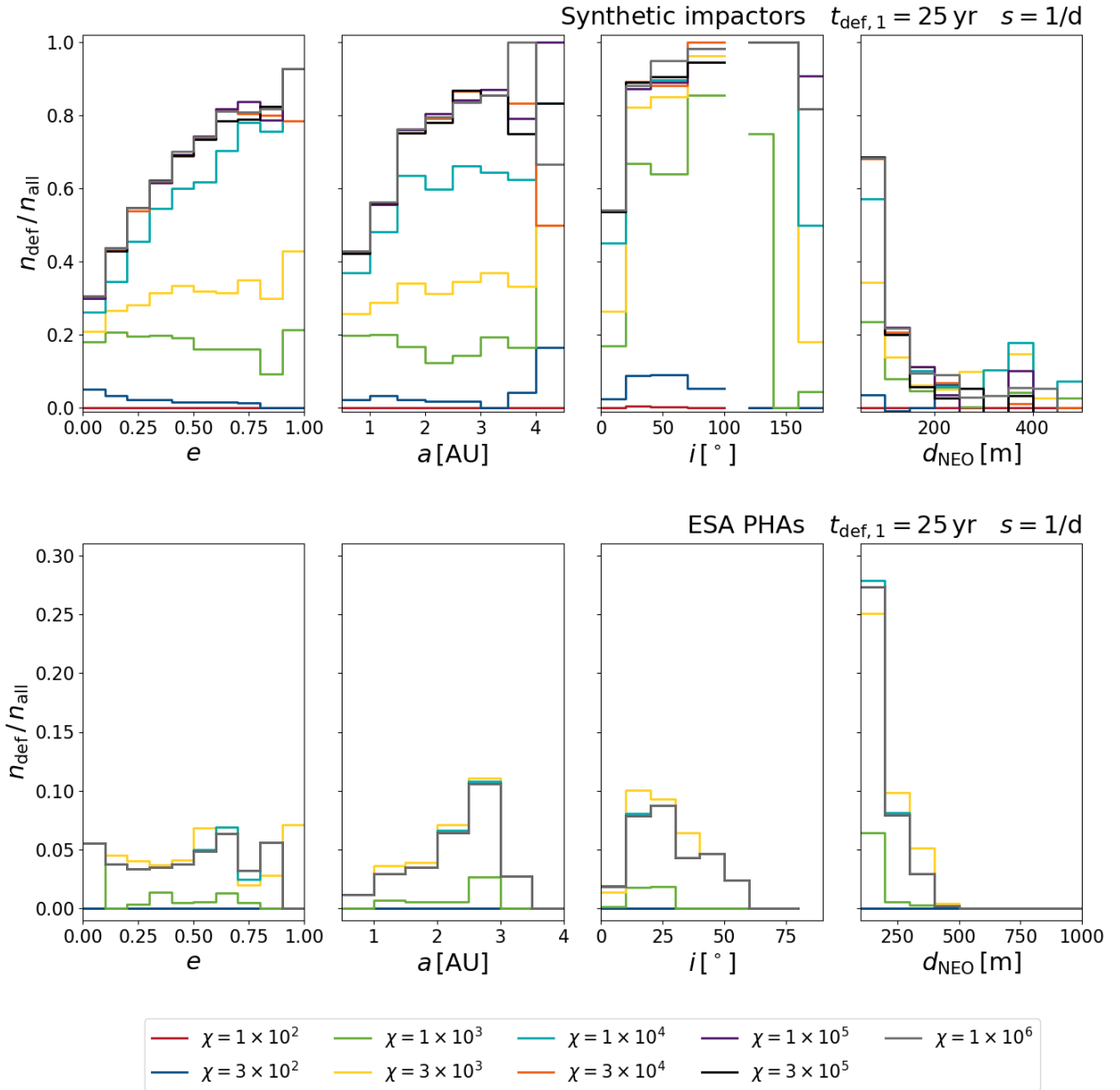


Figure 3.3: The histograms show the normalized number of successfully deflected NEOs  $n_{\text{def}}/n_{\text{all}}$  per bin for the synthetic impactor population in the upper row and the ESA PHA population in the lower row. They are given as function of the eccentricity  $e$ , semi-major axis  $a$ , inclination  $i$  and NEO size  $d_{\text{NEO}}$ . The colors represent the various amplification factors of the targeting angle  $\chi$ . Only the data of the 25 year and  $s = 1/d$  simulations are used.

properties, but a small population with individual properties of the objects. Hence, those individual properties of a few objects dominate parts of the histograms. In more detail, there are no objects with  $i \geq 60^\circ$  or  $a \geq 3$  AU in the population, which have  $d_{\text{NEO}} \leq 500\text{m}$  and in the range of  $30^\circ \leq i \leq 90^\circ$ , only approximately 36% are  $d_{\text{NEO}} \leq 500\text{m}$ . This is the reason why we do not see the similar increasing trend of  $a$  and  $i$  at the PHA histograms as for the synthetic impactors. This lack of objects is simply an observational bias, as it is easier to find large objects and usually NEO surveys focus on lower inclinations, as there is a higher chance of finding new small bodies in the Solar System. In contrast to the synthetic impactor histograms, where many lines and an evolution to better deflection with increasing  $\chi$  can be seen, the PHA histograms show a very few lines. Here, the deflection success is soaring to its maximum very quickly when reaching the proper  $\chi$ , why only less lines are in-between the lowermost and uppermost lines. This rapid jump in success can be noticed by comparing Fig.3.1 with Fig.3.2, too. Hence, most of the lines overlap and therefore simply hide behind other lines.

The numerical error of the simulation for the time integration is marginal and does not lead to any uncertain deflection, why no error bars are shown in the  $n_{\text{def}}/n_{\text{all}}$  plots and histograms.

# Chapter 4

## Summary and outlook

There is a huge diversity in small bodies in the Solar System and some of them regularly cross the orbit of Earth. Historic impacts of such objects are recorded by impact craters, though close approaches, atmospheric entries and ground impacts happen nowadays, too. Depending on the properties of the near-Earth object, the consequences can be devastating, why we have to think about mitigating this threat. There are numerous ideas for NEO deflection, each having its individual downsides. Most methods are still concepts and none of them was ever tested until now. Hence, a reliable and affordable deflection method must be found to ensure the safety of the human species.

The Breakthrough Starshot concept aims for interplanetary traveling chip-satellites with lightsails to explore Proxima Centauri within only few decades of travel time. In order to do this, large quantities of few gram light nanocrafts should be accelerated by light beamers to 20% speed of light. This future technology of ultrafast, light spacecrafts could be diverted for planetary defense by using the nanocrafts as low-mass kinetic impactors, which are called projectiles in this work. The principle is based on the linear momentum conservation, as the projectiles transfer their linear momenta to the threatening object and therefore push it out of its original orbit.

The deflection success depends on the start of the deflection, the number of fired projectiles, the shot frequency, the mass and the orbit of the near-Earth object. A single projectile for a perfectly inelastic collision can deflect a stony asteroid with 40 m diameter with a deflection time of roughly 25 years before the impact, though more massive bodies need a larger number of impacting projectiles for deflection. With 100 sent projectiles, one fired per day, a 100 m stony asteroid could be deflected if we start 10 years before the impact. For the same shot rate but 1000 impacts, we can deflect stony asteroids of the size

400 m with a deflection start of 25 years in advance. However, even an earlier mission start or a realistic number of more impacting projectiles does not lead to successful deflection of km-sized objects by pure momentum transfer.

The minimum targeting accuracy of the projectiles is predefined by the main mission of Breakthrough Starshot, as the nanocrafts should enter the planetary system of Proxima Centauri. However, impacting on an object inside the solar system is even more difficult. Although the distances for planetary defense are shorter, the targets are tremendously smaller, why roughly a  $10^3$  times better targeting accuracy is required. With the predefined accuracy, about  $10^9$  shots must be fired to have a 50% chance of hitting at least once a 100 m object at a distance of 1 AU. The use of photon thrusters, which are intended for attitude control on the nanocrafts, for improving the impact probability has no significant effect. Therefore we identify the targeting accuracy as bottleneck of this deflection method. The shot uncertainty is slightly larger than the location uncertainty of the NEOs by optical telescopes, yet of the same order. If a better targeting angle is realized, we need better position data, too. Despite the ultra high velocity of 20% speed of light, the gravity of the Sun and Earth must be taken into account, as the perturbation lead to km-scale or larger displacement of the projectiles to an ideal, straight path. Actually, comets are more problematic than asteroids, since they are further away from Earth in the outer Solar System most of the time and are therefore even more difficult to hit.

Once a threatening object has a close approach to Earth, the hit probability rises, why we might use the deflection concept for those cases inside the acceleration zone of the projectiles. In addition, deflection processes before the encounter are amplified due to the flyby. The best location for an impact with the highest expected value of velocity change is at 0.3% of the length of the acceleration zone, yet a single projectile seems still not sufficient.

As a projectile impacts on a near-Earth object, a crater forms due to the huge kinetic energy. Hence, we presume a fragmentation of bodies smaller than a few tens of meters. For larger NEOs, which survive the impact, material is ejected into space, leading to a momentum multiplication and therefore to a more efficient deflection. Interpolation of the data suggests a boost by a factor of up to a few  $10^4$ . However, the momentum multiplication is highly dependent on the porosity and in particular rubble piles or highly porous objects might be unaffected.

As the projectile travels through the interplanetary space, collisions with interplanetary dust and micrometeoroids occur, yet the deceleration of the projectiles by this matter

---

can be neglected. Collisions with a few  $10^3 \mu\text{m}$  large or  $10^{-5}$  to  $10^{-4}$  g massive particles can happen for a travel distance of 1 AU. Besides, smaller and less-massive dust collides numerous times, why the projectiles have to sustain such collisions.

The best location for the light beamers would be the equator region, as here a larger fraction of the ecliptic can be illuminated during a full rotation of Earth than at any other latitude. Though, the maximum alignment angle of the laser to the zenith is a very important factor, influencing the accessible parts of the ecliptic more than the location of the laser. The different tangential speeds of Earth at different latitudes due to the rotation have to be taken into account, too.

Deflection simulations without momentum multiplication showed, that there is roughly a 30% chance of deflecting a near-Earth asteroid with a size between 50m and 500 m for a shot rate of one projectile per day, a deflection start 10 years before the impact on Earth and an almost perfect hit ratio. If real potentially hazardous objects are used for the simulation with the same specifications, only roughly 0.03% were successfully deflected. Those numbers are pessimistic, yet foreseeable due to the analytic study of the deflection method. In addition, we see higher success for bodies with large inclinations, large semi-major axes and large eccentricities. As expected smaller NEO sizes and as a consequence lower masses are easier to deflect. The simulation confirms that roughly  $10^3$  times better targeting accuracy leads to no further deflection success, since almost every projectile already impacts on the object.

Future work has to focus on the impact effects on the near-Earth objects and their ejecta. Even though the pure linear momentum transfer is too small to handle km-sized objects, the huge released kinetic energy and the resulting momentum multiplication could make this deflection method attractive. Here, especially the newest research about porosity must be taken into account. Same is true for fragmentation or no fragmentation of the body, as this makes a tremendous difference for planetary defense. Further investigation should be done for the dust impacts on the projectiles. Here, a size or mass limit for destructive micrometeoroids must be found and checked, if projectiles can even reach their targets and not being destroyed before. A next step after the study of the beamer locations would be investigations about the gateway orbits of the projectiles around Earth, before they get accelerated. Apart from that, one has to look out for new publications and the newest technological developments of Breakthrough Starshot and if necessary rechecking the deflection success.

Further analysis of the simulation data can be done as for example different shot modes

can be studied. New data sets, including the gravity of Earth and other planets can be easily generated to consider flybys and the associated orbital changes, which lower the required velocity change for deflection. If theoretical studies confirm the expected huge momentum multiplication, this factor and the uncertainty in position can be implemented too, to get even more realistic results.

As one can see, there are still some open questions which must be resolved to figure out if this deflection method could be used to save the human civilization someday.

# Appendix A

## Details of MAIDS code

### Orbit determination

The specific orbit elements, described in AppB, are read in from an external file into the simulation. The computation begins with all NEOs and Earth at the same place, the home position, why only the 3D-velocities  $\mathbf{v}$  of the objects must be computed. They can be derived by geometrical considerations and from Walter (2012) with

$$\tan i = \frac{v_z}{\sqrt{(v_x^2 + v_y^2)}} \quad , \quad (\text{A.1})$$

$$\mathbf{L} = \mathbf{r} \times \mathbf{v} \quad , \quad (\text{A.2})$$

$$v^2 = GM_\odot \left( \frac{2}{r} - \frac{1}{a} \right) \quad , \quad (\text{A.3})$$

$$L^2 = aGM_\odot (1 - e^2) \quad . \quad (\text{A.4})$$

Here,  $\mathbf{L}$  is the angular momentum,  $a$  is the semi-major axis,  $e$  the eccentricity,  $i$  the inclination,  $M_\odot$  the mass of the Sun,  $\mathbf{r}$  the distance to the Sun and  $G$  the gravitational constant.

With the home position at  $X = 1$ ,  $Y = 0$ ,  $Z = 0$ , as we use AU as length unit, and

some rearranging, one obtains

$$v_x = \sqrt{GM_\odot \left(2 - \frac{1}{a}\right) - \left(\frac{(1-e^2)aGM_\odot}{1 + \tan^2 i} \tan^2 i\right)} \quad , \quad (\text{A.5})$$

$$v_y = \sqrt{\frac{(1-e^2)aGM_\odot}{1 + \tan^2 i}} \quad , \quad (\text{A.6})$$

$$v_z = \sqrt{\frac{(1-e^2)aGM_\odot}{1 + \tan^2 i} \tan^2 i} \quad (\text{A.7})$$

as starting conditions for the home position.

For every set of  $a$ ,  $e$  and  $i$ , two different orbits can be set up, as there are two valid arguments of periapsis  $\omega$ . Therefore the number of input orbits get doubled.

## Backward integration

The code is based on the Leapfrog integrator for the time integration, where the 3D-position  $\mathbf{x}$  and velocity  $\mathbf{v}$  of the collisionless objects are computed for every timestep  $\Delta t$ :

$$\mathbf{v}_{k+0.5} = \mathbf{v}_k + \frac{1}{2} \dot{\mathbf{v}}_k \Delta t \quad , \quad (\text{A.8})$$

$$\mathbf{x}_{k+1} = \mathbf{x}_k + \mathbf{v}_{k+0.5} \Delta t \quad , \quad (\text{A.9})$$

$$\mathbf{v}_{k+1} = \mathbf{v}_{k+0.5} + \frac{1}{2} \dot{\mathbf{v}}_{k+1} \Delta t \quad . \quad (\text{A.10})$$

This is similar to the work of Dehnen and Read (2011) with  $\dot{\mathbf{v}}$  as acceleration. The indices refer to the arbitrary time  $t_k$  and  $t_{k+1} = t_k + \Delta t$ . The index  $k + 0.5$  corresponds to an intermediate step during the computation of a full timestep. This time integration method is very easy, but energy is conserved in a longterm. Since we use a fixed timestep of  $\Delta t = 4 \text{ h}$ , the simulation is time reversible, too.

For computing the acceleration between the object  $i$  and  $n$  other bodies, we use the Newtonian gravitational force as described in (Benacquista and Romano, 2018):

$$\dot{\mathbf{v}}_{ki} m_i = \mathbf{F}_{ki} = G m_i \sum_{\substack{j=1 \\ j \neq i}}^n m_j \frac{\mathbf{r}_{kj} - \mathbf{r}_{ki}}{\|\mathbf{r}_{kj} - \mathbf{r}_{ki}\|^3} \quad . \quad (\text{A.11})$$

Here,  $\mathbf{r}$  is the position vector of a body and  $m$  its mass. However, for simplification reasons we only consider the gravity of the Sun with a fixed position at  $X = 0$  AU,  $Y = 0$  AU,  $Z = 0$  AU to the moving Earth and NEOs. This means, no orbit changes by close approaches are taken into account. The backward integration determines the actual starting position of the NEOs and Earth for the forward integration. This procedure is done to assure the impact of every object on Earth during the forward integration within the simulation timeframe.

## Turnaround

The turnaround command mirrors the velocities  $\mathbf{v}$  of the objects to determine the actual starting velocities. For the backward integration, only one object per orbit was computed to minimize the computation time. Hence, during the turnaround, the actual impactor population with different physical properties, as described in App.B, is generated.

## Forward integration

The forward integration is also done by the Leapfrog integrator and is split into two steps. At first a set of undeflected NEOs is simulated to ensure that all objects impact on Earth and no numerical inaccuracies disturb the simulation. The second step is the simulation of the deflected NEOs. Here three cases are studied: *acceleration firing*, *deceleration firing* and *independent firing*. The former only shoots a projectile if the NEO is moving away from Earth, the second case only shoots for approaching objects and the latter is independent of the NEO movement and fires always. A check, comparing the shot frequency with the simulation time  $t$ , reveals if projectiles are fired off. If yes, the impact probability

$$P = \left( \chi \frac{d_{\text{NEO}}}{2r_{\text{PC}}} \frac{D_{\text{PC}}}{D_{\text{NEO}}} \right)^2, \quad (\text{A.12})$$

described at Eq.(2.35), is checked against a random number for every spherically approximated object separately. Here, no uncertainties in the location data of the NEOs are assumed. If a projectile by chance hit a NEO, an additional velocity change is added to Eq.(A.10):

$$\mathbf{v}_{k+1} = \mathbf{v}_{k+0.5} + \frac{1}{2} \dot{\mathbf{v}}_k \Delta t + f \Delta \mathbf{v} \quad (\text{A.13})$$

with the additional velocity change

$$\Delta \mathbf{v} = \frac{\gamma(v_p)m_p \mathbf{v}_p}{m_{\text{NEO}}} . \quad (\text{A.14})$$

The derivation of the achieved velocity change is described at Eq.(2.15) as a perfectly inelastic collision without any momentum multiplication. No travel of the projectiles through space is considered, why the velocity change is added instantaneous, no perturbation on the projectiles are included and interplanetary dust, which might somehow effect the projectiles, is excluded.  $f$  is the fraction of velocity change by the projectile and is given by

$$f = \begin{cases} 0, & \text{if } D_{\text{NEO}} \leq 60 \times 10^3 \text{ km} \\ \frac{D_{\text{NEO}} - 60 \times 10^3 \text{ km}}{0.15 \text{ AU} - 60 \times 10^3 \text{ km}}, & \text{if } 60 \times 10^3 \text{ km} < D_{\text{NEO}} \leq 0.15 \text{ AU} \\ 1, & \text{otherwise} \end{cases} . \quad (\text{A.15})$$

With this case differentiation, the acceleration zone up to 0.15 AU and the initial position at  $60 \times 10^3$  km of the projectiles are considered, too.

The masses of the NEOs are kept constant during the full simulation, why we do not consider mass loss by ejecta or fragmentation.

For every timestep, the distance to Earth is checked, which is needed to determine the hit probability. We use  $\Delta t_{\text{detail}} = 2 \text{ min} \ll \Delta t$  two days before the scheduled impacts. This detail zone of higher accuracy is implemented to not miss any impact. We check for impacts only in the detail zone, since there are no notable perturbations on the NEOs in the simulation, as by other planets, why there can be impactors in an integer resonance with Earth, leading to premature impacts. Those unscheduled impacts should be excluded to enable the same deflection time for every object. If the distance from the center of Earth to the NEO  $D_{\text{NEO}}$  gets smaller than an additionally extended Earth radius

$$b_{\oplus, \text{check}} = \sqrt{b_{\oplus}^2 + 0.5 \left( 40 \frac{\text{km}}{\text{s}} \Delta t_{\text{detail}} \right)^2} , \quad (\text{A.16})$$

an impact on Earth is recorded.  $b_{\oplus}$  is the effective radius of Earth, which considers the gravity of Earth. This additionally extension is done to avoid false negatives by wrong timing. With this radius enlargement, every real impact on Earth is recorded, yet this leads to false positives. Therefore the simulation detects more impacts than there would be and

gives a worst case scenario. In addition, the simulation is extended by two days to capture late arriving impactors. The detail zone was considered for the backward integration, too.

## **Error analysis**

During the computation of the unperturbed NEOs the minimum distance of every impactor to Earth is computed. Due to the same home position, a perfect simulation would output zero as distance for all objects at the point of time of the scheduled impacts. However, numerical errors lead to a value  $> 0$ . We check for impacts of the deflected NEOs with two additional Earth radii, one with the minimum distance added and one with the minimum distance subtracted. This leads to an upper and lower value of impacts, caused by the numerical integration error.



# Appendix B

## Details of setup and impactor populations

### Orbit properties

We use two different sets for the orbit properties. The synthetic impactors by Chesley and Spahr (2004) is a large dataset of typical Earth impacting asteroids. The orbital parameters are based on the work of Bottke et al. (2000) and the corresponding NEAs. There are 21272 different orbits available, which we all use.

The second dataset is obtained from ESA NEO Coordination Centre (2018). They provide a list of all PHA orbits, inclusively their absolute magnitude  $H$ . As PHAs do not necessarily impact Earth, but have close approaches, their eccentricity  $e$  is slightly modified to ensure an impact. In the beginning of July 2018, 1908 PHAs were listed.

### Physical properties

Similar to Stuart and Binzel (2004), we differentiate between two types of NEOs, the dark group including C, D and X complexes with  $\rho_{\text{NEO,dark}} = 1400 \frac{\text{kg}}{\text{m}^3}$  and the bright group combining A, O, Q, R, S, U, V complexes with  $\rho_{\text{NEO,bright}} = 2700 \frac{\text{kg}}{\text{m}^3}$ . The densities are randomly picked with a dark-to-bright ratio of 1.6.

The  $H$ -distribution for the synthetic impactors is realized with the cumulative  $H$ -distribution of (Stuart and Binzel, 2004):

$$N(< H) = 10^{-3.88+0.39H} \quad , \quad (\text{B.1})$$

where  $N$  is the cumulative number of the NEOs with the absolute magnitude  $H$ . The relation is valid up to  $H = 22.5$ , which corresponds roughly to 180 m objects. Nevertheless, Stuart and Binzel (2004) extrapolates the distribution to higher magnitudes up to  $H = 25$ . We do the same as we want to simulate sizes of  $50 \text{ m} \leq d_{\text{NEO}} \leq 500 \text{ m}$ . Due to the distribution function, the majority of objects are very small and only few large NEOs are generated. The  $H$  values for the PHA setup are obtained from the ESA NEO Coordination Centre (2018) database.

The relation between the absolute magnitude  $H$  and the diameter of the objects, which is needed for both orbit datasets, is given by (Harris, 1998)

$$d_{\text{NEO}} = 10^{-\frac{H}{5}} \frac{1329 \times 10^3}{\sqrt{\mathcal{A}_v}} \quad (\text{B.2})$$

with the visual albedo  $\mathcal{A}_v$ . According to Stuart and Binzel (2004), the visual albedo depends on the taxonomic type and a typical value for a C-type albedo is  $\mathcal{A}_{v,\text{dark}} = 0.047$  and for a S-type albedo is  $\mathcal{A}_{v,\text{bright}} = 0.15$ . Together with the density and diameter, the mass of the spherically approximated NEOs gets determined with

$$m_{\text{NEO}} = \frac{4}{3} \pi \left( \frac{d_{\text{NEO}}}{2} \right)^3 \rho_{\text{NEO}} \quad . \quad (\text{B.3})$$

# Bibliography

- Abe, S. (2008). Meteoroids and meteor observations and connection to parent bodies. In Mann, I., Nakamura, A., and Mukai, T., editors, *Small Bodies in Planetary Systems*, pages 129–166. Springer, Berlin, Heidelberg.
- Anglada-Escudé, G., Amado, P. J., Barnes, J., Berdiñas, Z. M., Butler, R. P., Coleman, G. A., de La Cueva, I., Dreizler, S., Endl, M., Giesers, B., et al. (2016). A terrestrial planet candidate in a temperate orbit around proxima centauri. *Nature*, 536(7617):437–440.
- Asphaug, E. (2004). Interior structures for asteroids and cometary nuclei. In Belton, M. J. S., Morgan, T. H., Samarasinha, N. H., and Yeomans, D. K., editors, *Mitigation of Hazardous Comets and Asteroids*, pages 66–103. Cambridge University Press, Cambridge.
- AstDyS-2 (2013). [hamilton.dm.unipi.it/astdys/](http://hamilton.dm.unipi.it/astdys/).
- Badescu, V. (2013). *Asteroids: Prospective energy and material resources*. Springer Science & Business Media, Berlin, Heidelberg.
- Belton, M. J. S., Morgan, T. H., Samarasinha, N. H., and Yeomans, D. K. (2004). *Mitigation of Hazardous Comets and Asteroids*. Cambridge University Press, Cambridge.
- Benacquista, M. J. and Romano, J. D. (2018). *Classical Mechanics*. Springer, Berlin, Heidelberg.
- Bobrowsky, P. and Rickman, H. (2007). Springer Science & Business Media, Berlin, Heidelberg.
- Bombardelli, C. and Peláez, J. (2011). Ion beam shepherd for asteroid deflection. *Journal of Guidance, Control, and Dynamics*, 34(4):1270–1272.

- Bottke, W. F., Jedicke, R., Morbidelli, A., Petit, J.-M., and Gladman, B. (2000). Understanding the distribution of near-earth asteroids. *Science*, 288(5474):2190–2194.
- Bottke, W. F., Morbidelli, A., and Jedicke, R. (2004). Recent progress in interpreting the nature of the near-earth object population. In Belton, M. J. S., Morgan, T. H., Samarasinha, N. H., and Yeomans, D. K., editors, *Mitigation of Hazardous Comets and Asteroids*, pages 1–21. Cambridge University Press.
- Brashears, T., Lubin, P., Hughes, G. B., McDonough, K., Arias, S., Lang, A., Motta, C., Meinhold, P., Batliner, P., Griswold, J., et al. (2015). Directed energy interstellar propulsion of wafersats. In *SPIE Optical Engineering + Applications, Nanophotonics and Macrophotonics for Space Environments IX*, volume 9616, page 961609, San Diego, California, USA.
- Brashears, T., Lubin, P., Rupert, N., Stanton, E., Mehta, A., Knowles, P., and Hughes, G. B. (2016). Building the future of wafersat spacecraft for relativistic spacecraft. In *SPIE Optical Engineering + Applications, Planetary Defense and Space Environment Applications*, volume 9981, page 998104, San Diego, California, USA.
- Breakthrough Initiative (2018). <https://breakthroughinitiatives.org/Initiative/3>.
- Britt, D. T., Yeomans, D. K., Housen, K., and Consolmagno, G. (2003). Asteroid density, porosity, and structure. In Bottke, W. F., Cellino, A., and Paolicchi, P., editors, *Asteroids III*, pages 485–500. University of Arizona Press.
- Bronstein, I. N., Hromkovic, J., Luderer, B., Schwarz, H.-R., Blath, J., Schied, A., Dempe, S., Wanka, G., and Gottwald, S. (2012). *Taschenbuch der Mathematik*. Springer, Berlin, Heidelberg.
- Burbine, T. H. (2002). Asteroids: Their composition and impact threat. *Bulletin of the Czech Geological Survey*, 77(4):243–252.
- Burkert, A. (2017). private communication.
- Bus, S. J. and Binzel, R. P. (2002). Phase ii of the small main-belt asteroid spectroscopic survey: A feature-based taxonomy. *Icarus*, 158(1):146–177.
- Carusi, A., Valsecchi, G. B., D’Abramo, G., and Boattini, A. (2002). Deflecting neos in route of collision with the earth. *Icarus*, 159(2):417–422.

- Chapman, C. R. (2007). The asteroid impact hazard and interdisciplinary issues. In Bobrowsky, P. and Rickman, H., editors, *Comet/Asteroid Impacts and Human Society*, pages 145–162. Springer Science & Business Media, Berlin, Heidelberg.
- Cheng, A. F., Rivkin, A. S., Michel, P., Atchison, J., Barnouin, O., Benner, L., Chabot, N. L., Ernst, C., Fahnestock, E. G., Kueppers, M., et al. (2018). Aida dart asteroid deflection test: Planetary defense and science objectives. *Planetary and Space Science*, 157:104–115.
- Chesley, S. R. and Spahr, T. B. (2004). Earth impactors: orbital characteristics and warning times. In Belton, M. J. S., Morgan, T. H., Samarasinha, N. H., and Yeomans, D. K., editors, *Mitigation of Hazardous Comets and Asteroids*, pages 22–37. Cambridge University Press, Cambridge.
- Collins, G. S., Melosh, H. J., and Marcus, R. A. (2005). Earth impact effects program: A web-based computer program for calculating the regional environmental consequences of a meteoroid impact on earth. *Meteoritics & Planetary Science*, 40(6):817–840.
- Dehnen, W. and Read, J. I. (2011). N-body simulations of gravitational dynamics. *The European Physical Journal Plus*, 126(5):55–82.
- DeMeo, F. E., Binzel, R. P., Slivan, S. M., and Bus, S. J. (2009). An extension of the bus asteroid taxonomy into the near-infrared. *Icarus*, 202(1):160–180.
- Desmars, J., Bancelin, D., Hestroffer, D., and Thuillot, W. (2013). Statistical and numerical study of asteroid orbital uncertainty. *Astronomy & Astrophysics*, 554:A32.
- ESA NEO Coordination Centre (2018). <http://neo.ssa.esa.int/>.
- Fraser, S. D. (2013). Electric power system options for robotic miners. In Badescu, V., editor, *Asteroids: Prospective energy and material resources*, pages 247–270. Springer Science & Business Media, Berlin, Heidelberg.
- Genda, H. (2016). Origin of earths oceans: an assessment of the total amount, history and supply of water. *Geochemical Journal*, 50(1):27–42.
- Ghisellini, G. (2013). *Radiative processes in high energy astrophysics*. Springer.
- Grandl, W. and Bazso, A. (2013). Near earth asteroids—prospection, orbit modification, mining and habitation. In Badescu, V., editor, *Asteroids: Prospective energy and*

- material resources*, pages 415–438. Springer Science & Business Media, Berlin, Heidelberg.
- Grieve, R. A. and Kring, D. A. (2007). The geologic record of destructive impact events on earth. In Bobrowsky, P. and Rickman, H., editors, *Comet/Asteroid Impacts and Human Society*, pages 3–24. Springer Science & Business Media, Berlin, Heidelberg.
- Gritzner, C. (1997). Human casualties in impact events. *WGN, Journal of the International Meteor Organization*, 25:222–226.
- Gritzner, C. and Fasoulas, S. (2001). Katastrophen durch Einschläge von Asteroiden und Kometen. In *Zweites Forum Katastrophenvorsorge*, pages 43–52, Leipzig, Germany.
- Gritzner, C. and Kahle, R. (2004). Mitigation technologies and their requirements. In Belton, M. J. S., Morgan, T. H., Samarasinha, N. H., and Yeomans, D. K., editors, *Mitigation of Hazardous Comets and Asteroids*, pages 167–200. Cambridge University Press.
- Grün, E., Zook, H., Fechtig, H., and Giese, R. (1985). Collisional balance of the meteoritic complex. *Icarus*, 62(2):244–272.
- Harris, A. W. (1998). A thermal model for near-earth asteroids. *Icarus*, 131(2):291–301.
- Holsapple, K. A. (1993). The scaling of impact processes in planetary sciences. *Annual review of earth and planetary sciences*, 21(1):333–373.
- Housen, K. R. and Holsapple, K. A. (2011). Ejecta from impact craters. *Icarus*, 211(1):856–875.
- Housen, K. R. and Holsapple, K. A. (2012). Deflecting asteroids by impacts: What is beta. In *43rd Lunar and Planetary Science Conference*, pages 2539–2540.
- Jones, N. (2016). First flight for tiny satellites: launch of ‘chipsat’ probes in july will test a new way to explore the solar system—and beyond. *Nature*, 534(7605):15–17.
- Jutzi, M. and Michel, P. (2014). Hypervelocity impacts on asteroids and momentum transfer i. numerical simulations using porous targets. *Icarus*, 229:247–253.
- LeitOn GmbH (2018). <https://www.leiton.de>.

- Levison, H. F., Bottke, W. F., Gounelle, M., Morbidelli, A., Nesvorný, D., and Tsiganis, K. (2009). Contamination of the asteroid belt by primordial trans-neptunian objects. *Nature*, 460(7253):364–366.
- Ley, W., Wittmann, K., and Hallmann, W. (2009). *Handbook of space technology*, volume 22. John Wiley & Sons.
- Longo, G. (2007). The tunguska event. In Bobrowsky, P. and Rickman, H., editors, *Comet/Asteroid Impacts and Human Society*, pages 303–330. Springer Science & Business Media, Berlin, Heidelberg.
- Lubin, P. (2016). A roadmap to interstellar flight. *arXiv preprint*.
- Lyne, J. E. (1995). Origin of the tunguska event. *Nature*.
- Mainzer, A., Grav, T., Bauer, J., Masiero, J., McMillan, R. S., Cutri, R. M., Walker, R., Wright, E., Eisenhardt, P., Tholen, D. J., Spahr, T., Jedicke, R., Denneau, L., DeBaun, E., Elsbury, D., Gautier, T., Gomillion, S., Hand, E., Mo, W., Watkins, J., Wilkins, A., Bryngelson, G. L., Molina, A. D. P., Desai, S., Camus, M. G., Hidalgo, S. L., Konstantopoulos, I., Larsen, J. A., Maleszewski, C., Malkan, M. A., Mauduit, J.-C., Mullan, B. L., Olszewski, E. W., Pforr, J., Saro, A., Scotti, J. V., and Wasserman, L. H. (2011). Neowise observations of near-earth objects: Preliminary results. *The Astrophysical Journal*, 743(2):156–172.
- Mainzer, A., Grav, T., Masiero, J., Bauer, J., McMillan, R., Giorgini, J., Spahr, T., Cutri, R., Tholen, D., Jedicke, R., et al. (2012). Characterizing subpopulations within the near-earth objects with neowise: Preliminary results. *The Astrophysical Journal*, 752(2):110–125.
- Manchester, Z., Peck, M., and Filo, A. (2013). Kicksat: A crowd-funded mission to demonstrate the worlds smallest spacecraft. In *27th Annual AIAA/USU Conference on Small Satellites*, Logan, Utah, USA.
- Mann, I., Nakamura, A., and Mukai, T. (2009). *Small Bodies in Planetary Systems*. Springer, Berlin, Heidelberg.
- Meech, K. J., Weryk, R., Micheli, M., Kleyana, J. T., Hainaut, O. R., Jedicke, R., Wainscoat, R. J., Chambers, K. C., Keane, J. V., Petric, A., et al. (2017). A brief visit from a red and extremely elongated interstellar asteroid. *Nature*, 552(7685):378–381.

- Melosh, H. J. (2007). Physical effects of comet and asteroid impacts: beyond the crater rim. In Bobrowsky, P. and Rickman, H., editors, *Comet/Asteroid Impacts and Human Society*, pages 211–224. Springer, Berlin, Heidelberg.
- Melosh, H. J. and Collins, G. (2005). Planetary science: Meteor crater formed by low-velocity impact. *Nature*, 434(7030):157.
- Meyer, C., Fritz, J., Misgaiski, M., Stoeffler, D., Artemieva, N. A., Hornemann, U., Moeller, R., de Vera, J.-P., Cockell, C., Horneck, G., et al. (2011). Shock experiments in support of the lithopanspermia theory: The influence of host rock composition, temperature, and shock pressure on the survival rate of endolithic and epilithic microorganisms. *Meteoritics & Planetary Science*, 46(5):701–718.
- Nolting, W. (2017). *Theoretical Physics 5*. Springer.
- Onofri, S., de la Torre, R., de Vera, J.-P., Ott, S., Zucconi, L., Selbmann, L., Scalzi, G., Venkateswaran, K. J., Rabbow, E., Sánchez Iñigo, F. J., et al. (2012). Survival of rock-colonizing organisms after 1.5 years in outer space. *Astrobiology*, 12(5):508–516.
- Ostro, S. J. and Giorgini, J. D. (2004). The role of radar in predicting and preventing asteroid and comet collisions with earth. In Belton, M. J. S., Morgan, T. H., Samarasinha, N. H., and Yeomans, D. K., editors, *Mitigation of Hazardous Comets and Asteroids*, pages 38–65. Cambridge University Press, Cambridge.
- Oxford Dictionaries (2018). <https://en.oxforddictionaries.com/>.
- Parkin, K. L. G. (2018). The breakthrough starshot system model. *arXiv preprint*.
- Perna, D., Barucci, M., Drube, L., Falke, A., Fulchignoni, M., Harris, A., and Kanuchova, Z. (2015). A global response roadmap to the asteroid impact threat: the neoshield perspective. *Planetary and Space Science*, 118:311–317.
- Perna, D., Dotto, E., Ieva, S., Barucci, M. A., Bernardi, F., Fornasier, S., Luise, F. D., Perozzi, E., Rossi, A., Epifani, E. M., Micheli, M., and Deshapriya, J. D. P. (2016). Grasping the nature of potentially hazardous asteroids. *The Astronomical Journal*, 151(1):11–24.
- Pierazzo, E. and Artemieva, N. (2012). Local and global environmental effects of impacts on earth. *Elements*, 8(1):55–60.

- Planetary and Space Science Centre - University of New Brunswick (2018). <http://www.passc.net/EarthImpactDatabase/index.html>.
- Popova, O. P., Jenniskens, P., Emelyanenko, V., Kartashova, A., Biryukov, E., Khaibrakhmanov, S., Shuvalov, V., Rybnov, Y., Dudorov, A., Grokhovsky, V. I., et al. (2013). Chelyabinsk airburst, damage assessment, meteorite recovery, and characterization. *Science*, 342(6162):1069–1073.
- Richardson, J. E., Melosh, H. J., Lisse, C. M., and Carcich, B. (2007). A ballistics analysis of the deep impact ejecta plume: Determining comet tempel 1’s gravity, mass, and density. *Icarus*, 190(2):357–390.
- Sanchez, P., Colombo, C., Vasile, M., and Radice, G. (2009). Multicriteria comparison among several mitigation strategies for dangerous near-earth objects. *Journal of Guidance, Control, and Dynamics*, 32(1):121–142.
- SIMBAD Astronomical Database (2018). <http://simbad.u-strasbg.fr/simbad/>.
- Stöffler, D., Artemieva, N. A., and Pierazzo, E. (2002). Modeling the ries-steinheim impact event and the formation of the moldavite strewn field. *Meteoritics and Planetary Science*, 37:1893–1907.
- Stuart, J. S. and Binzel, R. P. (2004). Bias-corrected population, size distribution, and impact hazard for the near-earth objects. *Icarus*, 170(2):295–311.
- Tagesschau (2017). Bergbau im Weltraum – Mehr Space für Luxemburg. <https://www.tagesschau.de/ausland/luxemburg-weltraum-101.html>.
- Takeuchi, T. (2008). From protoplanetary disks to planetary disks: gas dispersal and dust growth. In Mann, I., Nakamura, A., and Mukai, T., editors, *Small Bodies in Planetary Systems*, pages 1–35. Springer, Berlin, Heidelberg.
- Tepfer, D., Zalar, A., and Leach, S. (2012). Survival of plant seeds, their uv screens, and nptii dna for 18 months outside the international space station. *Astrobiology*, 12(5):517–528.
- Valsecchi, G., Milani, A., Gronchi, G. F., and Chesley, S. (2003). Resonant returns to close approaches: Analytical theory. *Astronomy & Astrophysics*, 408(3):1179–1196.
- Walter, U. (2012). *Astronautics: the physics of space flight*. John Wiley & Sons.

- Wyatt, M. C. (2008). Dynamics of small bodies in planetary systems. In Mann, I., Nakamura, A., and Mukai, T., editors, *Small Bodies in Planetary Systems*, pages 37–70. Springer, Berlin, Heidelberg.
- Yeomans, D. K. (2016). *Near-Earth objects: finding them before they find us*. Princeton University Press, Princeton.
- Yeomans, D. K., Bhaskaran, S., Broschart, S., Chesley, S., Chodas, P., Sweetser, T., and Schweickart, R. (2009). Deflecting a hazardous near-earth object. In *1st IAA Planetary Defense Conference: Protecting Earth from Asteroids*, Granada, Spain.

# List of figures and tables

## Figures

1.1	Small bodies term clarification . . . . .	4
1.2	NEO orbit classes . . . . .	6
2.1	Artist illustration of a nanocraft . . . . .	18
2.2	Artist illustration of the KickSat . . . . .	18
2.3	Encounter and impact velocities of PHAs and impactor population . . . . .	22
2.4	Orbital elements of impactor population . . . . .	23
2.5	Required velocity change of NEO for successful deflection . . . . .	25
2.6	Single event achieved velocity change of NEO . . . . .	28
2.7	Deflection time for single event deflection . . . . .	29
2.8	Evolution of required velocity change by continuous deflection . . . . .	31
2.9	Deflection starting time for continuous deflection . . . . .	34
2.10	Deflection starting time for deflection with maximum shot number . . . . .	36
2.11	Deflection starting time comparison between continuous and single event model . . . . .	37
2.12	Required targeting angle for hitting NEOs . . . . .	40
2.13	Impact probability of projectiles . . . . .	40
2.14	Required targeting angle amplification factor for 100% impact chance . . . . .	42
2.15	Probability of hitting a NEO with 50% chance at least once . . . . .	42
2.16	Spatial uncertainty of NEOs and projectiles . . . . .	43
2.17	Trigonometric setup for targeting angle improvement . . . . .	44
2.18	Normalized targeting angle improvement . . . . .	45
2.19	Gravitational perturbation of projectiles starting outside the acceleration zone	47
2.20	Gravitational perturbation of projectiles starting inside the acceleration zone	48
2.21	Deflection of a 50 m NEO inside the acceleration zone . . . . .	51

2.22	Deflection of a 100 m NEO inside the acceleration zone . . . . .	52
2.23	Transient crater diameter by projectiles as function of bulk density . . . . .	56
2.24	Transient crater diameter on 9P/Tempel 1 as function of bulk density . . . . .	56
2.25	Transient crater diameter by projectiles as function of NEO diameter . . . . .	58
2.26	Momentum multiplication factor for projectiles . . . . .	60
2.27	Velocity evolution by interaction with interplanetary dust . . . . .	62
2.28	Mean free path of projectile in interplanetary space . . . . .	63
2.29	Light beamers at equator . . . . .	65
2.30	Light beamers at high latitude . . . . .	66
3.1	Deflection simulations of synthetic impactors . . . . .	72
3.2	Deflection simulations of ESA's PHA impactors . . . . .	73
3.3	Detailed results of a 25 year simulation with one shot per day . . . . .	75

## Tables

1.1	Size, number and impact timescales of NEOs . . . . .	9
1.2	Damage by NEO impacts . . . . .	11
2.1	Specifications of projectiles . . . . .	20
2.2	Specifications of Breakthrough Starshot . . . . .	20
2.3	Required velocity change 25 years before impact . . . . .	24
2.4	Target properties for cratering computation . . . . .	55
2.5	Target properties for momentum multiplication factor computation . . . . .	59

# Abbreviations

<b>App</b>	Appendix
<b>AIDA</b>	Asteroid Impact & Deflection Assessment
<b>CCD</b>	Charge-coupled device
<b>DART</b>	Double Asteroid Redirection Test
<b>DFG</b>	German Research Foundation Deutsche Forschungsgemeinschaft
<b>Eq</b>	Equation
<b>ESA</b>	European Space Agency
<b>Fig</b>	Figure
<b>HEOS</b>	Highly Eccentric Orbit Satellite
<b>IEO</b>	Interior-to-Earth object
<b>ISO</b>	Interstellar object
<b>MIAPP</b>	Munich Institute for Astro- and Particle Physics
<b>MOID</b>	Minimum orbit intersection distance
<b>NASA</b>	National Aeronautics and Space Administration
<b>NEA</b>	Near-Earth asteroid
<b>near-IR</b>	near-infrared
<b>NEO</b>	Near-Earth object

<b>PHA</b>	Potential hazardous asteroid
<b>Sec</b>	Section
<b>SI</b>	International System of Units
<b>SOI</b>	Sphere of influence
<b>SSA</b>	Space Situational Awareness segment of ESA
<b>Tab</b>	Table
<b>WISE</b>	Wide-Field Infrared Survey Explorer

# Nomenclature

## Physical quantities

$\alpha$	Right ascension
$\alpha_{\text{tar,max}}$	Maximum targeting angle
$\alpha_{\text{tar}}$	Targeting angle
$\bar{Y}$	Effective material strength
$\beta$	Momentum multiplication factor
$\chi$	Amplification factor of targeting angle
$\Delta t$	Timestep
$\Delta U$	Change of internal energy
$\Delta v$	Achieved velocity change
$\Delta v_{\text{r}}$	Required velocity change for deflection
$\delta$	Declination
$\dot{v}$	Acceleration
$\lambda$	Mean free path
$\mathcal{A}_{\text{v}}$	Visual albedo
$\mathcal{F}$	Cumulative interplanetary meteoroid flux
$\mathcal{N}$	Cumulative spatial density

---

$\mu$	Material property
$\omega$	Argument of periapsis
$\Phi$	Latitude
$\rho$	Bulk density
$\Sigma$	Areal density
$\sigma$	Cross section
$\tau$	Time scale
$\mathbf{L}$	Angular momentum
$\mathbf{x}$	Position
$\theta$	Angle between geometric velocity of NEO and heliocentric velocity of Earth
$\varphi$	Targeting angle improvement
$\zeta$	Maximum possible angle deviation of laser to the zenith
$A$	Area
$a$	Semi-major axis
$b_{\oplus}$	Effective radius of Earth
$C$	Material proportionality constant
$D$	Distance
$d$	Diameter
$E$	Energy
$e$	Eccentricity
$F$	Force
$g$	Force of gravity

---

$H$	Absolute magnitude
$h$	Altitude
$i$	Inclination
$k$	Number of impacts
$K_1$	Material property
$m$	Mass
$N$	Cumulative number
$n$	Total number of shot projectiles
$P$	Probability
$p$	Linear momentum
$Q$	Aphelion
$q$	Perihelion
$r$	Radius
$s$	Shot frequency
$T$	Orbital period
$t$	Time before NEO impact on Earth
$t_{\text{def},1}$	Deflection starting time for longer deflection process
$t_{\text{def}}$	Deflection time
$V$	Transient crater volume
$v$	Velocity
$v_{\infty}$	Unperturbed encounter velocity of the NEO on Earth
$v_{\text{esc}}$	Escape velocity
$v_{\text{tan}}$	Tangential speed

$X$	X-coordinate
$Y$	Y-coordinate
$Z$	Z-coordinate
$z$	Thickness or depth
MOID	Minimum orbit intersection distance

### Physical units and constants

$\text{AU} = 1.496 \times 10^{11} \text{ m}$	Astronomical unit
$\text{d} = 8.64 \times 10^4 \text{ s}$	Day
$\text{ls} = 2.9979 \times 10^8 \text{ m}$	Light-second
$\text{ly} = 9.4542 \times 10^{25} \text{ m}$	Light-year
$\text{mo} \approx 2.59 \times 10^6 \text{ s}$	Month
$\text{Myr} = 10^6 \text{ yr}$	Million years
$\text{wk} \approx 6.05 \times 10^5 \text{ s}$	Week
$\text{yr} \approx 3.15 \times 10^7 \text{ s}$	Year
$c = 2.9979 \times 10^8 \frac{\text{m}}{\text{s}}$	Speed of light in free space
$g_{\oplus} = 9.807 \frac{\text{m}}{\text{s}^2}$	Standard acceleration due to gravity
$M_{\oplus} = 6.0 \times 10^{24} \text{ kg}$	Mass of Earth
$M_{\text{oceans}} \approx 1.4 \times 10^{21} \text{ kg}$	Mass of Earth's oceans
$M_{\odot} = 1.989 \times 10^{30} \text{ kg}$	Mass of Sun
$\text{pc} = 3.086 \times 10^{16}$	Parsec
$R_{\oplus} = 6.3781 \times 10^6 \text{ m}$	Radius of Earth
$T_{\oplus} \approx 23 \text{ h } 56 \text{ min } 4 \text{ s}$	Sidereal day

kT TNT equivalent  
 $\approx 4.2 \times 10^{12}$  J

Kiloton TNT equivalent

MT TNT equivalent  
 $\approx 4.2 \times 10^{15}$  J

Megaton TNT equivalent

Hiroshima atomic bomb  
 $\approx 84 \times 10^{12}$  J

Hiroshima atomic bomb



# Acknowledgement

I would like to thank ...

Prof. Dr. Andreas Burkert for the supervision of my thesis, the great discussions and for enabling me to present my thesis to many professional and public audiences.

Kristina Monsch and Raphael Franz for a lot of support and encouraging me to meet any challenges.

Steven R. Chesley for sharing the synthetic impactor dataset.

Andreas Frühauf, Thomas Pfaller, Thomas Steingasser and all other people who somehow helped me in realizing this thesis.

all my office colleagues and all the members of the Computational Astrophysics Group of the University Observatory Munich for always having a sympathetic ear and inspiring conversations.

the numerous MIAPP participants who gave me new input and encouraged me to continue my scientific journey.



# Statement in lieu of an oath

Diese in englischer Sprache verfasste Masterarbeit orientiert sich am typischen Sprachstil astrophysikalischer Publikationen. Somit wurde insbesondere das Personalpronomen "we" verwendet, obwohl es sich nur um einen einzelnen Autor handelt.

Hiermit erkläre ich, die vorliegende Arbeit selbständig verfasst zu haben und keine anderen als die in der Arbeit angegebenen Quellen und Hilfsmittel benutzt zu haben.

---

Michael Frühauf

München, 30. Juli 2018